International Ocean Atlas and Information Series, Volume 13

NOAA Atlas NESDIS 77

CLIMATOLOGICAL ATLAS OF THE NORDIC SEAS AND NORTHERN NORTH ATLANTIC

Silver Spring, Maryland
June 2014

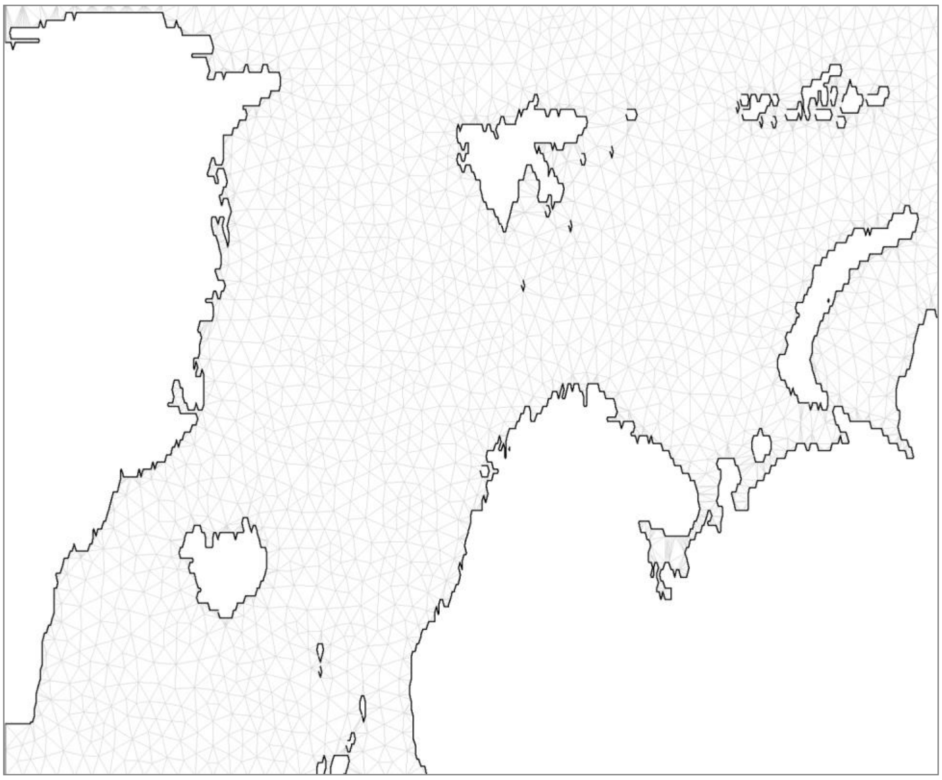

U.S. DEPARTMENT OF COMMERCE
National Oceanic and Atmospheric Administration
National Environmental Satellite, Data, and Information Service

National Oceanographic Data Center

Additional copies of this publication, as well as information about NODC data holdings and services, are available upon request directly from NODC.

National Oceanographic Data Center User Services Team
NOAA/NESDIS E/OC1
SSMC III, 4th floor
1315 East-West Highway
Silver Spring, MD 20910-3282

Telephone: (301) 713-3277
Fax: (301) 713-3302
E-mail: nodc.services@noaa.gov
NODC web: www.nodc.noaa.gov

For updates on the data, documentation, and additional information about this product please refer to: www.nodc.noaa.gov/OC5/nordic-seas

This publication should be cited as:

Korablev, A., A. Smirnov, and O. K. Baranova, 2014. *Climatological Atlas of the Nordic Seas and Northern North Atlantic*. D. Seidov, A. R. Parsons, Eds., NOAA Atlas NESDIS 77, 122 pp. , dataset doi: 10.7289/V54B2Z78

International Ocean Atlas and Information Series, Volume 13

NOAA Atlas NESDIS 77

CLIMATOLOGICAL ATLAS OF THE NORDIC SEAS AND NORTHERN NORTH ATLANTIC

Alexander Korablev[1], Alexander Smirnov[2], and Olga K. Baranova[3]
Editors: Dan Seidov[3] and Arthur R. Parsons[3]

[1] *Geophysical Institute, University of Bergen (Norway)*
[2] *Arctic and Antarctic Research Institute (Russia)*
[3] *National Oceanographic Data Center, NOAA/NESDIS (USA)*

Silver Spring, Maryland
June 2014

U.S. DEPARTMENT OF COMMERCE
Penny S. Pritzker, Secretary

National Oceanic and Atmospheric Administration
Kathryn D. Sullivan,
Acting Under Secretary of Commerce for Oceans and Atmosphere

National Environmental Satellite, Data, and Information Service
Mary E. Kicza, Assistant Administrator

CONTENTS

LIST OF TABLES

LIST OF FIGURES

ACKNOWLEDGEMENTS

The present work has been carried out within the framework of International Oceanographic Data and Information Exchange (IODE) Global Oceanographic Data Archeology and Rescue (GODAR) Project.

The authors and editors are grateful to Dr. Margarita Gregg, the Director of NOAA National Oceanographic Data Center (NODC) and current Director of the World Data Center for Oceanography (WDC) in Silver Spring, Maryland for her support of the work on this Atlas. We are also thankful to Sydney Levitus, the former Director of the WDC, and Tim Boyer, Dr. Ricardo Locarnini and Evgeni Yarosh, of NODC for their assistance with the Atlas and inclusion of the data into the World Ocean Database. Our thanks go also to Professor Tor Eldevik of the Geophysical Institute, University of Bergen, for his invaluable comments on the text of the Atlas and to Steven Rutz (NODC) for his final review of the Atlas. John Relph, John Carroll and Andy Allegra (NODC) are acknowledged for review of the online version. We express our special gratitude to C. Troupin, M. Ouberdous and J.-M. Beckers of the GeoHydrodynamics and Environment Research (GHER) Group, University of Liege for providing us with the Data-Interpolating Variational Analysis (DIVA) software[1] and for their support during Atlas development. Special thanks go to Professor G. Alekseev, the Chief of the Air-Sea Interaction Department of the Arctic and Antarctic Research Institute (AARI) and E. Medvedchenko, N. Kharlanenkova, A. Vyazilova and V. Ivanov of AARI for their thorough assistance. Alexander Korablev greatly appreciates the support provided by the University of Bergen, Geophysical Institute, for the opportunity to complete the Atlas at the Geophysical Institute.

We wish to acknowledge the NOAA's NODC (www.nodc.noaa.gov), the International Council of the Exploration of the Seas (www.ices.dk), Institute of Marine Research (www.imr.no), Alfred Wegener Institute for Polar and Marine Research (www.awi.de), Institute of Oceanology Polish Academy of Sciences (www.iopan.gda.pl) for providing access to their hydrographic data sets as well as the Arctic and Antarctic Research Institute (www.aari.ru) for access to historical cruise reports and publications in the institute's library.

---

[1] DIVA development supported by the European Union Sixth Framework Programme (FP6/2002–2006) under grant agreement # 026212, SeaDataNet, Seventh Framework Programme (FP7/2007–2013) under grant agreement # 283607, SeaDataNet II, and project EMODNet (MARE/2008/03 – Lot 3 Chemistry – SI2.531432) from the Directorate-General for Maritime Affairs and Fisheries.

ABSTRACT

The goal of the Atlas is to provide the international scientific community and wider general public with a regional dataset and illustrative material in support of climate change studies in the key regions of high northern latitudes. The dataset is built on an enhanced collection of observations spanning over a period from the end of the 19th century to 2012. It is based on *in situ* data that had been considerably improved (data addition, editing and quality control) within the framework of IODE's Global Oceanographic Data Archeology and Rescue Project (GODAR).

The geographic region of the Atlas is bounded by 60° N – 82° N, 45° W – 70° E and thus includes, entirely or partly, eight seas. Among many established geographical terms for the area north to 60° N, we selected a combination of two names – 'The northern North Atlantic' and 'The Nordic Seas'. In fact, there are two definitions of the Nordic Seas - with and without the Barents Sea with a clear tendency in literature to exclude the Barents Sea. We decided to follow Hansen & Østerhus (2000) specification combining the Norwegian, Greenland, Iceland and Barents Seas together for several reasons, which will be discussed in Introduction.

The Atlas is comprised of two types of oceanographic data presentation, namely time-depth diagrams, and horizontal fields at selected depths. The time-depth diagrams of water temperature, salinity, density and dissolved oxygen are computed from *in situ* observations and visualize regional variability in 12 selected areas in the northern North Atlantic and the Nordic Seas. Additionally to representing long-term fluctuations of oceanographic variables, the diagrams offer information for controlling temporal transformations seen in the horizontal gridded fields.

The horizontal gridded fields, included in the Atlas, were generated by a special interpolation algorithm. Using this algorithm, unevenly distributed observations were interpolated on regular grid with 0.25° × 0.25° spatial resolution at 29 depth levels. The employed interpolation technique is called 'Data Interpolating Variational Analysis (DIVA)' method and was specially designed for oceanographic data analysis. The software is freely available for non-commercial purposes. SeaDataNet climatologies (gher-diva.phys.ulg.ac.be/web-vis/clim.html) are based on DIVA and include products for the North Atlantic and the Arctic while the Nordic Seas area remains underrepresented.

An essential difference between the SeaDataNet products and the present dataset is a higher (up to monthly) temporal resolution of the climatological fields and two different approaches ('A' and 'B') to computing the mean fields for this Atlas. Variant 'A' is based on analysis of all data within a certain period regardless of the date of the observation. Variant 'B' is the result of the arithmetic averaging of the monthly gridded fields. Both variants have certain advantages and disadvantages. A biasing towards summer months in year mean fields in variant 'B' is reduced, but spatial coverage is better in variant 'A'.

All gridded fields in the Atlas are accompanied by interpolation error (variant ‘A’) or the standard error of the mean (variant ‘B’). It provides users with the possibility of selecting data with known accuracy for further processing or analysis.

The Atlas consists of six different types of climatological fields with different temporal integration of the observations (from a month of a year to decades and selected abnormal periods). The anomalous hydrographic regime periods have been chosen in accordance with regional variability of the thermohaline parameters revealed in the time-depth diagrams. In-depth analysis of the temporal–spatial pattern of variability, which was derived from the dataset used in the Atlas, was not included here. The details of this analysis will be presented in an accompanying paper ‘Nordic Seas in transformation: evidence from a new climatology and extended *in situ* dataset’ (in preparation). The technical report of the Atlas outlines the region’s physical-geographical conditions and a description of the *in situ* dataset, the interpolation technique and the software used for data processing. A brief analysis of the time-depth diagrams and gridded fields is also included.

Publication of this Atlas coincided in time with the new release of the World Ocean Database (WOD13). WOD13 provides international scientific community a considerably updated source of information, including dataset used for this Atlas preparation. Additionally, NODC has recently published a high-resolution regional climatology of the Greenland, Iceland and Norwegian Seas (GINS) with 0.1° × 0.1° spatial resolution of monthly, seasonal and annual temperature and salinity. Both WOD13 and GINS regional climatology can be accessed from NODC web site (www.nodc.noaa.gov). The new release of WOD13, the new NODC GINS climatology and this Atlas have some common features and yet are substantially different in many aspects and are complementary rather than overlapping. The authors and editors, therefore, believe that both the updated *in situ* dataset, included into the WOD13, the GINS regional climatology and the climatological fields presented in this Atlas will be used side-by-side in a wide range of applications and help to better understand the ocean variability in the Nordic Seas and their adjacent regions of the northern North Atlantic and Arctic oceans.

ATLAS CONTENT

The Atlas consists of

- inventory of the oceanographic stations from 1900 to 2012; (www.nodc.noaa.gov/OC5/nordic-seas/atlas/inventory.html)
- temperature, salinity, density and oxygen time–depth diagrams for 12 areas in the Nordic Seas and in the northern North Atlantic; (www.nodc.noaa.gov/OC5/nordic-seas/atlas/diagrams.html)
- 98,952 gridded fields of temperature, salinity and density for 60° N – 82° N, 45° W – 70° E geographic region, different periods (monthly, yearly, periods, decades) and 29 standard depths (Table 1);
- 10,478 maps of temperature, salinity and density distributions for different mean periods (periods, decades) at 29 standard depth levels (Table 1);
- 80,536 NetCDF files with gridded fields available for download (Table 1);

The gridded fields, maps and NetCDF data files are available at www.nodc.noaa.gov/OC5/nordic-seas/atlas/climatology.html.

The data ***inventory table***, posted on the web page, provides access to the series of maps showing oceanographic stations positions over the Atlas geographic region for each month from 1900 to 2012 (see Section 2 for information about observed dataset). In addition, the table offers links to the maps were the stations are combined either for all months of a year or all years of a month. The map with positions of all 503469 stations used in the present release of the Atlas can be found at the bottom-right corner of the table.

Time series of temperature, salinity, density and oxygen in the form of the ***time–depth diagrams*** (Section 5) were included into the Atlas to display regional variability at 12 selected locations where the most uniform and abundant data were collected.

We imply here that a ***gridded field*** is a two dimensional dataset which contains the estimated (interpolated) values of water temperature, salinity or density on regular 0.25° × 0.25° latitude – longitude grid. The spatial analysis (interpolation) procedure has been implemented by means of the DIVA method (Section 3) at 29 standard depth levels (Table 1, footnote). Six types of gridded fields, based on two computational approaches (A or B), for various periods are listed in the Table 1.

The ***monthly fields*** are the result of the analysis of observations within a calendar month of a year (if more than three samples were available at a standard depth). Totally, 79,828 gridded fields of temperature, salinity and density are available for the 1900–2012 period. The ***yearly fields*** represent the analysis of all the samples within a selected year regardless of the annual variations. Two ***long-term average periods*** (or ***reference periods***) were selected to represent a mean condition: based on all available observations from 1900 to 2012 and a period with more uniform stations distribution and better data quality from 1950 to 2000. Six ***anomalous periods*** were defined from the time–depth diagrams as periods with prevailing positive or negative anomalies: 1950–1970, 1960–1970, 1976–1982, 1976–1999, 1992–1998, and 2000–2012. The overlapping periods highlight the difference between an anomalous period and an abrupt event. Longer periods signify relatively uniform abnormal regimes which can include one or several stronger events with unidirectional signals. Joint consideration of gridded fields computed for the anomalous and reference periods allows estimating a magnitude and a spatial pattern of the anomalies specific for an anomalous regime. Eleven decadal periods were also computed as a common practice in oceanography: 1900–1910, 1911–1920, 1921–1930, 1931–1940, 1941–1950, 1951–1960, 1961–1970, 1971–1980, 1981–1990, 1991–2000, and 2001–2012.

A number of maps with variables horizontal distributions are available through the web interface for the anomalous periods and decades (Table 1). Maps with monthly and yearly distributions are not included due to their great number, but can be plotted using the provided NetCDF files.

The climatological gridded fields and corresponding maps based on averaging of the monthly fields (**variant B**) are provided only for anomalous periods with **yearly** averaging (field type 5 in Table 1). Other averaging can be computed using the provided monthly gridded fields in NetCDF format. An algorithm has been applied to compute the mean yearly fields by variant B, which includes two steps. First, mean monthly fields were computed (if at least three nodes with estimated values existed for a period) by averaging of the monthly gridded fields (variant A) for distinct years. Then, the derived 12 mean monthly fields were averaged to obtain a mean yearly field (if at least there are three months with estimated values at a node within a year). The yearly fields computed by the variant B are supplied by the error of the mean, which depends on the number of months within a year used to compute an annual mean value in each grid node. The applied algorithm served to reduce a bias to the summer months, like it is in case when all observation are analyzed together regardless the date of observations. The difference between yearly gridded fields produced by approaches A and B is demonstrated in Section 6.

Section 6 also contains examples how the climatological and reference fields can be treated together. One application is the estimation of anomalies' magnitude and spatial pattern for a period of interest (month, anomalous period, or decade) relative to a reference periods (1900–2012 or 1950–2000).

Most of the data processing during the Atlas preparation was made by means of ‘Ocean Shell’ author software, specially developed for large amount of oceanographic data handling (Section 4).

Table 1. Inventory of the gridded fields, maps and data files included in the Atlas

N	Type of field	Variant	Field composition	Number of fields total/with data	Total number of files in NetCDF format and a file composition	Maps
1	Monthly	A[1]	3V/113Y/12M/29L	t*: 26747/26747 s*: 26562/26562 d*: 26519/26519	79828 1Y/1M/1L	-
2	Yearly	A	3V/113Y/29L	9831/8568**	339 1V/1Y/29L	-
3	Anomalous periods Monthly	A	8P/3V/12M/29L	8352/8237	288 1P/1V/1M/29L	8165***
4	Anomalous periods Yearly	A	8P/3V/29L	696/696	24 1P/1V/29L	696
5	Period 1900-2012 Monthly	B[2]	8P/3V/12M/29L	1044/985	288 1P/1V/29L	985
6	Period 1900-2012 Yearly	B[2]	8P/3V/29L	696/696	24 1P/1V/29L	696
7	Decades Yearly	A	11P/3V/29L	957/927	33 1P/1V/29L	921
			Total:	100360/98952	80536	10478

1. Variant **A** is a basic algorithm of data interpolation when all samples for the selected period are processed together regardless date of each sample;
2. Variant **B** based on the monthly gridded fields (variant A, N1) arithmetic averaging if there are at least three nodes with estimated values within a period;

* – monthly fields were only computed if more than 3 samples existed at a depth level;
** – numbers are different because not all years have data;
*** – number of maps is less than number of fields with data due a specific plotting software problem at deep depth levels when a variable has identical values at all locations;

V – variable (temperature, salinity or density);
Y – calendar year; **M** – calendar month; **L** – standard depth level; **P** – time period (anomalous or decadal);

29 standard levels: 0, 10, 20, 30, 50, 75, 100, 125, 150, 200, 250, 300, 400, 500, 600, 700, 800, 900, 1000, 1100, 1200, 1300, 1400, 1500, 1750, 2000, 2500, 3000, 3500;

Example:
3V/113Y/29L shows that this type of field includes 3 variable for 113 years at 29 depth levels totally 9831 fields; The fields are converted into 339 NetCDF files, each file with 1V/1Y/29L composition consists of 1x1 x 29 = 29 fields for each variable, year and depth level; Correspondently, the total number of fields of this type equal to 339x 29=9831

1. INTRODUCTION

Modern oceanography relies on diverse digital information about multiple ocean elements– temperature, salinity, chemical composition, etc. Since the beginning of instrumental measurements more than a century ago, oceanographic observations have been conducted by various marine organizations and stored in different formats on different media. Numerous attempts were made to collect and merge observations together at different levels, from research institutes to the various data centers. The Climatological Atlas of Nordic Seas and Northern North Atlantic presents a new step towards compiling a complete dataset of observed data and derived climatological fields for the Nordic Seas and the northern North Atlantic.

The dataset, especially the historical measurements, were considerably improved, while the climatological gridded fields were computed by means of the state-of-the-art spatial interpolation technique. Certainly, further efforts are required for improving both the *in situ* data collection and the climatological fields by overcoming the existing technical, economic and bureaucratic problems (not all observed data are yet publicly available).

This Atlas is built upon a dataset developed at the Arctic and Antarctic Research Institute (AARI) in the late 1980s containing vast amount of Russian observations including those collected during extensive Soviet field programs in the northern North Atlantic and Nordic Seas. As a part of the Atlas effort, this AARI dataset was converted to a modern database format and updated to include international observations from multiple sources (Section 2) using modern software for quality control (Section 4).

We present a selective overview of the current knowledge about ocean properties and processes in the region to facilitate understanding and interpreting of the materials included in the Atlas. Comprehensive information can be found in books (Helland-Hansen & Nansen, 1909, Hurdle, 1986, Drange et al., 2005., Dickson et al., 2008), reviews (Trangeled 1974, Hopkins, 1991, Hansen & Østerhus, 2000, Blindheim & Østerhus, 2005) and numerous research papers. Definitely, the progress in understanding of processes and driving mechanisms is directly linked to the improvements in instruments and data accumulation.

Our main objective was to compile a gridded climatological dataset to support studies of ocean variability during the period of instrumental observations. There are at least three interfering circumstances: (1) insufficient number of observations, (2) inadequate data quality control and (3) limitations associated with interpolation techniques. The first obstacle is the most critical (Section 2.1). None of the existing geostatistical techniques can emulate a reliable gridded field without a sufficient number of properly distributed qualitative observations. Thus, a labor-intensive work was needed to improve the observed dataset (Section 2.2), which has become a part of the World Ocean Database 2013 (WOD13). Inadequate quality control introduces into the interpolation process not only outliers but also biases distorting a natural variability. There are also too many data formats, duplicates and incomplete metadata related problems, which had to be solved or at least reduced at the quality control stage. The observed data used in the Atlas passed through an extensive quality check, with the biases-suspicious instruments were eliminated from the analysis altogether (Section 2.3). Until recently, no common or universally accepted method existed for spatial interpolation of oceanographic data (either for analysis or gridding). Here we use a technique known as Data-Interpolating Variational Analysis (DIVA, Section 3) developed in Department of Astrophysics, Geophysics and Oceanography, University of Liège. The method has already been tested for several regions of the World Ocean, well documented and is being continuously improved and updated.

Geographic region and bottom topography

The gridded fields in the Atlas are presented for the geographic region within the following latitudinal and longitudinal limits 60° N – 82° N, 45° W – 70° E (Fig. 1.1). The data for spatial interpolation were from a larger area, with two degrees extension in all directions to provide more reliable estimations at boundaries. The Atlas includes data from eight seas belonging to the Nordic Seas system (some only partly), and small areas of the northern North Atlantic to the south and the Arctic Ocean (to the north).

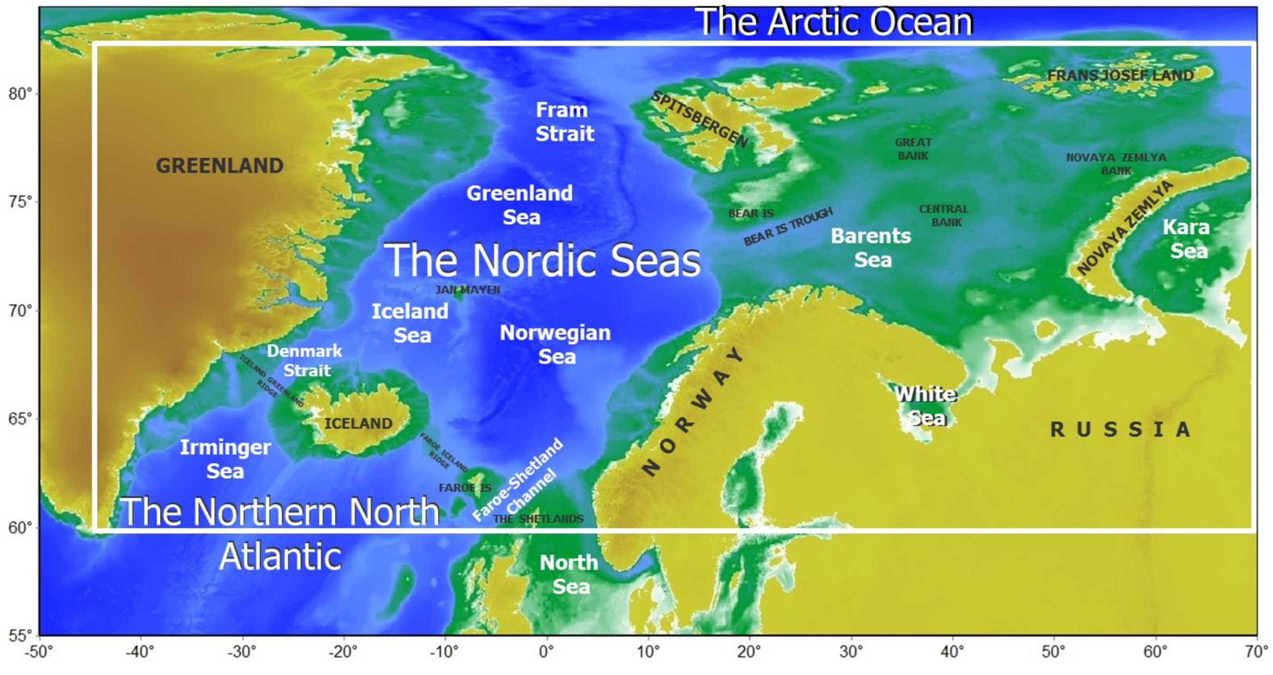

Figure 1.1 The Atlas area (delimited by the white rectangle). Background shows smoothed ocean bathymetry and land topography extracted from ETOPO1 global relief model (www.ngdc.noaa.gov/mgg/global).

The bottom topography shapes major features of regional circulation and exchanges between adjacent basins (see Hurdle, 1986, Blindheim & Østerhus, 2005 for a detailed overview). The northern North Atlantic and the Nordic Seas are separated by the underwater Greenland – Scotland Ridge with the deepest passage at 840 m (Hansen & Østerhus, 2000). Submarine ridges split the interior of the Nordic Seas into the Norwegian (3200 - 3600 m), Lofoten (3200 m), Greenland (3600 m) and Boreas (3200 m) deep basins. Water exchange between the Nordic Seas and the Arctic Ocean occurs through the 2500 m deep Fram Strait, the Barents Sea Opening and the shallow Barents Sea. Due to very limited exchanges through other passages (Bering and Canadian straits), Helland-Hansen and Nansen (1909) stated that the Norwegian Sea (their definition also includes the Greenland and Iceland Seas) is an ‘enclosed sea’. Later, when it was found that the Norwegian Sea and the Arctic Ocean have a deep connection via the Fram Strait the whole area became known as the Arctic Mediterranean (Aagaard et al., 1985).

Processes shaping the water masses and volume fluxes

Spatial distribution of oceanographic properties is formed by a complex synergy of multiple physical processes including advection from adjacent regions, internal recirculation, mixing with surrounding waters, air–sea interaction, sea-ice formation/melting etc. In general, currents in the ocean are highly turbulent and variable, so that the mean flow cannot be easily distinguished. Turbulent character of the surface currents around the world can be seen in an animation of the satellite and *in situ* data synthesized by an ocean general circulation model (available for viewing at svs.gsfc.nasa.gov/vis/a000000/a003800/a003827). Lagrangian drifters provide further insides into the nature of currents and water mixing in the ocean. Koszalka et al., 2013 analyzed trajectories of 168 drifters in the Nordic Seas and found that mean arrival time from the southern Norwegian Sea to the entrance to the Barents Sea and Fram Strait are 200 and 500 days, correspondingly. However, the transit time for the individual water particles can vary from 4 months to 2 years. At the same time, it was found that the center of the mass of a group of water parcels moves northward at speeds comparable with hydrographic measurements, confirming an advective nature of signal transfer in the Nordic Seas. Both examples emphasize the role of the horizontal circulation affecting oceanographic variable distributions seen in horizontal fields.

All water exchanges between the Nordic Seas and adjacent domains are divided into inflow, outflow and overflow regimes of transporting the mass, heat, salt and sea ice. The major component of inflow is the Atlantic water affecting the water mass properties in the Arctic Mediterranean and the regional climate (Hansen et al., 2008). Helland-Hansen and Nansen (1909) identified the three main openings over the Greenland-Scotland Ridge where the Atlantic water enters the Nordic Seas: the Denmark Strait, the Faroe-Iceland Ridge, and the Faroe–Shetland Channel (see Figure 1.1). Regular instrumental current measurements in all three branches began in the mid-1990s. Based on a 3-year period of observations Hansen et al. (2008) estimated the total volume of Atlantic water inflow as ~8.5 Sv (1 Sv = 10^6 m^3/s). It corresponds to ~90% of all water entering the Arctic

Mediterranean while the inflow through the Bering Strait and the freshwater input (runoff and precipitations) contribute together only ~1 Sv.

Most of the Atlantic water (~90 %) enters over the Faroe-Iceland Ridge and through the Faroe-Shetland Channel almost equally divided between the two branches. However, the amount of heat and salt exported by the branches differs considerably. The mean salinity of Atlantic inflow is 35.25, but increases from ≤ 35 in the Denmark Strait branch to 35.23 and 35.32 in the Faroe and Shetland branches respectively (Hansen et al., 2008).

The return flow consists of surface outflow (the East Greenland Current and flow through the Canadian Archipelago) and overflow (deep flow of dense water across the Greenland – Scotland Ridge). A general consensus (Hansen & Østerhus, 2000, Hansen et al., 2008) is that total overflow is about 6 Sv, which is equally divided between the Denmark Strait and the overflows east of Iceland. The surface outflow (3.5 Sv) was computed as a residual between the total inflow and the total overflow. Accordingly, ~ 70 % of the Atlantic inflow returns into the Atlantic Ocean as a cold and dense overflow water after modification in the Nordic Seas and the Arctic Ocean.

The generic products of the water advection and modification are the **water masses** inheriting both the properties of the source water and the history of transformation. Definitions and properties of the 14 major water masses in the Nordic Seas can be found in Blindheim & Østerhus (2005).

There is no consensus among oceanographers what seas comprise the “Nordic Seas”. Some include all seas between Greenland and Novaya Zemlya north of Greenland-Scotland Ridge and south of the Fram Strait, i.e., to include the Barents Sea and other seas east of the eastern edge of the Norwegian Sea (e.g., Hansen, Østerhus, 2000). Others define the Fram Strait-Spitsbergen-northern Norway transect as the northern and eastern edges of the Nordic Seas (e.g., Drange 2005, Blindheim & Rey 2004, Meincke et al., 1997, Rudels et al., 1999 etc.). In present Atlas, we adopt the former naming convention that includes the Barents Sea in the Nordic Seas definition. First, such composition is close to the Russian term ‘The North European Basin’, although it also includes the White Sea (Great Soviet Encyclopedia, online version, dic.academic.ru/dic.nsf/enc3p/266810). Second, without the Barents Sea, the Nordic Seas composition becomes equal to the GIN Sea (the Greenland, Iceland and Norwegian Seas) definition introduced by Hopkins (1991) that is also often in use. Third, there is a physical justification for inclusion the Barents Sea. Although being a shallow continental shelf-sea, the Barents Sea is strongly connected with the Norwegian Sea and is an important conduit to the Arctic Ocean, the reason why many studies treat the Norwegian, Iceland, Greenland and Barents Seas together (e.g. Fig. 1.2 from Helland-Hansen & Nansen, 1909).

Upper ocean circulation

Oceanographic conditions in the surface layer are closely linked to the mean surface currents. Two major water masses of different origin come into collision in the upper layer of the the Nordic Seas. The warm and salty Atlantic water, flowing northward and gradually losing their properties due to mixing and air-sea interaction, occupies the eastern part of the Nordic Seas. In the upper layer of the western part, the counter southward flow transports the cold and fresh Polar water from the Arctic Ocean.

Helland-Hansen and Nansen (1909) were the first who plotted detailed map of the surface currents in the Nordic Seas (Fig. 1.2). We have summarized knowledge about the mean upper layer circulation from selected (and far from complete) literature (Tansjura 1959, Bourke et al., 1992, Poulain et al., 1996, Loeng et al., 1997, Hansen & Østerhus 2000, Orvik & Niiler 2002, Fogelqvist et al., 2003, Jakobsen et al., 2003, Skagseth 2004, Rudels et al., 2005, Østerhus et al., 2005, Dickson et al., 2007, Jonsson 2007, Slubowska-Woldengen et al., 2008, Sutherland & Pickart, 2008, Koszalka et al., 2011, Beszczynska-Moller et al., 2012, Jónsson & Valdimarsson 2012a, 2012b, Våge et al., 2013). The result of this compilation is shown in Figure 1.3. This schematic view was adjusted by overlaying the currents over the climatological distribution of salinity at 50 m depth.

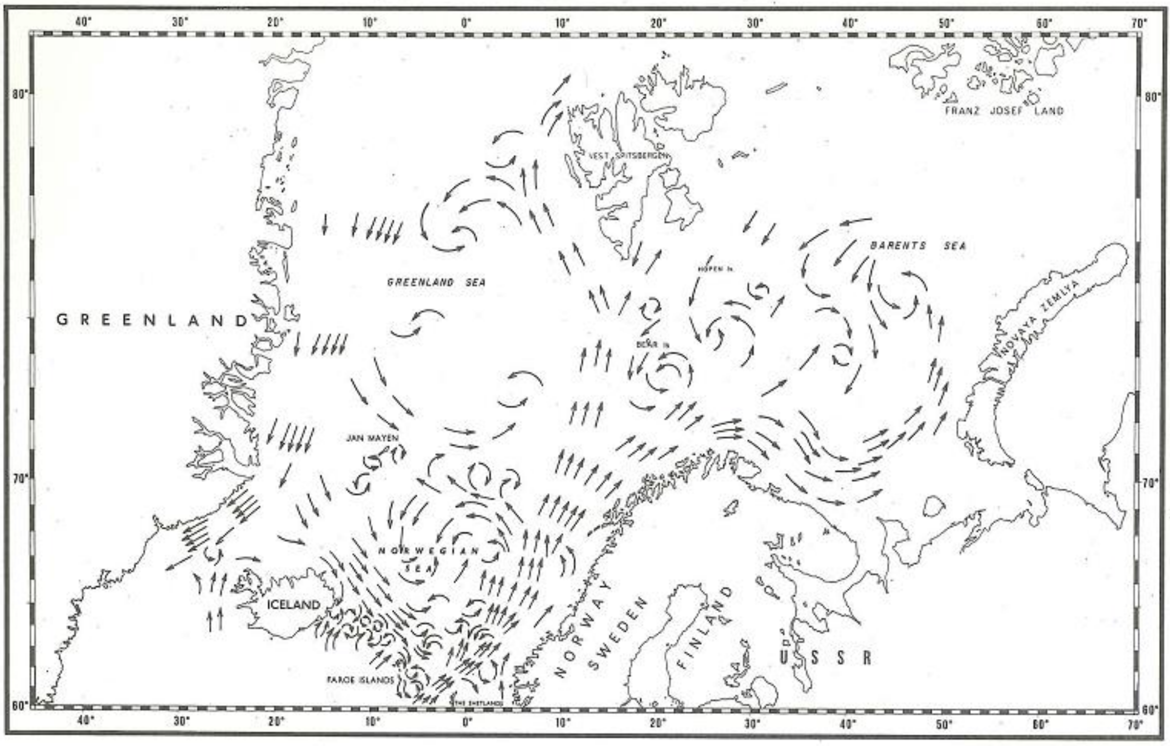

Figure 1.2 The circulation of the Norwegian Sea (Fig. 2 from Helland-Hansen & Nansen, 1909).

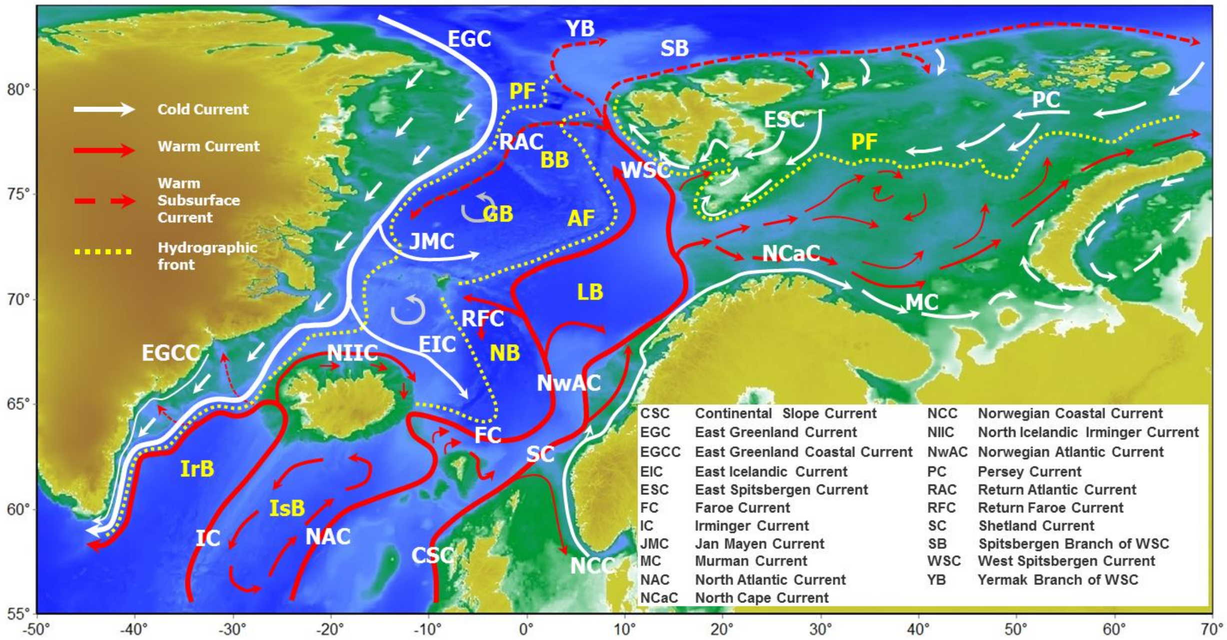

Figure 1.3 Schematic view of the mean upper ocean circulation. Abbreviations in yellow indicate the deep basins (IrB – Irminger Basin, IsB – Iceland Basin, NB – Norwegian Basin, LB – Lofoten Basin, GB – Greenland Basin, BB – Boreas Basin) and the hydrographic fronts position (AF – Arctic Front, PF – Polar Front) defined from mean 1900–2012 salinity distribution at 50 m depth. Background shows smoothed ocean bathymetry and land topography extracted from the ETOPO1 global relief model (www.ngdc.noaa.gov/mgg/global).

Interestingly, the earlier publications often show far more detailed currents schemas, based on intuition rather than instrumental measurements. For instance, Tansjura (1959) named 14 currents in the Barents Sea. Comparison of the Figures 1.2 and 1.3 shows little difference in major pattern of the surface circulation, highlighting Helland-Hansen and Nansen’s insight, regardless data scarcity. In spite of a considerable progress in recent archiving of a large volume of new data, certain currents require further monitoring to resolve their variability on seasonal and inter-annual time-scales

Swift & Aagaard (1981) introduced a convenient process-motivated division of the Nordic Seas into the Atlantic, Arctic and Polar domains. The Atlantic and Polar domains, according to the names, denote the areas where waters of the Atlantic and Polar origin dominate. The Arctic domain, in between, comprises the central parts of the Greenland and Iceland seas, separated from the Polar domain to the west by the Polar Front, and from the Atlantic domain to the east by the Arctic Front (Fig. 1.3). Uniqueness of the Arctic domain lies in the fact that a spectrum of arctic water types (intermediate, deep and bottom) could be formed there in winter at the sea surface owing the specific water column stratification and atmospheric forcing.

The Norwegian Atlantic Current

In the Norwegian Sea (Fig. 1.3), the North Atlantic Current (NAC) and Continental Slope Currents (SC) continue as the Faroe Current (FC) and Shetland Current (SC), which comprise the two-jet Norwegian Atlantic Current (NwAC). The eastern jet is a topographically controlled predominantly barotropic current flowing along the Norwegian continental slope over 500–1000 m depth, while the western offshore branch follows 2000–2500 m isobaths as a baroclinic unstable jet attached to the Arctic Front (Orvik & Niiler, 2002). Analyzing the surface drifters, Koszalka et al. (2011) estimated the current's velocities in the eastern and western branches as 30–35 and 20–25 cm/s respectively. It was found that the two branches reconcile over the Vørning Plateau, with a quasi-permanent vortex dominating the center of the Lofoten Basin (e.g., Ivanov & Korablev, 1995 a, b, Köhl, 2007, Volkov et al., 2013, Søiland & Rossby, 2013, Raj et al., 2013). Further to the north, a part of the Atlantic water carried by the NwAC deviates into the Barents Sea through shallow Barents Sea Opening, crossing the continental slope close to 72° 30' (Skagseth et al., 2008). The main flow of NwAC continues to the Arctic Ocean as the West Spitsbergen Current (WSC).

The western branch of the NwAC flows around the western periphery of the Lofoten basin and then along the Arctic Front joining the WSC in the Fram Strait (Walczowski, 2013). The branch recirculates partly near Jan Mayen with the fractions turning to the Iceland Sea and southward along the western periphery of the Norwegian Basin (Blindheim & Østerhus, 2005).

At the northern part of the Fram Strait, the WSC splits on three branches. The major portion recirculates southward as the Return Atlantic Current (RAC) and forms a subsurface jet flowing along the Greenland continental slope. The rest of the Atlantic water enters the Arctic Ocean as the Spitsbergen Branch (SB) following the Barents Sea slope and the Yermak Branch (YB) streaming around the Yarmak Plateau. All branches have strong seasonal and multi-year fluctuations, which are not yet sufficiently studied.

Atlantic-derived water occupies the near-bottom layers over the continental shelves and penetrates into numerous fjords, as well. The fjords play an important role in conditioning of the upper layer on the shelf because of the freshwater runoff. The shelf-fjord water exchanges have strong seasonal and interannual fluctuations controlled by upwelling and downwelling.

A deep baroclinic pressure gradient between the Nordic Seas and the northern North Atlantic is arguably a dominant force driving the Atlantic water transport across the Greenland-Scotland Ridge (Hansen et al., 2008). The stability of the overflows is supported by the Atlantic water transformation, which occurs mainly in the Nordic Seas (Isachsen et al., 2007, Eldevik & Nilsen, 2013).

The Norwegian Coastal Current

Oceanographic conditions and dynamics of the Norwegian Coastal Current (NCC) are summarized in the book ‘The Norwegian coastal current: oceanography and climate’ (Saetre Ed., 2007). We refer the interested reader to the detailed current maps given there (Figs. 2.11, 2.12, 5.9, 8.1 in the cited publication). The main sources of the current are the freshwater outflow from the Baltic (~50 %), the freshwater run-off from Norway (~40 %) and the North Sea (~10 %). Along northbound flow, salinity in the NCC gradually increases due to mixing with the saltier Atlantic water. Typical current speed is 20–50 cm/s and the water transport values are of 1–2 Sv. Strong temporal variations in the current pattern can be due to changes in the main driving forces–wind and atmospheric pressure, tides, freshwater runoff. The character and scope of this variability differ considerably along the southern, central (62° N – 68° N) and northern Norwegian shelf. In the Barents Sea, the NCC continues along the Norwegian coast, narrowing off the North Cape and deflecting offshore farther to the east (changing its name to the Murman Current after crossing Russian border). During summer, water temperature in NCC is close to the Atlantic water, but salinity falls below 34.7. Strong seasonal variability is reported (Skagseth et al., 2008), with a deep and narrow current in winter and a wide and shallow one in summer.

The Norwegian Coastal Oceanographic Observing System, established in the mid-1930s, has been providing valuable information for identifying climatic signal in the Norwegian coastal waters. Fore example, it recorded, among other prominent climatic events, that sharp water warming after 1987 and at the beginning of the 1990s occurred along the southern and central parts of the Norwegian coast. This coastal warming was attributed to significant increase in the inflow of the Atlantic water to the North Sea (Saetre Ed., 2007). Relatively cold and low-salinity period at the end of the 1970s and early 1980s appears to be associated with the ‘Great Salinity Anomaly’ described by Dickson et al. (1988). As the main mechanism driving the long-term variability in the upper Norwegian coastal waters, the authors of ‘The Norwegian coastal current: oceanography and climate’ monograph suggested an interplay of the variations in advected properties (Atlantic inflow) and the local thermohydrodynamical processes (seasonal cycle, runoff, wind forcing). In the deeper part of the Norwegian Sea the variations are mainly caused by fluctuations of the Atlantic water volume and properties.

The East Greenland Current

The East Greenland Current (EGC) is a multilayer current. At the surface, it carries the Polar water and sea-ice out of the Arctic Ocean, while at intermediate and deeper depths the current transports the modified waters of Atlantic, Nordic Seas and Arctic origin. The EGC and the water circulating in the Iceland Sea are the major sources for Denmark Strait Overflow Water, which contributes directly to the formation of the North Atlantic Deep Water (Jeansson et al., 2008, Våge et al., 2013).

Freshwater, exported by the EGC in solid and liquid forms, is the crucial factor for the high latitude climate. Extra amount of freshwater, added into the upper ocean, reinforces the stratification and thus reduces the deep water formation affecting the Atlantic Meridional Overturning Circulation (Dickson, 1988, Curry et al., 2003, Curry & Mauritzen, 2005). It implies the importance of long-term freshwater transport monitoring in the EGC.

Time-series of sea-ice extent measured from satellites begun since 1979, while the direct measurements of liquid freshwater transport within the EGC began much later. In 1997, at 79° N and in 2000 at 74° N and 63° N, Holfort et al. (2008) estimated the total flux of freshwater through the Fram Strait to be ~2000 km^3/year and equally divided between EGC and shallow shelf currents. Further south, at 74° N, the total flux decreased to 1400 km^3/year, including 800 km^3/year carried by the EGC. A rough estimates at 63° N, within only three years of observations, showed a wide spread of freshwater transport between mere 150 and 2200 km^3/year. The monitoring network was too sparse to measure freshwater divergence between the different circles of latitude, which was supposedly small.

There are two topographically steered branches of the EGC, which transport upper and deeper water towards the interior parts of the Nordic Seas. The Jan Mayen Current (JMC) flows along the southern periphery of the Greenland Basin, while the East Icelandic Current (EIC) diverts towards the Faroe–Shetland Channel in the Iceland Sea.

The EGC is not the only current that carries liquid freshwater to the North Atlantic. South of the Denmark Strait, the East Greenland Coastal Current (EGCC) was identified as a shallow and fast baroclinic jet generated by the summer runoff (Bacon et al., 2002). It was, however, suggested that the latter is rather a recirculation branch of the EGC (Sutherland & Pickart, 2008). Bacon et al. (2008) further considered the importance of local sea-ice melting and wind for the EGCC generation.

Another climatically important process is the interaction between Atlantic water and submarine parts of the Greenland Ice Sheet. As it has been recently understood, the Atlantic water has a direct contact with the tidewater glaciers' submarine ice fronts in deep Greenland's fjords and its increased temperature contributes to the glaciers' melt and speed acceleration (Straneo et al., 2010).

The Barents Sea

Oceanographic conditions in the shallow Barents Sea (average depth ~230 m) result from interactions between the Atlantic, Polar and Coastal water inflows. The Atlantic water enters the Barents Sea through its western and northern boundaries. The main inflow from the Norwegian Sea splits into two branches in the western Barents Sea. The southern branch, known as the North Cape Current (NCaC), continues eastward and further northward to the Arctic Ocean along the coast Novaya Zemlya (Fig. 1.3). The properties, velocities, transport and width of the currents vary and are strongly linked to the local wind forcing over the inflow region (Ingvaldsen, 2005). The northern branch of the NCaC controls the central Barents Sea, where it spreads, brakes into smaller branches and recirculates over the shallow banks (Blinheim & Østerhus, 2005). Subsurface portion of the Atlantic water enters the Barents Sea under the Polar water between Svalbard and Franz Josef Land detaching from the Spitsbergen Branch of the West Spitsbergen Current. Without direct contact with the atmosphere, the submarine portion of the Atlantic water remains relatively warm and salty (Lind & Ingvaldsen, 2012). In contrast, the near-surface Atlantic water flowing across the southern and eastern parts of the Barents Sea gradually loses its identity due to intensive cooling and mixing. For example, the measurements made in the St. Anna Through in 1996 indicated that the Barents Sea branch of the Atlantic Water reached the Arctic slope with the temperature below zero and salinity between 34.7 and 34.9 (Schauer et al., 2002b).

The water of Arctic origin arrives across the northern boundary and occupies the upper 20–200 m of the northern Barents Sea. The East Spitsbergen Current (ESC) carries the Polar Water along the eastern coasts of Svalbard, while the Persey Current (PC) enters the Barents Sea to the east of Frans Josef Land.

Loeng et al. (1997) estimated the Barents Sea's inflow budget of ~4.1 Sv as a sum of the Atlantic (3.3 Sv) and Polar (0.8 Sv) water inflows. The outflow composition was defined as the modified Atlantic water carrying to the Arctic Ocean (1.9 Sv), the modified Atlantic water and the deep water recirculated back to the Norwegian Sea (1.2 Sv) and smaller volumes of water escaping the Barents Sea through the boundaries with the Norwegian Sea (0.2 Sv), the Arctic Ocean (0.1 Sv) and the Kara Sea (0.7 Sv). The dense water carried by topographically controlled westward flow mixes with both the intermediate and the deep waters of the Norwegian Sea (Blindheim & Østerhus, 2005).

Four-year record by mooring current meters deployed along the cross-section of the Atlantic water inflow into the Barents Sea showed frequent and large fluctuations in the velocity field due to sea level changes caused by local wind forcing (Ingvaldsen et al., 2004a). The mean annual transport of the Atlantic water was estimated to be 1.5 Sv, changing from 1.3 Sv in summer to 1.7 Sv in winter (Ingvaldsen et al., 2004b). One-year instrumental current measurements between Novaya Zemlya and Frans Josef Land, in combination with numerical models (Gammelsrød et al., 2009), yielded approximately 2 Sv net volume flux towards the Arctic Ocean, half of which was dense Cold Bottom Water.

Many studies indicate that the processes in the Barents Sea (inflow, outflow, modification due to the air-sea interaction, the dense water formation etc.) have strong seasonal and interannual fluctuations. However, Årthun et al. (2012) reported an 'Atlantification' of the Barents Sea from 1998 to 2008, accompanied by 50% reduction in the annual sea-ice area being a result of strengthening and warming of the Atlantic inflow, thus implying that there was a substantial non-local trend in the Barents Sea conditions.

Intermediate, deep and bottom waters in the Nordic Seas

The intermediate and deep circulation in the Nordic Seas is radically different from the circulation in the upper ocean and is directly linked to the dense water formation and spreading processes (Mauritzen, 1996). Locally or remotely formed water masses (depending on their depth and density) either fill the internal areas of the Nordic Seas (Blindheim, 1990, Eldevik et al., 2005), cascading into the northern North Atlantic (Hansen & Østerhus, 2007, Jochumsen et al., 2012), or propagate to the Arctic Ocean through the deep Fram Strait (Aagaard et al., 1985).

Understanding deep water formation depended heavily on the progress in the deep-sea observations. Mohn (1887) was already aware that the deep basins in the Nordic Seas were filled with the 'ice-cold' water derived from the surface. Depth soundings and oceanographic observations taken during the Norwegian North-Atlantic Expedition in 1876–1878 showed, for the first time, a clear difference in deep water temperatures between the Greenland and Lofoten Basins (Fig. 1.4). Knudsen (1899) was the first to discover the dense water overflow to the North Atlantic by analyzing the Danish observations around Iceland and in the East Greenland Current taken in 1895–1896. Unfortunately, his important discovery did not receive much attention until the second half of the 20th century.

The classical mechanism of deep and bottom water formation in the Barents and Norwegian Seas was explained by Nansen (1906) and Helland-Hansen & Nansen (1909). Nansen (1906) analyzed all available data from the Barents Sea and concluded that the properties of the locally-formed bottom water varied considerably from place to place. Depending on salinity of the bottom water, he considered four different regions: southern banks and shelf (low salinity), shallow banks in the northern Barents Sea (moderately high salinity), shelf along the coast of Novaya Zemlya (high salinity), and the Bear Island Trough (salinity ≥ 34.9). The bottom water formation process was described as a gradual winter cooling and mixing of the water column, which eventually could have reached the bottom. The ice formation on the surface plays an important role, contributing to salinity increase due to brine release. Based on observed profiles in the Barents Sea, Nansen (1906) suggested that mean salinity increase from 34.7 to 35.03 of the upper 200-m water column can be caused by forming of two meters of new ice. He also described the necessary conditions for production of the bottom water with a very high salinity: stationarity (absence of strong horizontal currents during the mixing process) and ice disintegration (polynias reopening). Two possible pathways of the bottom water spreading from the Barents Sea were checked against the observations. Nansen found no communication with the Norwegian Sea, but suggested that sinking along the slope into the Arctic Ocean was possible.

Without attention to these processes in the water column, extremely high salinity observations (higher than the salinity of the inflowing Atlantic Water) may be wrongly flagged as outliers during quality control of the data from the Barents Sea. For instance, salinity as high as 35.8 was measured in April 2002 in Storfjorden (a fjord in southern Svalbard) at the depth ~150 m resulting from the brine release during ice formation (Anderson, 2004).

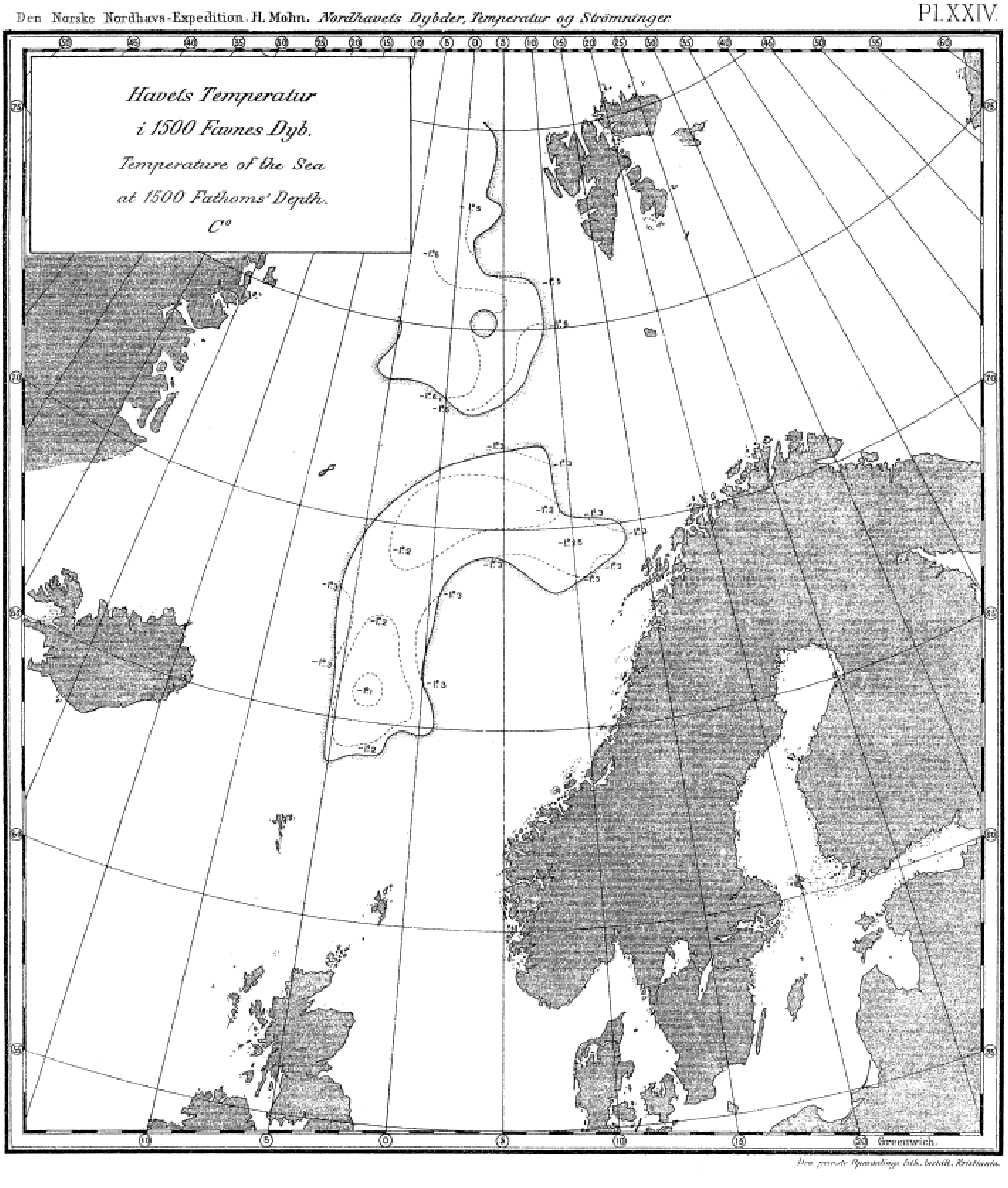

Figure 1.4 Water temperature at 1500 fathoms (2743 m). Source – plate XXIV from Mohn (1887).

New data confirmed and detailed the formation of dense bottom water in the Barents Sea at several locations: Novaya Zemlya shelf (Midttun, 1985), shallow banks (Årthun et al., 2011), marginal ice zone (Ivanov & Schapiro, 2005), and coastal polynia in Storfjorden (Skogseth et al., 2005). For instance, Årthun et al. (2011) estimated that the dense water formation over the shallow banks (9% of the Barents Sea area) contributes approximately one third of the total production. The authors distinguished two predominant mechanisms during ‘cold’ (reduced inflow of the Atlantic water, increased formation of the sea-ice) and ‘warm’ (reverse conditions) periods of the Barents Sea. During the cold periods, more dense water is produced over the banks by brine rejection, while the warm periods are characterized by the enhanced transformation of the northward flowing Atlantic Water by general cooling. Årthun et al. (2011) defined the 1950s and late 2000s periods as extremely warm, which were accompanied by a strong reduction in the total export of the dense water to the Arctic Ocean.

Nansen (1906) used the ‘Amundsen’s eleven high-quality stations’ in the Greenland Sea in 1901 (together with some previous observations (Fig. 1.5) he considered trustworthy) to infer a theory of deep-water formation in the Greenland Sea. He assumed that the renewal of the Bottom water, which filled at least two third of the whole basin, takes place at the sea-surface in a small area bounded by 73° N – 76° N and 4° W – 4° E. In addition to a strong winter cooling, he formulated several favorable conditions for developing of a deep vertical circulation (convection in modern terminology): the absence of a strong horizontal current in the center of the cyclonic circulation, the presence of cold water with relatively high salinity at the surface and the existence of warm and salty Atlantic water in the intermediate layer. Such conditions are different from what normally would occur in the central part of the Greenland Sea, where the upper layer is occupied either by low-salinity Polar water or warm Atlantic water preventing effective developing of deep convection.

The deep-water formation mechanism itself was described as a sequence of mixing (overturning) events of dense water formed at surface during the winter cooling and entrainment of the more saline subsurface water. The process continues until the vertical circulation reaches the Bottom water. According to Nansen’s theory, the vertical homogeneity of temperature, salinity and density at the deep convection site is a necessary condition for a renewal event.

The temperature and salinity distributions in Fig. 1.5 (from Helland-Hansen & Nansen, 1909), depicts the bottom water formation areas in the Greenland and Iceland Seas and can probably be regarded as the first example of the climatological fields, although based on manual analysis of a very limited dataset. Such synthesis was complicated by poor quality of a large portion of those early observations, many of which were suspicious or simply wrong.

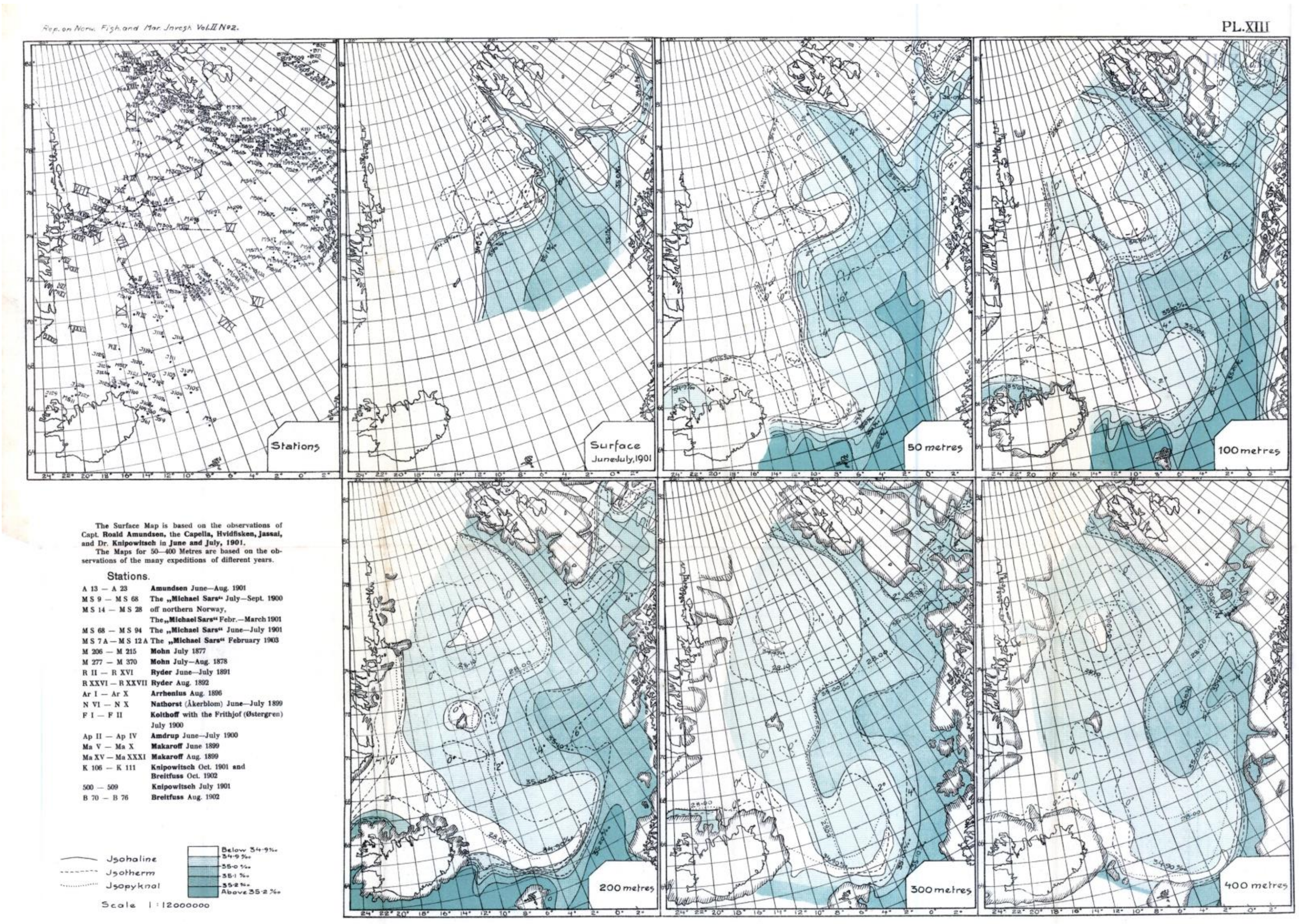

The Surface Map is based on the observations of Capt. **Roald Amundsen**, the **Capella, Hvidfisken, Jassai,** and Dr. **Knipowitsch** in **June and July, 1901.**

The Maps for 50—400 Metres are based on the observations of the many expeditions of different years.

Stations.

A 13 — A 23	**Amundsen** June—Aug. 1901
M S 9 — M S 68 M S 14 — M S 28	The **„Michael Sars“** July—Sept. 1900 off northern Norway, The **„Michael Sars“** Febr.—March 1901
M S 68 — M S 94	The **„Michael Sars“** June—July 1901
M S 7 A — M S 12 A	The **„Michael Sars“** February 1903
M 206 — M 215	**Mohn** July 1877
M 277 — M 370	**Mohn** July—Aug. 1878
R II — R XVI	**Ryder** June—July 1891
R XXVI — R XXVII	**Ryder** Aug. 1892
Ar I — Ar X	**Arrhenius** Aug. 1896
N VI — N X	**Nathorst** (Åkerblom) June—July 1899
F I — F II	**Kolthoff** with the Frithjof (Østergren) July 1900
Ap II — Ap IV	**Amdrup** June—July 1900
Ma V — Ma X	**Makaroff** June 1899
Ma XV — Ma XXXI	**Makaroff** Aug. 1899
K 106 — K 111	**Knipowitsch** Oct. 1901 and **Breitfuss** Oct. 1902
500 — 509	**Knipowitsch** July 1901
B 70 — B 76	**Breitfuss** Aug. 1902

Figure 1.5 Stations location for the 1878–1903 period (left panel) used to plot temperature and salinity distribution on the surface, and 50, 100, 200, 300, 400 m depths (to the right). Source – plate XIII from Helland-Hansen and Nansen, 1909.

Nansen (1906) also made several assumptions about the circulation of the newly formed bottom water. He envisioned that it moved away from the formation site along the bottom and spread out laterally, slightly warmed by geothermal heat sources and convective mixing with overlying waters and did not extend across the Greenland-Scotland Ridge. In his view, renewal of the Bottom water was an extremely slow process, and the amount produced during the winter was sufficient to feed this circulation. It was not clear at the time if there was a deep passage between the Nordic Seas and the Arctic Ocean between Greenland and Spitsbergen (later named Fram Strait after Nansen's ship 'Fram'). Thus, Nansen proposed two regions capable of supplying deep water to the Arctic Ocean – one north of Spitsbergen and another near the northern Novaya Zemlya.

Both Mohn's and Amundsen's observations were taken several months after the cooling season ended. However, the series of surface observations of cold and salty water in the central Greenland Sea taken during the early springs from 1901 to 1903 allowed Helland-Hansen and Nansen (1909) to emphasize that 'the formation of cold, heavy bottom water was directly observed on the very sea-surface' and that 'the process of its formation is thus settled beyond all doubts.' This entire concept had not been challenged until the second half of the 20th century.

Despite the elegancy of the theory, the fact that surface-to-bottom homogeneity was never observed demanded development of alternative hypotheses. In one hypothesis, Metcalf (1955) suggested sinking of dense water along inclined isopycnal surfaces. Another explanation was offered by Carmack & Aagaard (1973) who proposed sub-surface modification of sinking water by double diffusion of the Atlantic water within the Greenland Basin. As more deep, high-quality observations had become available, a new consensus was reached in mid 80s about deep water in the Arctic Mediterranean circulating internally, while the waters that ventilate the North Atlantic being the intermediate water masses formed in the Greenland and Iceland Seas (Aagaard et al., 1985).

Although the large-scale overturning in the Greenland Sea had never been directly observed (Ronski & Budeus, 2005), eddies (convective chimneys or submesoscale coherent vortices) with a diameter of ~10 km, which are able to create homogeneous vertical structure up to nearly 2500 m, had often been found (Wadhams et al., 2002, Gascard et al., 2002, Wadhams et al., 2004, Budeus et al., 2004, Kasajima et al., 2006). However, deep water temperature was proved to be an indicator of high or low deep water formation rates (Bonisch et al., 1997).

Dickson et al. (1996) emphasized the different role of convection in the Greenland Sea and Arctic Ocean. Slope convection in the Arctic creates a downward flux of heat (warm water entrainment during sinking) and salt (brine rejection during the ice formation) while the open ocean convection in the Greenland Sea results in upward heat and salt fluxes (warmer and saltier intermediate water ascended to the surface during the mixing). As a result, the Arctic Ocean Deep Water is about 0.3 °C warmer and 0.04–0.05 saltier than the Greenland Sea Deep Water. Certainly, such a small salinity difference can be only detected by a high quality instruments and methods. Dickson et al. (1996) postulated that ‘all other deep waters are a mixture of the two’.

In the same paper, Dickson et al. (1996) further argued that the deep waters in the Greenland Basin are being renewed not only by vertical convection, but also by horizontal advection of the deep water through the Fram Strait. Thus, the intensity of convection (volume of sinking water and depth of penetration) is a key for developing and maintaining deep water characteristics, directly or indirectly. During the active convection periods, the deepwater is not only renewed from the surface, but is also being replaced by the Arctic Ocean Deep Water if convection recedes.

Contrary to the opinion that the bottom water properties remain relatively constant in the changing climate, the horizontal mixing implies a higher variability of that water in the Greenland Basin. Blindheim & Østerhus (2005) analyzed observations in Greenland Basin for the decade of 1991–2000. They found that convection, as it was inferred from the position of 34.89 isohaline, did not penetrate deeper than 1300 m. A gradual increase of temperature and salinity of the deep layers, especially strong at 1500 m, was attributed to the increase of the volume of the Arctic Ocean Deep Water in the Greenland Basin. It was also confirmed by changes in oxygen and silicate concentrations.

Mauritzen (1996) analyzed a high quality set of hydrography and tracer data and questioned the concept that the rate of the dense water production in the Greenland and Iceland Seas (traditional sites for the dense water formation) can explain the significantly larger volume of overflows across the Greenland Scotland Ridge. Another inconsistency was that no seasonal or interannual signals were found in the overflow waters, as might had been expected from the seasonal character of the winter convection and highly variable conditions at the surface. An alternative circulation scheme was presented, with modification of the Atlantic water, occurring along three different trajectories in the Nordic Sea and in the Arctic Ocean, becoming the main mechanism of creating dense water feeding the overflows. After recirculating, all three branches meet in the Fram Strait and continue southward along the Greenland slope within the East Greenland Current. Because of en route modification, water properties in these branches change and the water occupies different depths. It was argued that the densest water branch deviates and flows without mixing around the Greenland Basin towards the Faroe–Shetland Channel and exits the Nordic Seas. The other two branches feed the overflows in the Denmark Strait. Since the properties of all three distinct water types still do not match the properties of the North Atlantic Deep Water, an additional mixing is required. Ambient water entrainment and mixing is especially strong when the overflow water descent along the southern side of the Greenland-Scotland Ridge (description of an extensive survey can be found in Mauritzen et al., 2005), thus being a candidate for the required additional mixing.

The idea that the modified Atlantic water is the main component of the overflow was further developed by Isachsen et al. (2007). Using a linear inverse modeling, they quantified the density flux across the surface and found that most of the light-to-dense water transformation takes place in the eastern part of the Nordic Seas (with a particularly high production in the Norwegian and Lofoten Basins) by a large-scale diapycnal overturning process. In the Arctic domain, where the densest waters are formed, some less intensive transformations may occur. However, the tracer release experiment conducted in 1996 (Olsson et al., 2005) confirmed that the central Greenland Sea and Faroe Bank Channel (FBC) continued to be dynamically linked in spite of the overall convection reduction after 1972 (Malmberg & Jonsson, 1997). The fact that the intermediate waters from the Greenland Sea reached the FBC of around 2.5 years was confirmed by model simulations (Eldevik et al., 2005).

Long-term variability and climatological fields

The gridded fields of oceanographic variables presented in the Atlas, were designed to address the key ocean climate change question: How much these variables have changed in the Nordic Seas during the time period supported by reliable observations? For this purpose, climatological fields based on monthly, yearly and longer averaging periods were computed. Special attention was directed at the periods with the ocean anomalous states, which have been diagnosed from time series of temperature, salinity and oxygen (Section 5).

To conclude the introduction, we briefly mention the processes that are known to have significant impacts on long-term trends and large-scale fluctuations in oceanographic variables in the Nordic Seas.

Anomalous periods in the ocean climate timeline are being often explained by the anomalies propagation (Dickson, 1988, Belkin et al., 1998, Belkin 2004, Furevik, 2001) or long-term variations linked to oceanic or atmospheric climatic indexes (Jakobsen et al., 2003, Blindheim & Østerhus, 2005, Eldevik et al., 2009). Significant correlations of hydrographic variables were found with Atlantic Multidecadal Oscillation (AMO; Skagseth et al., 2008) and North Atlantic (NAO) or Arctic Oscillation (AO) indexes (Blindheim et al., 2000). The sub-polar gyre intensity (Hatun et al., 2005) has been suggested to modulate properties of the Atlantic water entering the Nordic Seas in the late 1990s. It is obvious, however, that the distinct driving forces cannot explain the total variability in the complex climate system. AMO is the most obvious climatic index that can be traced along the Atlantic water inflow in the Norwegian Seas and further in the Barents Sea. For example, Levitus et al (2009) showed high correlation between temperature at about 100 m and AMO in the Barents Sea in the second half of the 20th and beginning of the 21st centuries. Furthermore, the importance of a distinct forcing or feedback could be time-dependent (correlation with the NAO index, for instance) – another reason for additional scrutinizing of historical datasets.

According to Levitus et al. (2012), there are six areas, where complete *in situ* oceanographic datasets are especially valuable: (1) computing of the climatological fields, which are used as initial and boundary conditions in the ocean climate models and for validation of simulations, (2) identification of ocean variability, (3) data assimilation, (4) public access to data for understanding of observed changes, (5) optimization of measurement strategies, and (6) understanding and management of the marine resources. The new release of the World Ocean Database (WOD13, www.nodc.noaa.gov/OC5/WOD13) gives to the international scientific community considerably updated source of information for their research. Additionally, NODC has recently published a high-resolution regional climatology of the Greenland, Iceland and Norwegian Seas (GINS, www.nodc.noaa.gov/OC5/regional_climate/gin-seas-climate) with 0.1° × 0.1° spatial resolution of monthly, seasonal and annual temperature and salinity on 87 standard levels with vertical resolution substantially higher than in the World Ocean Atlas 2009 (WOA09), but levels extend from the surface to 4000 meters. The new release of WOD13, the new NODC GINS climatology and this Atlas have common features and yet are different in many aspects and are complementary rather than overlapping. The authors and editors, therefore, believe that both the updated *in situ* dataset (Section 2), included into WOD13 and the GINS regional climatology, and the climatological fields presented in the Atlas (Section 6), will be used side-by-side in a wide range of applications and help to understand the ocean variability in the Nordic Seas and adjacent regions of the northern North Atlantic and Arctic oceans.

2. INITIAL DATA AND DATABASE

2.1 Database structure and content

The observational dataset (e.g., Fig. 2.3 used for the Atlas preparation, was subjected to several modifications. The earlier versions of the database were created at the Arctic and Antarctic Institute (AARI, St. Petersburg, Russia) as a compilation of all available sources for the area bounded by 60° N – 82° N and 40° W – 70° E (Ivanov et. al., 1996, Korablev et al., 2007, Smirnov & Korablev, 2010). Although the main focus was the Norwegian, Iceland, Greenland and Barents Sea, the rectangle area was chosen to fit the $5^o \times 5^o$ data structure in the World Ocean Database 2001 (Stephens et al., 2002).

The dataset was compiled in two stages. At the first stage, data from multiple data sources were merged to form a single database. The idea was to compile a dataset as complete as possible. However, the merged database had serious problems with retaining a large number of duplicates, insufficient metadata, low-quality measurements and numerous data errors. Therefore, the initial database was subjected to a comprehensive duplicate control and a rigorous quality control procedure, including the algorithms based on standard deviation check (Section 2.3). Later on, the merged database was updated by adding new data which had passed quality control before merging.

This Section describes mainly the first stage of the data processing with the applied procedures listed in Table 3 (see Appendix). Initially, almost 2.5 million stations were collected for the chosen geographical area of the Nordic Seas and northern North Atlantic from all available sources. Special software was developed for data processing (see Section 4 for details) aligned with the designed database structure (metadata, service and variables database tables) and metadata composition (25 fields in two database tables, Appendix, Tables 4, 5).

The first metadata table includes four mandatory entries: latitude, longitude, date and station version. Taken together, these entries comprise a unique, fundamental element of the database – the oceanographic station (Appendix, Table 4). Remaining positions in the metadata table are reserved for the station time (not always known), quality flag, source name, vessel name, country name, the bottom depth and the depth of the last measured level. The last three fields are the bottom depths from General Bathymetric Chart of the Oceans (GEBCO, BODC, 2003): depth at the station's location, minimum depth and maximum depth within a 5-km radius around the station. The second metadata table (Appendix, Table 5) consists of supplementary information including a station's international country/vessel code, cruise number, station number in the cruise, instrument type, name of the secondary source, etc. The oceanographic variables are stored in uniform database tables (Appendix, Table 6) with four fields: unique key, depth, a variable value, and the quality flag (Appendix, Table 8).

The data from each initial source were downloaded into the separate initial source databases with a full set of available variables by means of a convertor (a program application designed for data conversion from source to the internal database format; Appendix, Table 3). Before merging, all initial databases have passed preliminary quality control (Section 2.3). After merging, the duplicates were removed employing four automatic algorithms and an expert visual control (see next paragraph for details). An application was developed to simplify the duplicates expert visual control with possibility of merging metadata and profiles from the duplicate stations. At this stage, the stations conducted using low-accuracy instruments (MBT, XBT) and profiles with less than three depth levels (temperature or salinity profile should have at least three depth levels with observed values) were deleted from the integrated database. After applying all these procedures, the total number of stations in the integrated database was reduced from nearly 2.5 million to about one million of reliable and high-quality profiles.

The duplicates problem is common for large oceanographic datasets and is difficult to resolve. We introduced a specific hierarchy of duplicate definitions and several detecting algorithms were applied to address this issue (Appendix, Table 3). There is, however, one benefit of having duplicates – using the metadata and profiles from the duplicates during the merging process helps to compile an improved station composition.

The simplest type of duplicates is an ‘EXACT’ duplicate, when all metadata and station data are identical. Such duplicates are easy to detect. The ‘FULL’ duplicate means that some metadata fields that are not mandatory may differ. In such a case, the algorithm adds the missed metadata into the station with a higher rate of assigned priority (the source databases were rated based on their reliability). The ‘TSO2’ duplicate is found if temperature (T), salinity (S) and oxygen (O2) profiles at different stations match exactly, while the metadata and other profiles may be different. Then, the missing metadata and profiles are automatically added to the station with a higher priority. The ‘INTERPOLATED TYPE’ is a station, which is a suspected duplicate, but actually contains different interpolated versions of the same profile. For this type of duplicates, an algorithm was developed which performs a linear cross-interpolation between profiles (values from one profile interpolated to the depth levels of another). A profile is then considered to be a duplicate if the resulting profiles coincide within an arbitrary chosen threshold value (selected to be close to the historical data accuracy). The same procedure was applied to CTD profiles with different vertical resolutions. After the automatic and expert visual controls, only 25 %, or slightly more than 503,000 stations, were left in the integrated database for the 1900–2012 period.

The temporal distribution of the station numbers in the duplicate-controlled database (Fig.2.1) shows substantial fluctuations in observational activity in the northern North Atlantic and the Nordic Seas. In the 1930s, after the 2nd International Polar Year (1932–1933), the number of stations started to increase, but dropped down during the World War II (Levitus et al., 2013). After the WW II the number of observations increased rapidly. Since the mid-1950s the number of observations grew almost exponentially and exceeded 6,000 for the 1960–1990 period, with two major peaks occurred in 1957–1962 and 1982–1990. The first peak coincides with the 3rd International Polar Years (1957–1959). The second, and the most prominent, happened for the years 1982 to 1990, when the Russian field program in the Nordic Seas was all times high. The absolute maximum on the record was reached in 1984, when more than 15,000 oceanographic stations were sampled. The monthly distributions (Fig. 2.1 insert, Fig 2.2) highlight the fact that June and August are the most sampled months within a year, with more than 60,000 and 65,000 of stations respectively.

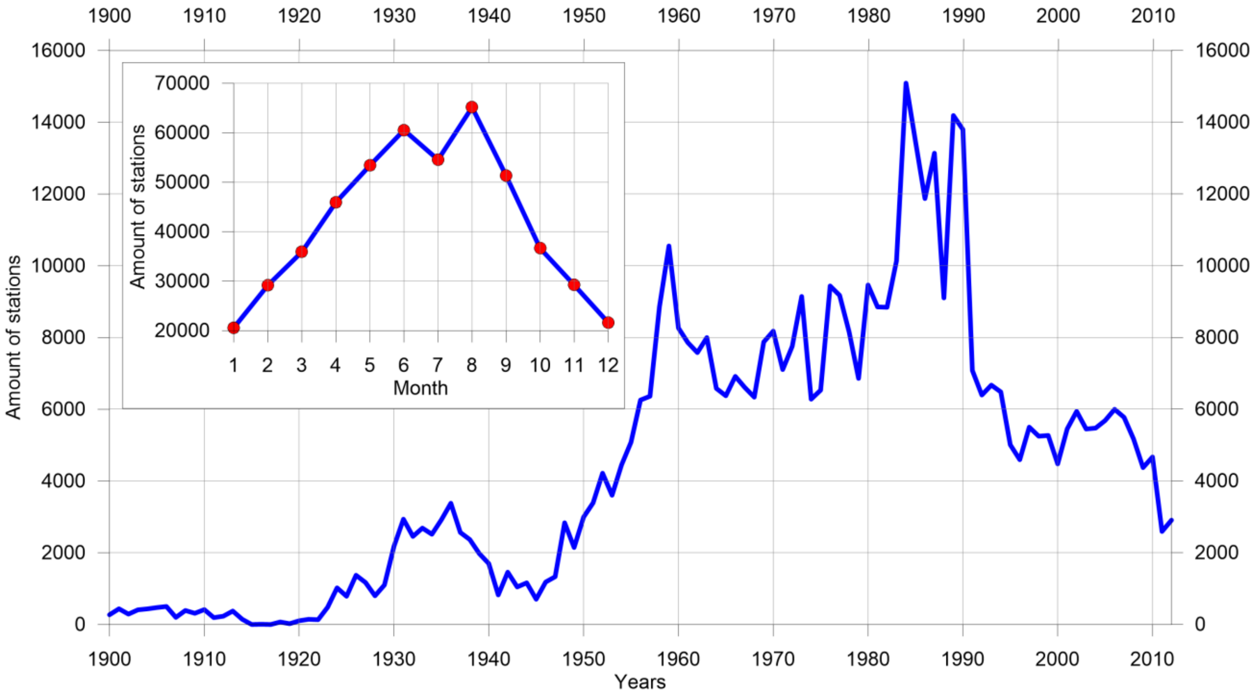

Figure 2.1 Stations distribution in the merged oceanographic database by years and by months.

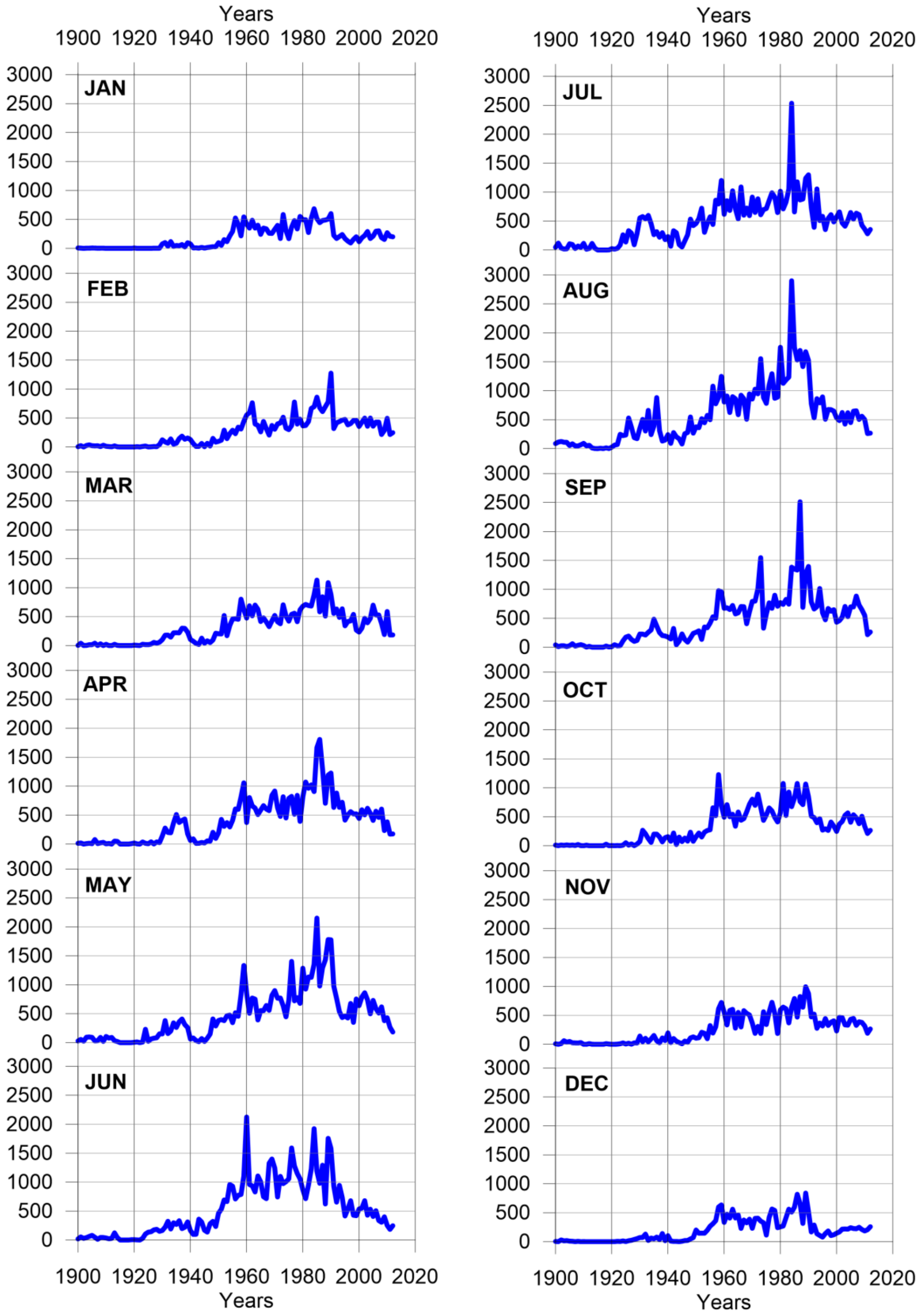

Figure 2.2 Time series of station distribution in the merged oceanographic database by months.

The remaining stations in the database (after the duplicate-removal and quality-control procedures) originated from 37 different sources as listed in Fig. 2.3. Ten major sources supplied more than 10,000 stations each, including the two sources with more than 100,000 stations. Combined contribution from WOD01 (Stephens et al., 2002), WOD05 (Boyer et al., 2005) and WOD09 (Johnson et al., 2009) amount to 121,493 stations. More than 120,000 stations were added from “The Climatic Atlas of the Arctic Seas” (ODB_CA, Matishov et al., 2004). Almost 64% of the identified stations (with complete metadata) belong to USSR/Russia (> 167,000) and Norway (> 156,000). Together with stations of unknown origin (> 61,000), it is more than 80 % of stations in the database. The large number of stations with insufficient metadata implies that even selecting from multiple data sources and using an algorithm designed to improve metadata content cannot restore a considerable part of information. It is also highlights importance of updating the station composition against the original reports.

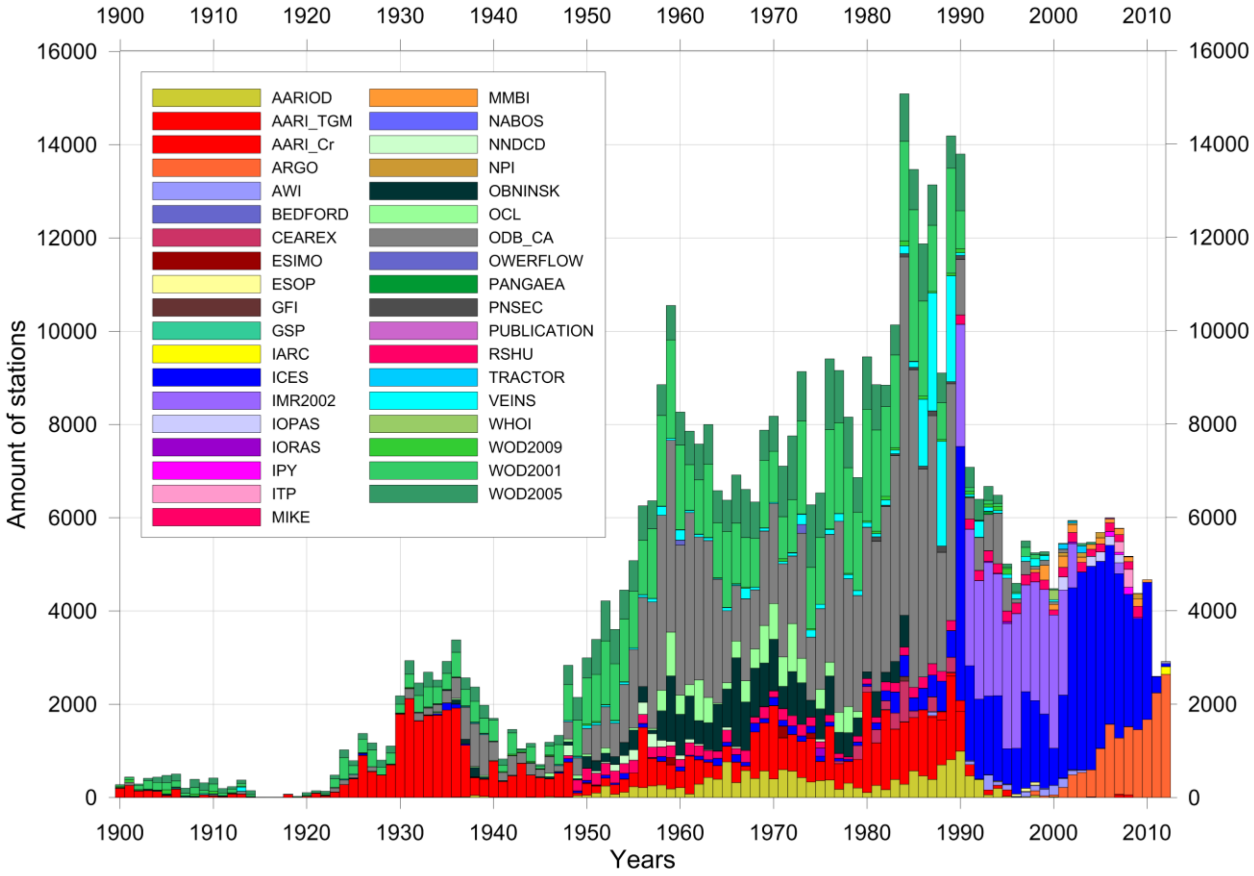

Figure 2.3 Stations distribution in the merged oceanographic database by years and by sources.

2.2 Update under GODAR project

The Global Oceanographic Data Archaeology and Rescue (GODAR) project was initiated in 1993 under the auspices of the International Oceanographic Data and Information Exchange (IODE) programme. It was further agreed that the National Oceanographic Data Center (NODC), USA would lead this project. Levitus et al., (2012) summarized GODAR objectives as data digitizing, rescue (if there is a danger of media decay), making available for international exchange, preparation of catalogues and performing quality control. The project played a major role in increasing the volume of historical oceanographic data available to the international scientific community. Along this path, 9 million temperature stations were included into the World Ocean Database 2009 (WOD09), two million more than in World Ocean Database 2001 (WOD01).

The AARI was involved in the GODAR project for 6 years, from 2006 to 2012. During that period, the number of stations in the database was significantly increased, while stations metadata and profiles composition were also improved. A large number of meteorological observations were added. As a result, 1,157 cruises that carried out almost 84,000 stations were verified and updated against the original cruise reports. A temporal distribution of the updated data is shown in Fig. 2.4 and a scatter plot of stations distribution by days and by years is presented in Fig. 2.5.

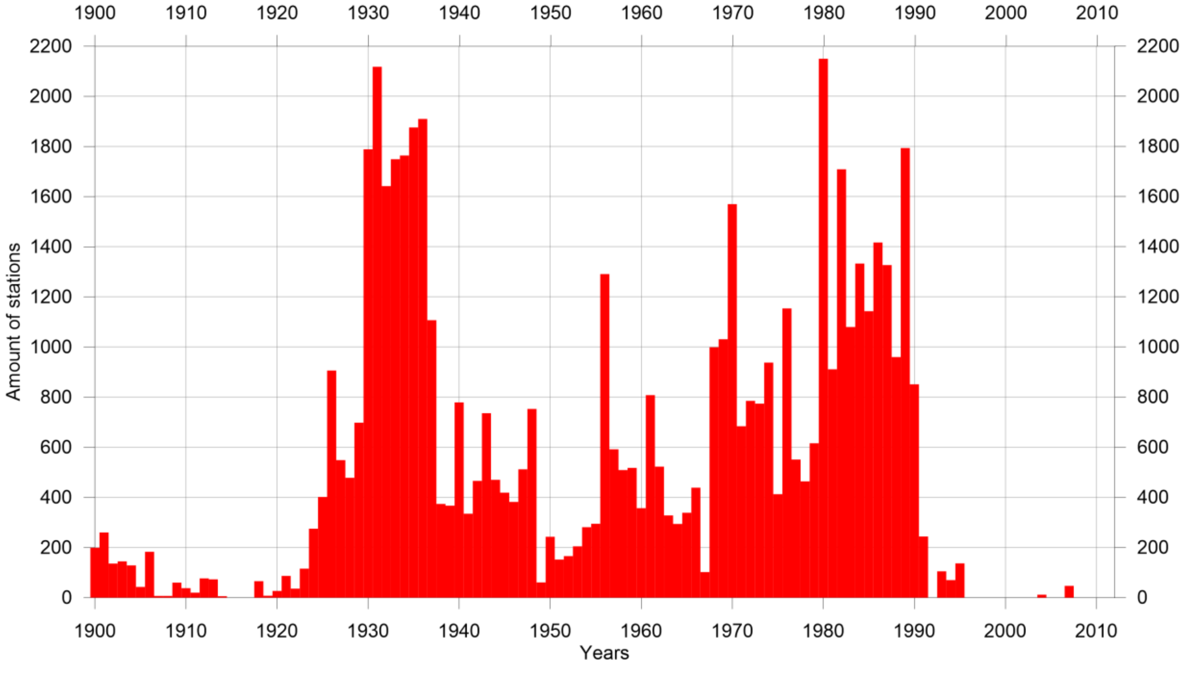

Figure 2.4 Number of stations updated under GODAR project.

A percentage of the updated data contribution into the database is shown in Fig. 2.6. It is important that the early periods (where data coverage is sparse) have been significantly updated.

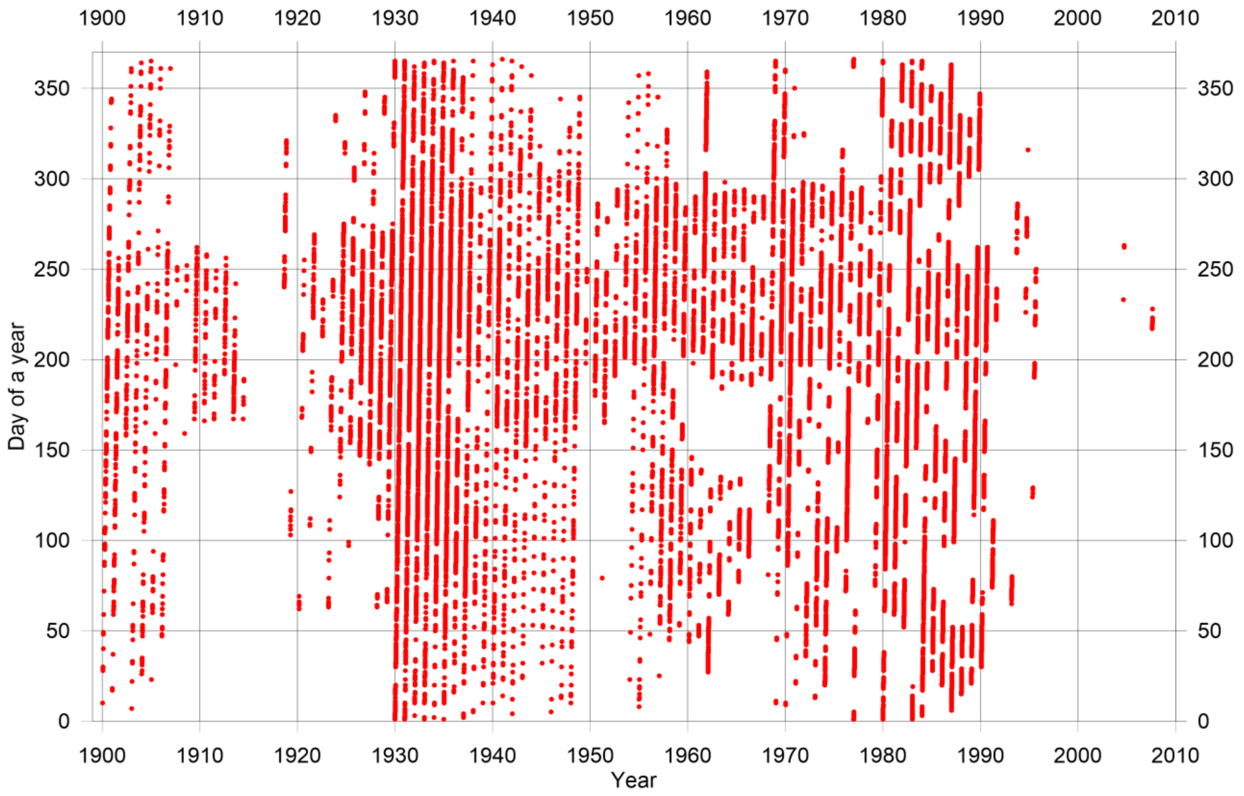

Figure 2.5 Station distribution by days and by years.

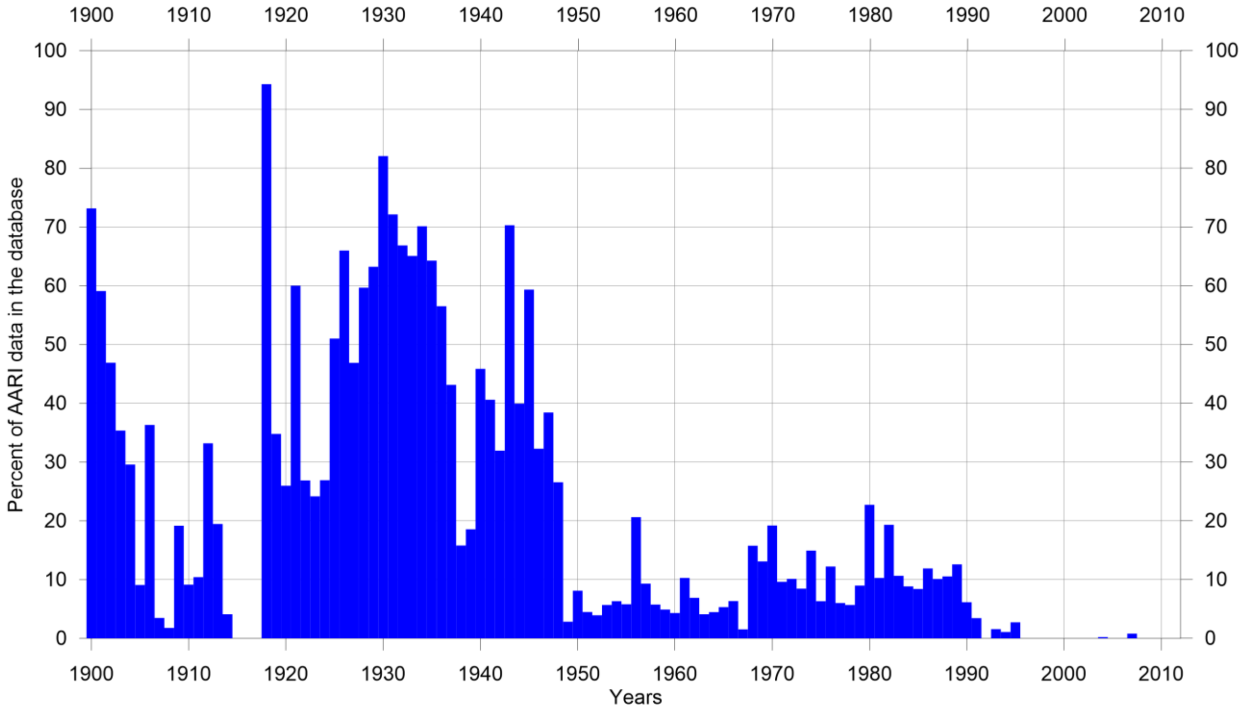

Figure 2.6 Percentage of verified AARI data in the database.

Major addition of historical observations corresponds to the 1900–1913 period (1,377 stations, 28 %) and 1918–1948 period (23,196 stations, 51 %).

2.3 Quality control

The database structure aims at maintaining information about the data quality and modifications during the data processing. A set of quality control flags was developed, attributed to a station as a whole or to each profile's value (Appendix, Table 7, Table 8). A sequence of algorithms was developed to check metadata integrity and verify consistency of temperature, salinity and oxygen profiles. The range check ascertains that a variable's values are within a realistic physical interval (i.e. impossible parameter check). The following intervals were applied: temperature from –2 °C to 20 °C, salinity from 0 to 40, oxygen from 0 to 20 ml/l.

Profile's depths passed through four procedures: (1) The vertical resolution of CTD profiles was reduced to 5 m above 400 m depth and 10 m below that depth, while preserving the original upper and lower levels depth intervals; (2) Depth inversions were detected and deleted; (3) For depth duplicates correction, both automatic and expert controls were applied. If the offsets for temperature, salinity and oxygen at the repeated levels were within a specified range (0.02 °C, 0.02, 0.05 ml/l), then the values were automatically averaged and corresponding quality control flags were assigned. If not, the profiles were sent to expert control with three options: (a) average all values or a subset of the duplicate values, (b) select one value, or (c) select most suitable value by comparison with value from the mean profile, computed by averaging profiles within a user specified area around the station. The algorithm was especially useful for the sources with a large amount of depth duplicate (e.g. OWS 'Mike'); (4) Profiles with less than three levels for T and S were eliminated. Compliance with such strong constrains requires deleting a large amount of stations, mainly with surface-only measurements.

The vertical stability algorithm assigns quality control flags if the density inversion criteria failed. Criteria (0.03 kg/m^3 for 0–30 m, –0.02 kg/m^3 for 300–400 m, and all negative gradients below) are similar to those used in WOD01 (Stephens et al., 2002). The flags are assigned both for temperature and salinity values.

Standard deviations algorithm assigns quality control flags in accordance with variability assessed from statistical analysis of a data sample selected in the vicinity of the analyzed observation. The sample was formed by gradually increasing the search radius in space and time from the observation (50 km, ±10 years) until a maximum (300 km, all periods). At each increasing step, the sample size (n), and the normality of the variable distribution was checked by means of a χ^2 test ($35 < n < 100$) and Kolmogorov–Smirnov test for small samples ($n < 35$). For $n > 100$, a normal distribution was assumed without tests. If the normal distribution was not achieved, standard deviations were not computed. For the observed-level database, samples were selected in the layers between the standard levels. The quality control flags were set 'on' if the observed value was beyond 3, 4 or 5 σ intervals, as shown in Appendix, Table 8.

2.4 Preparation for the analysis

In order to perform the interpolation (analysis), the observations (samples) need to be in a format supported by DIVA (Section 3). For this purpose a program module was embedded into the 'Ocean Shell' application (Section 4), which converts data from the database format directly to the DIVA format.

A vertical interpolation of the profiles data to standard depth levels is a necessary step for gridding. Different interpolation methods may produce significantly different results, especially in high-gradient zones and could be a source for large, off-the-books errors when accuracy of vertical interpolation is not estimated. Unfortunately, many profiles in some data sources have already been interpolated using undocumented algorithms, and therefore different sources contain different versions of the same profile. This situation emphasizes the importance of using original, observed-depth profiles, which, afterwards, might be vertically interpolated using the same uniform algorithm.

We use an algorithm based on three interpolation methods: linear, Lagrangian and Reiniger–Ross (Reiniger and Ross, 1968). The algorithm is similar to the one used in WOD05 (Boyer et al., 2006), but with the following important modifications: (1) more strict criteria for distances between observed and interpolated depths, (2) – linear increase of the criteria with depth, in contrast with the three-level approach in WOD05, (3) additional limitations on applying nonlinear methods (interpolated value cannot exceed the nearest values on a vertical profile by more than 20%). These restrictions prevent generation of artificially induced outliers in the interpolated profiles. As in WOD05, all measurements with a depth less than 5 m are considered to be surface observations.

Finally, several standard-level datasets were downloaded from the database for the area bounded by 58° N – 84° N and 47° W – 72° E, and then used as an input for DIVA analysis. All types of derived gridded fields are listed in Table 1 in the 'Atlas Content' Section.

3. METHOD OF SPATIAL DATA INTERPOLATION

3.1 DIVA description and installation

The Data-Interpolating Variational Analysis (DIVA) is a method designed for interpolating irregularly-spaced, noisy data onto any set of grid points, in most cases on a regular grid. It is a combination of a specially designed methodology and an efficient finite-element numerical method Troupin et al., (2010, 2012, 2013). The methodology is based on minimization of a cost function that penalizes the misfit between the observations and the reconstructed field and ensures smoothness of the field. The method bears some similarities to the smoothing splines, where the second derivatives of the field are also penalized.

DIVA allows the spatial interpolation of data (analysis) in an optimal way, comparable to optimal interpolation (OI). In comparison to OI, it takes into account coastlines, subbasins and advection by currents. Calculations are highly optimized and depend on a finite element resolution. The tools for generating the finite element mesh and the tools to optimize the parameters of the analysis are provided. Quality control of data can be performed and error fields can be calculated. Also, data can be de-trended. Finally, 3D and 4D extensions are included with an emphasis on direct computations of climatologies from the Ocean Data View (ODV) spreadsheet files.

The advantages of the method are in taking into account topographic and dynamic constraints (coasts, advection, etc.) and its capacity of handling large data sets inherent to oceanography. The method yield gridded fields in two dimensions, usually in horizontal layers. Three-dimensional fields are obtained by horizontally stacking two-dimensional gridded fields (Troupin et al., 2012).

Details of the method are provided in Troupin et al., (2010, 2012, and 2013) and can be found on the DIVA project's WIKI page (modb.oce.ulg.ac.be/mediawiki/index.php/DIVA).

Here we employed GODIVA version dated April 2012 (GODIVA_03_2012c). It was recompiled and run on three computers with Windows 7, Windows 8 and Linux Mint 14 operational systems. In all cases a gFortran compiler (gcc.gnu.org/wiki/GFortran) was used. On Windows PCs, DIVA was run under Cygwin environment (www.cygwin.com).

3.2 Interpolation parameters

DIVA requires a parameter file and topography contour for each computed field. In this Section we describe every entry in the parameter file.

Topography

After getting the initial data ready for analysis, it is necessarily to create topographic files. The GEBCO Atlas with 30 second resolution (BODS, 2003) was chosen as *the* source for bottom topography in the Nordic Seas Atlas. The region of interest was selected with 2- degree offsets from the gridded field area (58° N – 84° N and 47° W – 72° E) to ensure proper coverage of the Atlas region. We extracted data from GEBCO using standard BODC software and then processed it using DIVA tools. A 30-second grid was too detailed for large scale analyses so a courser resolution grid was creating using a subset taking every fifteenth grid point of the original 30-second grid. The resulted bottom topography has sufficient resolution for 0.25-degree oceanographic analysis. . Then all the necessary steps described in (Troupin, 2013) were completed and twenty nine files with standard depth contours (0, 10, 20, 30, 50, 75, 100, 125, 150, 200, 250, 300, 400, 500, 600, 700, 800, 900, 1000, 1100, 1200, 1300, 1400, 1500, 1750, 2000, 2500, 3000 and 3500 m) were prepared for the analysis. Finally, the topography contours were plotted and double-checked visually.

Correlation length

The correlation length *(L)* is the distance over which a given data point influences its neighborhood. Similarly to other interpolation techniques, it is an essential parameter for obtaining meaningful results. The value of L can be provided a priori by the user, or determined using the data distribution.

We used our complete data set to determine L by applying the internal DIVA algorithm called *divafit*. Correlation lengths were calculated for every month at each level. It mostly depends on data spatial distribution rather than seasonal variability (Troupin, 2010) because we averaged L values to generate a single vertical profile of the correlation length (Fig. 3.1)

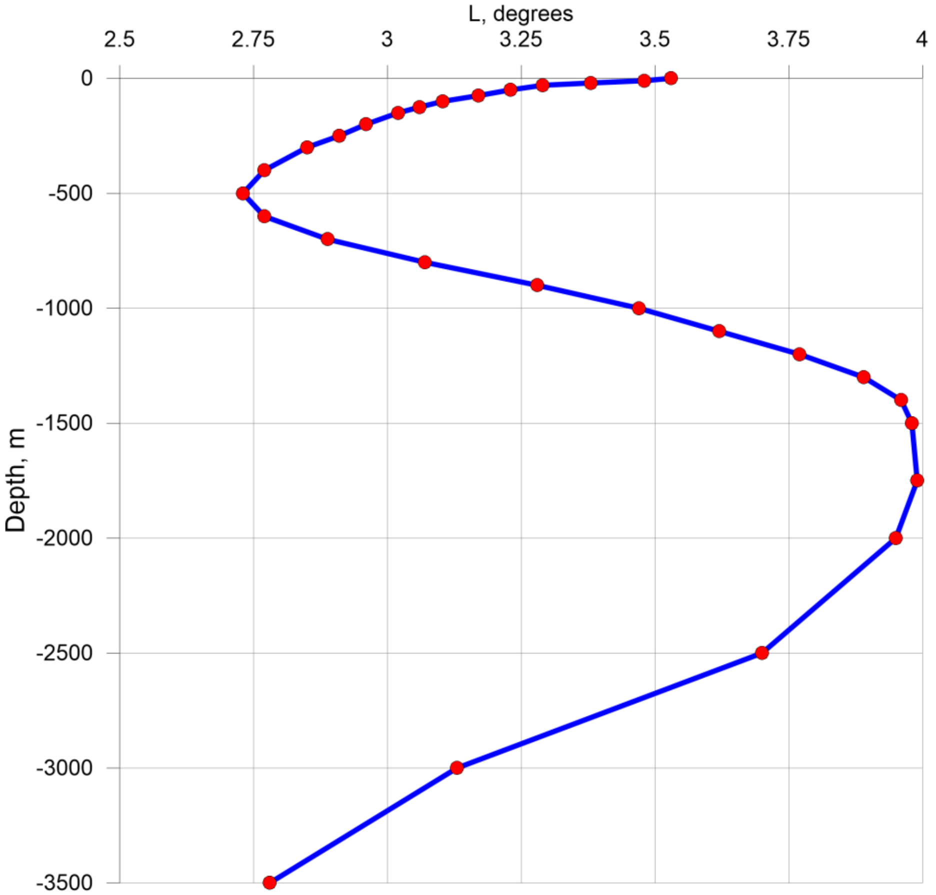

Figure 3.1 Vertical distribution of correlation length L (in degrees).

Change of coordinates

icoordchange specifies the desired type of coordinate system. DIVA operates in kilometers. *icoordchange*=1 indicates that data position is given in geographical coordinates (degrees) and has to be converted into kilometers.

Error outputs (ispec)

Of the three types of errors that can be calculated using DIVA (Troupin et al., 2013), we selected to compute errors with the real covariance function and to obtain the error field at the same grid as the 0.25-degree resolution climatological fields, which requires ispec=–1.

Specification of the background field which is subtracted from the data field (ireg)

The *ireg*=1 was chosen (the data mean value is subtracted)

xori/yori, nx/ny, dx/dy

xori/yori indicates the coordinates of the first grid point, while nx/ny indicates the number of grid points in x/y directions. In the Atlas, xori=–47, yori=58, dx=dy (step of output grid)=0.25; nx=476, ny=104

Exclusion value (valex)

The exclusion *valex* value is –9999.

Signal-to-noise ratio (λ)

When measuring a variable, there is always an uncertainty (noise) due to instrumental errors or variable fluctuations on different time scales caused by unresolved sub-grid physical processes. Noise not only takes into account instrumental error (which is generally low), but it also includes:

- the representativeness errors, meaning that what one measures is not always what ones intends to analyze (e.g., skin temperature, inadequate scales)
- the synopticity errors, occurring when the measurements are assumed to be taken at the same time (e.g., data from a cruise)

Because of multiple sources of error, a perfect fit to data cannot be achieved. The choice of λ is not straightforward. In the case of climatology, the error is not only instrumental, but comes also from representativeness errors: a climatological field (hence representative of long time scales) is represented using measurements coming from several surveys (hence having shorter-scale variability). Unfortunately, this kind of error cannot be easily quantified (Troupin et al., 2010).

To limit computational cost, due to the large volume of initial data, we set λ to be constant. Two values were used (1) λ=50 for monthly fields (highly homogeneous dataset within a single month of a single year), and (2) λ=5 for the rest.

Variance of the background field

Any field can be defined as a sum of a background field and an anomaly. The background field is the first guess of the field to reconstruct (Troupin et al., 2013). In the current implementation, we use two kinds of variance of the background field: (1) mean values that depend only on depth (for long term means, Fig. 3.2) and (2) values which vary with depth and annual cycle (for monthly fields) (Fig. 3.3).

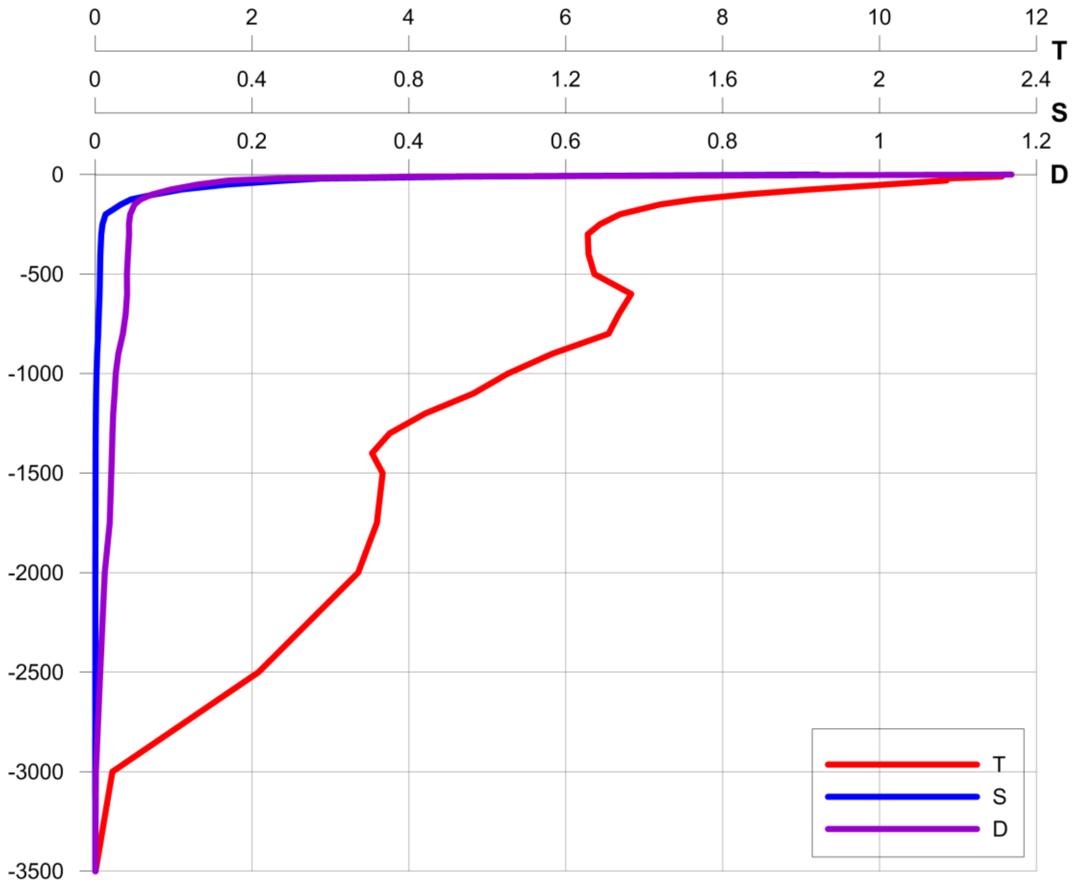

Figure 3.2 Vertical distribution of the variance of background fields for mean annual data. (T – water temperature (^{o}C), S – salinity, D – density (kg/m^3))

Monthly fields were obtained for every parameter and smoothed both vertically and monthly by applying the running averaging. Artificial spikes were removed manually. Annual profiles (Fig. 3.2) were obtained by averaging of monthly fields.

Practically, the computation of the gridded fields consisted of executing of the described parameters files in a batch mode.

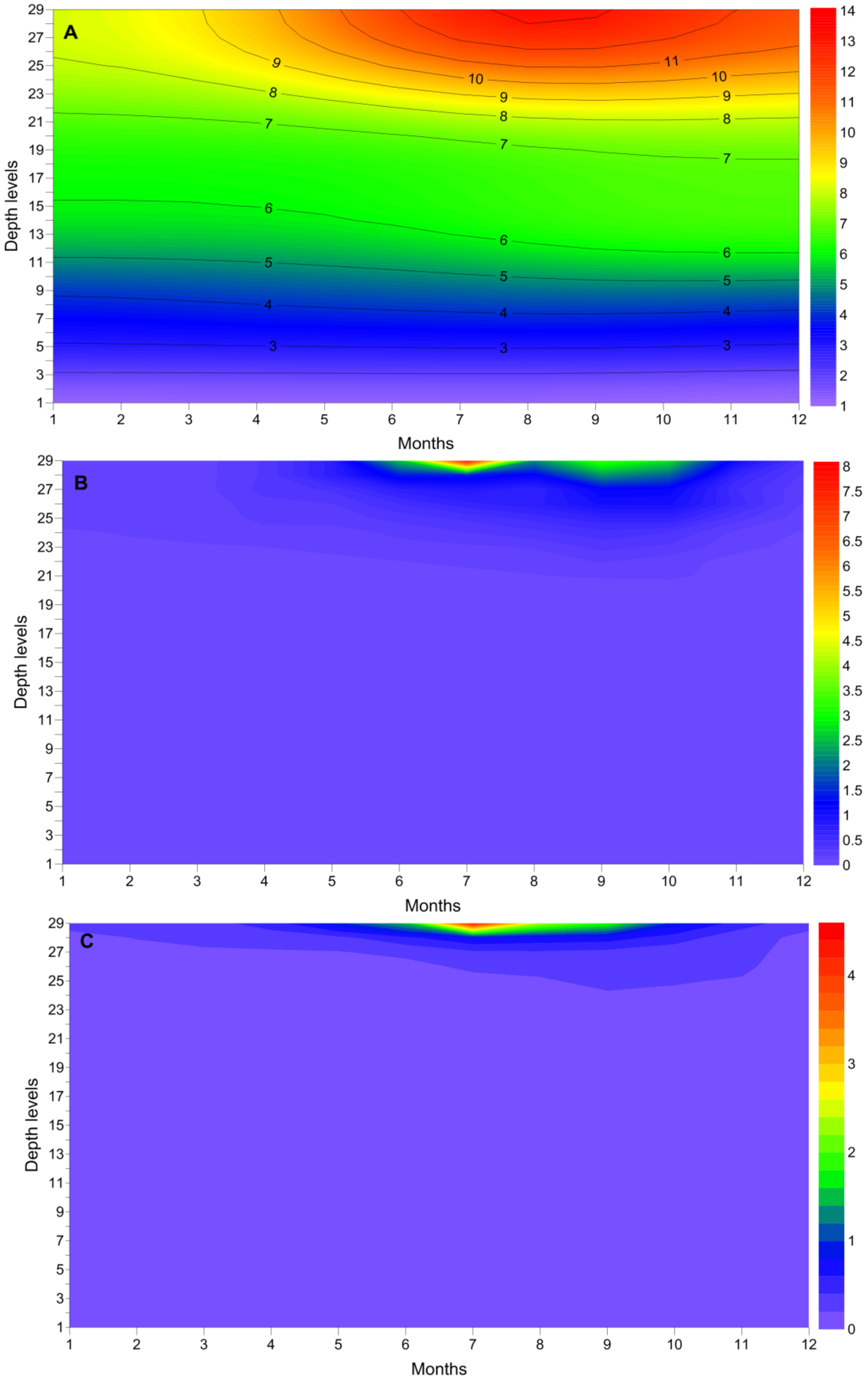

Figure 3.3 Monthly variance of the background field by depth. (A) – temperature, (B) – salinity, (C) – density. Depth level 29 corresponds to the surface, number 1 to 3500 m.

3.3 Mesh creation

The finite-element mesh is based on specified contours (bottom topography) and the correlation length *L* (see sec. 3.2) provided by user. Topography contour segments should not be much smaller than finite element length. If the contour has too fine resolution it should be reduced. In addition, the typical length of a finite element should be smaller than the correlation length, otherwise the grid would be too coarse compared to the signal to resolve (Troupin et al., 2010). An example of the mesh is shown at Fig. 3.4

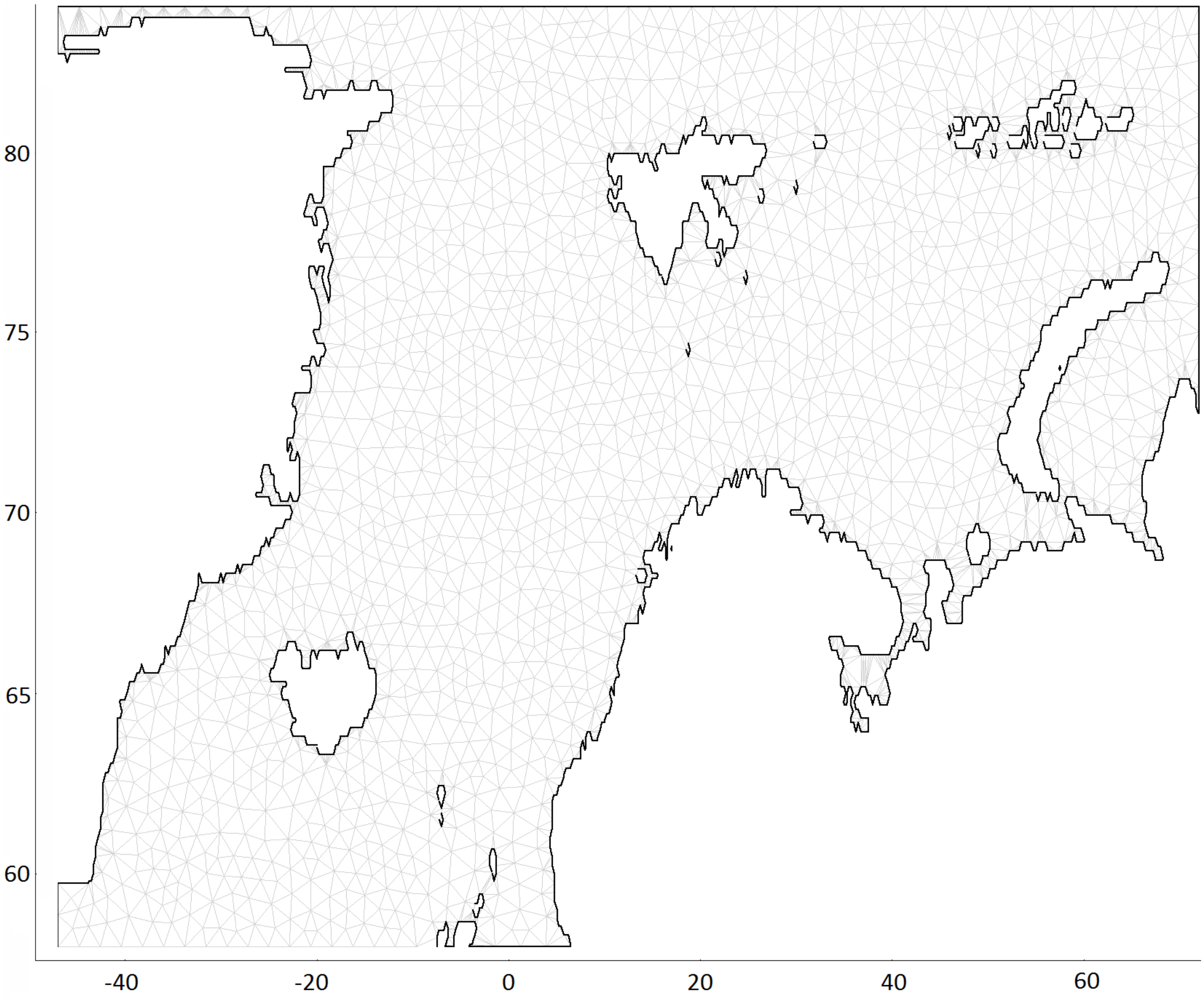

Figure 3.4 Mesh used for calculation of the Nordic Seas domain.

3.4 Running the analyses

After generating all initial data and parameter files, the analysis was run to create interpolated fields of chosen oceanographic parameters. The current version of DIVA (GODIVA_03_2012c) is not a multi-threaded software. Therefore, to speed up the calculations, three PCs with 4, 6, and 8 cores were used in parallel. Monthly fields were interpolated level by level and then combined into annual files (12 monthly fields at 29 levels yield one annual field at those levels).

3.5 Output

The results are included in the Atlas in the form of gridded fields in NetCDF (Network Common Data Form) format and visualized as maps showing different data integration periods from month to decades and even longer periods (see Atlas content, Table 1).

The NetCDF format provides a set of interfaces for array-oriented data access and a freely distributed collection of data access libraries for C, FORTRAN, C++, Java, and other languages. The NetCDF libraries support machine-independent format for representing scientific data. Together, the interfaces, libraries, and format support the creation, access, and sharing of scientific data (Rew et al., 1997).

4. SOFTWARE FOR DATA PROCESSING, ANALYSIS AND VISUALISATION

4.1 'OceanShell' application description and functionality

The 'OceanShell' application is a software package for oceanographic data storage, interactive exploration, analysis and visualization. For data storage, the Interbase 7.0 server (www.embarcadero.com/products/interbase) was chosen to accommodate an appropriate ratio between the processing power and cost. Alternatively, 'Firebird', an open-source database server can be used (www.firebirdsql.org). The program code is written in the Embarcadero Delphi 2010 Professional Environment with embedded Interbase components (IBX). This environment supports client-server architecture, Structured Query Language (SQL) and a variety of internal or additional (optional) commercial components. This setup allows developing database applications with multiuser network access. The software runs on MS Windows 8, 7, Vista and XP.

The 'OceanShell' application has all functionalities required for processing oceanographic data: selection, filtering, sorting, editing, inserting, deleting, gathering of the statistical information etc. The selection module provides both basic and advanced data search options. The basic-option search allows selecting data by combination of coordinates, data/time, country, vessel, source, cruise and instrument. Advanced search offers more sophisticated algorithms: stations selection around a specified point or section inside an arbitrary region by stations depth, by quality flags etc. There is also an option to use a custom SQL query. Selected stations metadata and profiles are shown in a tabular form, while stations position is displayed on a bathymetry map. The map is resizable and interactive, i.e., allowing navigation among and selection of specific stations). Additionally, the application maintains a catalog allowing the stations to be grouped by a range of attributes – vessel name, standard section or surveys, repeated stations at fixed position, project data and others. The catalog, therefore, gives another way of selecting data quickly and conveniently.

The graphical interface allows inspecting profiles, vertical sections, horizontal maps, T/S diagrams, time-depth diagrams etc. The Surfer (www.goldensoftware.com) graphical automation functions are embedded into the 'OceanShell' application facilitating high-quality plotting of the processed data.

Export and import procedures support data conversion between several formats (DIVA, WOD, ODB text/database, ICES, ODV etc.).

The statistical module generates various database content information in tabular or graphical form.

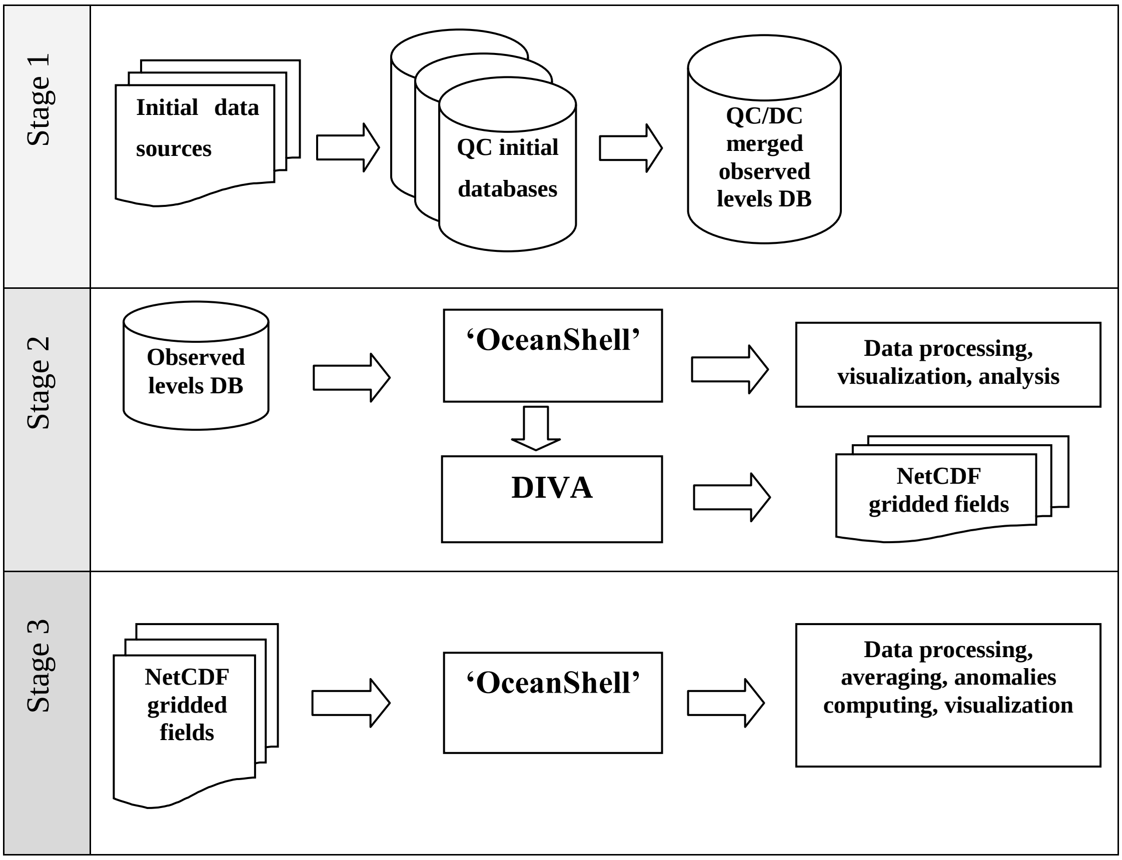

Figure 4.1 Functionality of the 'OceanShell' application (DB stands for database, QC – quality control, DIVA – Data-Interpolating Variational Analysis, NetCDF – Network Common Data Form).

There are several modules for computing specific oceanographic characteristics included in the software package. For example, the mixed layer depth can be determined using three different algorithms – threshold, gradient and curvature-based analysis. Also, heat content, dynamic heights and freshwater content can be computed. Information about sea-ice concentration can be stored in the database and the sea ice edge can be plotted.

The schematic diagram in Fig. 4.1 illustrates three stages of the data processing for preparing the data for spatial analysis and processing of gridded fields. The first stage includes data downloading procedure, the database structure and all the necessary technological steps were described in Section 3 (see above). At the second stage, data are converted into DIVA format. Finally, at the third stage, after completing the analysis, the output fields are transferred to the modules that generate and process the NetCDF files. These modules allow averaging of the gridded fields, anomalies computing between any two fields, as well as plotting of fields, time-series and time-depth diagrams.

To summarize, the ‘OceanShell’ application provides a sophisticated and practically autonomous tool for the entire oceanographic data processing procedure – from the initial data downloading to sophisticated processing of climatological fields.

5. TIME-DEPTH DIAGRAMS

5.1 Definition, geographical locations and computing algorithm

5.1.1 Definition

Time-Depth Diagrams (TDDs) are designed for displaying oceanographic parameters variability in space of time and depth at selected geographical locations. The parameters are shown on TDDs as anomalies (Section 5.1.4) representing their area-averaged monthly-mean time series. The diagrams are based on *in situ* observations. They are included in the Atlas to demonstrate regional changes of selected oceanographic parameters in the Nordic Seas and northern North Atlantic and to provide additional visual information for consistency check of the gridded horizontal fields.

5.1.2 Geographical locations of TDDs

Twelve areas in the Northern North Atlantic and the Nordic Seas were chosen for computing TDDs based on the long-term observational programs available at those locations. The areas' configuration and size (Table 2) were determined by available spatial and temporal distributions of the stations in the vicinities of TDDs locations. The diagrams were created using data from numerous field programs. Over the years, different countries, marine organizations and research projects employed diverse observational strategies. Individual subsets are dominated by profiles clustering either around either a single location (OWSA, OWSI, OWSM) or distributed along standard sections (FSS, KS) or originated from polygon surveys (LB, GB), at least for certain extended time periods. Unfortunately, localized observations from ocean weather ships, which provided uniform and consistent time series, were terminated for a long time ago. Therefore, the time series of this nature were extended using data from ships of opportunity and more recent data from Argo profiling floats (www.argo.ucsd.edu).

5.1.3 Data availability and quality control

Data for TDDs were extracted from our oceanographic database (version: March 2012). Profiles obtained by three types of instruments (CTD, bottle and profiling floats) together with some profiles of unknown origin were all merged together. The XBT profiles were not included because of the known XBT bias problem (Gouretski & Kolterman, 2007).

Table 2. Specifications of areas and profiles selected for the regional time-depth diagrams

Abbr.	**Central point**		**Radius (km)**	**Num. of Stations**	**Period**	**Num. of profiles**			
	Lat	Lon				T	S	D	O2
I	59.00N	19.00W	100	2,605	16.09.1929 10.01.2012	2,600	1,062	1,057	140
A	62.00N	33.00W	150	2,837	17.06.1895 26.03.2012	2,831	2,724	2,720	480
FSC	61.00N	3.16W	70	4,845	31.07.1896 13.05.2011	4,840	4,758	4,753	1,492
DS	66.20N	27.00W	100	2,233	4.06.1895 30.07.2011	2,232	2,178	2,177	751
M	66.00N	2.00 E	50	12,458	2.07.1935 2.09.2011	12,440	12,102	12,086	1,978
EIC	67.50N	12.40W	150	4,782	23.06.1891 23.10.2012	4,780	4,309	4,307	1,335
LB	70.00N	3.00E	100	1,390	11.08.1900 29.02.2012	1,390	1,269	1,269	409
GB	75.00N	2.00W	100	2,401	25.06.1901 15.03.2012	2,399	2,142	2,141	521
FS75	75.00N	12.00E	100	2,669	5.07.1871 18.04.2011	2,668	2,263	2,262	568
FSRA	77.00N–79.50N	0.00–10.00E		5,439	10.07.1871 20.10.2012	5,438	4,814	4,813	909
BSO	72.80N	19.50E	100	8,713	1.07.1871 24.01.2012	8,713	7,694	7,694	1,397
KS	77.00N–79.50N	33.10E–33.50E		14,492	14.07.1882 29.08.2010	14,486	12,229	12,224	2,546

I – Ocean Weather Ship India (OWSI); **A** – Ocean Weather Ship Able/Alpha (OWSA); **FSC** – Faroe Shetland Channel; **DS** – Denmark Strait; **M** – Ocean Weather Ship Mike (OWSM); **EIC** – East Icelandic Current; **LB** – Lofoten Basin; **GB** – Greenland Basin; **FS75** – Fram Strait 75° N; **FSRA** – Fram Strait Recirculation Area; **BSO** – Barents Sea Opening; **KS** – Kola Section.

Despite a relatively low number of dissolved oxygen profiles, oxygen TDDs were added to the Atlas along with temperature, salinity and density diagrams. Although scarce data availability makes oxygen diagrams not fully compatible with much better substantiated temperature and salinity diagrams, oxygen is an important tracer for horizontal and vertical advection and mixing. Inclusion of the oxygen TDDs is therefore justified.

The data have passed standard quality control described in the Section 2.3. Additionally, the profiles were plotted together for each of the 12 areas for visual inspection, with outliers, if any, removed from further processing. The outliers that survived the first pass of quality control were mainly caused by small scale processes (shelf processes, frontal zones) or erroneous measurements that escaped filtering out by the standard quality control procedures. Therefore, the magnitude of variability within the areas (Table 2) is most likely underestimated rather than overestimated in the TDDs. Measurements prior to 1950 often show excessive variance due to the generally lower accuracy of historical observations. Nonetheless, early observations provide an important evidence of processes, help to extend our time series and better assess anomalies' recurrence and magnitude on a longer time scale.

5.1.4 Computational algorithm and plots design

The diagrams were plotted after the following steps in data processing:

- For each area (Table 2), station subsets were extracted from the database. One of the two configurations for a selected area was used: (i) a circle with certain radius around a central point; and (ii) a rectangle fitting a section or area (Fig. 5.1). The sizes of the areas were determined to compromise between data availability and regional features of variability (with exclusion of divergent processes).
- For each subset, stations' metadata were stored in the database's catalog for further processing.
- An additional quality control was applied to temperature, salinity, density and oxygen (profiles visual inspection).
- The profiles were interpolated at standard depths using weighted parabolic interpolation algorithm (Reiniger and Ross, 1968 and section 2.4 for details).
- The mean monthly profiles were computed by averaging observed profiles.
- The mean annual cycle for each parameter and each standard depth was defined by averaging monthly values for the years 1950–2000.
- The monthly mean values at standard depths were converted into the values with annual cycle removed by subtracting the mean annual cycle.
- Finally, the anomalies of monthly mean values (with annual cycle removed) were computed by subtracting the mean values for the reference period of 1950–2000.

The outlined algorithm is an embedded module of the 'OceanShell' software (Section 4). The TDDs in the Atlas represent monthly anomalies (with the annual cycle removed) relative to the 1950–2000 period. The program module allows the user to compute the diagrams with variable temporal averaging, reference periods and with or without the annual cycle. We compared several versions and found that basic anomalies remain quite similar while details can vary. Including of the annual cycle provides slightly less intense variability in the upper ocean that highlights the large-scale anomalies.

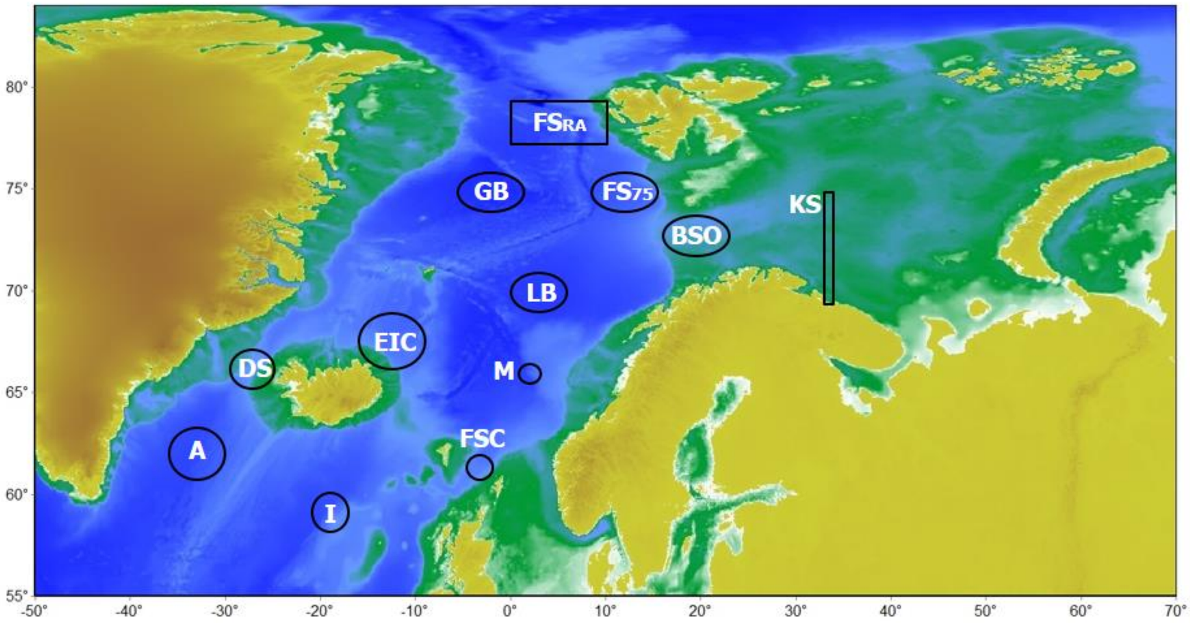

Figure 5.1 Areas for computing the time-depth diagrams (A – Ocean Weather Ship Able/Alpha (OWSA), I – Ocean Weather Ship India (OWSI), FSS – Faroe Shetland Channel, DS – Denmark Strait, M – Ocean Weather Ship Mike (OWSM), EIC – East Icelandic Current, LB – Lofoten Basin, GB – Greenland Basin, FS75 – Fram Strait 75° N, FSRA – Fram Strait Recirculation Area, BSO – Barents Sea Opening, KS – Kola Section). Background map shows smoothed ocean bathymetry and land topography extracted from ETOPO1 global relief model (www.ngdc.noaa.gov/mgg/global).

Two different types of diagrams can be seen on the web (www.nodc.noaa.gov/OC5/nordic-seas/atlas/diagrams.html): the first type shows the anomalies in the upper 500 m, while the second type covers the depth range from the surface to the last standard interpolated depth level. The depth range depends on the bottom depth at site and on data availability in deeper layers. Identical horizontal and vertical scales in all diagrams makes it easier to compare TDDs at different locations, whereas the full depth plots reveal the vertical extents of anomalies' and show the connection between deep and upper ocean processes.

All TDDs are accompanied by plots showing the data node positions used for mapping. The color of a node signifies that a number of observations were available for computing the monthly mean value from *in situ* observations at a given position. Additional constraint for TDDs required masking of the periods with more than two years gaps in data (white vertical strips overlaying TDDs). Closer to the surface, there is a narrow white horizontal bar (particularly noticeable in plots on the web page) indicating that data filtering was applied. It is wider for the plots of the data in upper 500 m.

5.1.5 Focus on regional variability

The TDDs demonstrate variability at key locations caused by different processes. Specifically, they help to trace anomalies or climatic signals advected by ocean currents or redistributed by vertical processes. In order to obtain a clear regional signal and avoid the impact of divergent processes, an area chosen for a TDD needs to be relatively small. Ideally, the size of the area should not exceed the correlation radius for the specific sea region. According to DIVA (Section 3), an averaged correlation radius for the region is between 2 and 4 latitude degrees. Therefore, in most cases the TDDs satisfy this criterion (Fig. 5.1).

5.2 Abnormal hydrographic regimes and events

The temporal-spatial pattern of temperature, salinity and density anomalies (Section 5.1.4), as seen in the time-depth diagrams at 12 locations (Fig. 5.1), yield valuable additional insights into variability of the water mass properties and regularities in emergence, propagation and, finally, decay of the anomalies. Indeed, the variability at selected areas is represented by anomalies with different magnitude, duration and vertical extent. The diagrams facilitate following the anomalies modification *en route*, as well as vertical propagation conditioned by the upper-ocean stratification and by intensity of atmospheric forcing.

The time series of anomalies in the Faroe-Shetland Channel, the longest time-series of all datasets, allows monitoring of both the upper ocean inflow and the deep overflow. Over the time period between 1896 and 2012, at least four strong negative and three positive anomalies can be distinguished (Fig. 5.2). As a rule, although temperature, salinity and density anomalies are generally coherent, the density anomalies are mostly thermally driven. In other words, the positive temperature and salinity anomalies, in most cases, are less dense than the negative anomalies due to predominant temperature contribution to the density. Therefore the upper-layer density absolute minimum in the record (labeled as ‘D3^{-}‘event, continuing since 2000) is caused by a strong temperature rise within the inflowing Atlantic water, regardless of the accompanying salinity increase. However, in some cases this relation is not dominant. The noticeable warm event from the mid-1950s to the mid-1960s passed through the phases of negative and positive density. The later state was caused by a strong atmospheric cooling of water with elevated salinity. Likewise, a strong salinity decrease during the Great Salinity Anomaly (GSA) propagation (Dickson et al., 1988) resulted in density decrease, despite of the substantial water temperature decrease during that event.

The oxygen anomalies (Fig. 5.2, bottom panel) change sign from positive to negative around 1970. This can be interpreted as an increased volume of the oxygen-rich intermediate waters compared with *en route* vertical transformation of the Atlantic water with reduced oxygen concentrations. In the upper layer, oxygen variations are most likely linked to changes in temperature. A strong positive anomaly around 500 m depth timed between the mid-1990s and mid-2000s can be possibly associated with the subsurface low-salinity anomaly transported from the Arctic Ocean.

Anomalies often intensify under the surface ($T1^-$, $T2^-$, $T2^+$, $T4^-$). That may be explained by the two-layer water mass structure in the Faroe-Shetland Channel. Vertical migration of the sharp gradient zone between the warm/salty Atlantic and cold/fresher underlying waters can generate substantial anomalies. Most of the anomalies in Fig. 5.2 are well mixed vertically, but at the end of the record, after the year 2000, a two-layer structure emerged. It might reflect opposite trends in the upper (warming) and intermediate (cooling) water masses, although it seems that the variability typical for the upper layer penetrates progressively deeper.

Most of the anomalies found in the Faroe-Shetland Channel can be traced both to the south and north of the Channel, while TDDs in the vicinity of the East Greenland Current (in Denmark Strait) and the East Icelandic Current (DS, EIC in Fig. 5.1) display fluctuations that are unique to those locations.

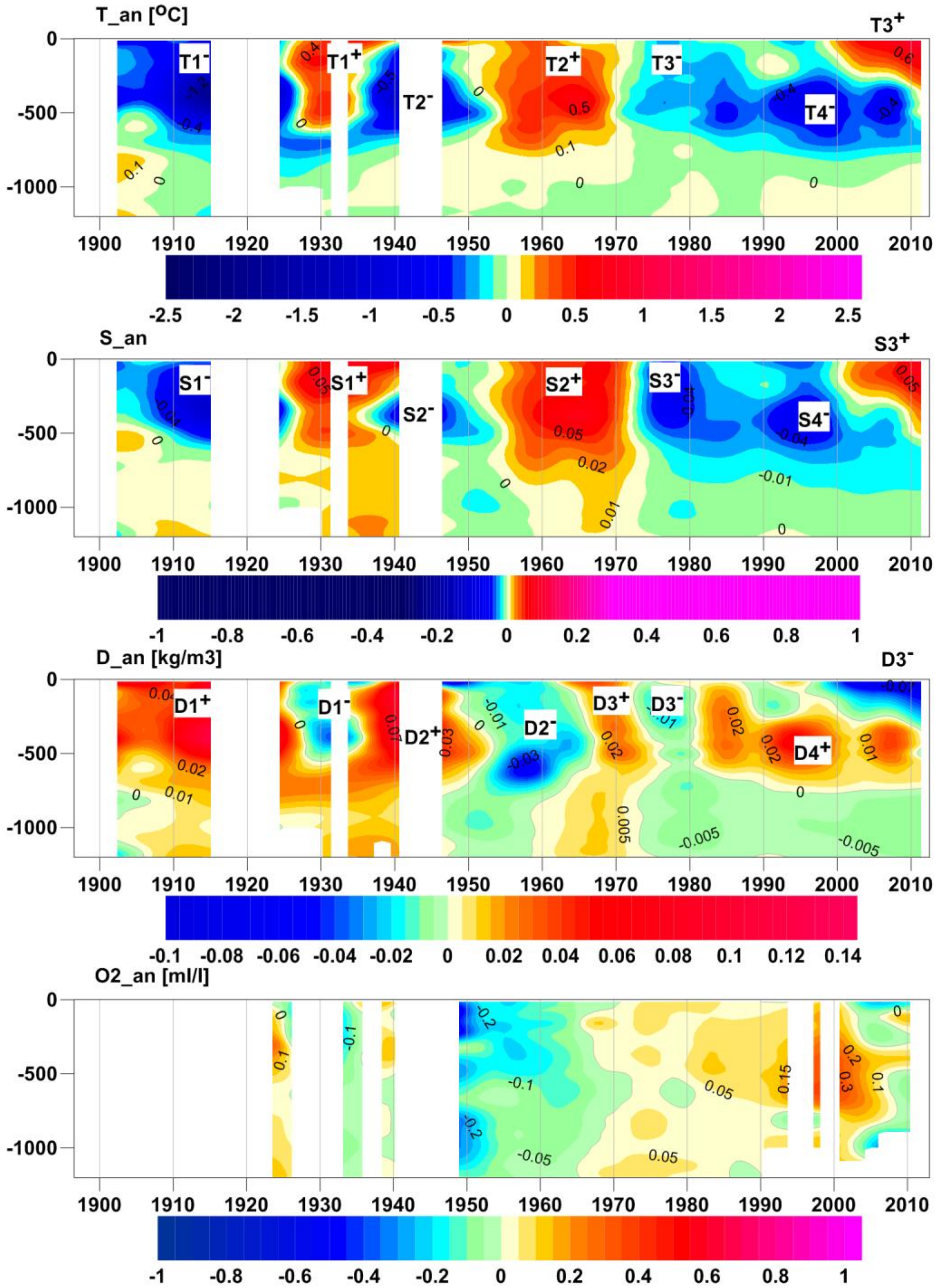

Figure 5.2 Time-depth diagrams of temperature, salinity, density and oxygen anomalies at the Faroe-Shetland Channel. Strong positive and negative anomalies are marked by ‘T’, ‘S’ or ‘D’ for temperature, salinity and density.

The composite plots of temperature, salinity and density diagrams for all 12 areas are included to demonstrate the generalized picture of variability in the Nordic Seas (Fig. 5.3–5.5). The composite plots consist of two panels for each set. The upper panels represent a comparable variability in the upper 500 m, while the bottom panels are plotted in full depth range specific to each location. The time-depth diagram at Faroe-Shetland Channel is used to label the major anomalies, while other referred events are also marked. In the full-depth diagrams only the anomalies below 500 m are labeled to show relationships with the top layer. According to the diagrams, the variability of thermohaline characteristics from 1900 to 2012 can be described as following:

1. Fragmentary observations prior 1950 contain evidence of two opposite regimes: cold and low salinity regime during the first two decades of the 20th century ($T1^-$, $S1^-$, $D1^+$) and warm and high salinity regime that lasted from the late 1920s to the end of the 1930s ($T1^+$, $S1^+$, $D1^-$). The first regime is associated with the early 20th century strong low salinity anomaly propagation (Blindheim et al., 2000). The period also contains a subsurface event ($T2^-$, $S2^-$, $D2^+$). However, this event is not fully supported by data. Its origin is perhaps similar to another, a much better documented event of the mid-1990s ($T4^-$, $S4^-$, $D4^+$). A low salinity dominated in the Barents Sea during the 1920s and 1930s, according to the measurements, at Kola section, in contrast to most other locations.
2. More abundant after 1950 data suggest that the generally warm and salty upper layer conditions in the part of the northern North Atlantic Ocean included in the Nordic Seas Atlas lasted until the onset of the Great Salinity Anomaly (GSA) that occurred in the mid-1970s, albeit with some exceptions. At OWSA location, for example, warming started only at the end of the 1960s.
3. The onset of the GSA is dated as mid-1960s and was associated with large ice and freshwater discharge from the Arctic Ocean. It can only be seen in the upper layer of the Arctic part of the Nordic Seas Atlas (DS, EIC) in the second part of the 1960s. Certainly, observations during the sea ice discharge were impossible. At the same time, conditions in the western areas of the Nordic Seas were not affected by extra freshwater export owing the limited dynamical connection to the discharge region.
4. In the 1950s and 1960s, a warm and salty regime prevailed all over the region, except for the Irminger Sea (OWSA), where a moderate low salinity anomaly was a dominant feature during the 1950s. Most likely, this is a consequence of the GSA gradual mixing with the underlying saltier water.
5. Strong atmospheric cooling of the late 1960s had a widespread influence on the vertical exchange over the entire Nordic Seas, intensifying both the light-to-dense water

transformation in the Atlantic domain and the intermediate/deep reaching convection in the Arctic part of the Nordic Seas Atlas (see the discussion in Introduction). An abrupt cooling event (marked with 'AC' in Fig. 5.3) of the salty Atlantic water caused a vast density increase (event is marked with '$D3^{+}$' in fig. 5.5) and sinking of the initially warm and salty surface water to the significant depths. The bottom panels in Fig. 5.3–5.5 show how deep this anomaly penetrated at different locations. The process continued for several years establishing a new hydrographic regime in the deep layers. For example, high salinity condition in 1000–2000 m layer at the OWSM location persisted until 1990 (Fig. 5.5).

6. The GSA's return in the second part of the 1970s designated an onset of a cold hydrographic regime with decreased salinity that lasted until the turn of the 20th century. A new pulse of cold and fresh water of the Arctic origin in the mid-1990s substantially reinforced that regime. Contrary to the GSA, this anomaly had subsurface intensification superseded the GSA magnitude at the surface (Blindheim et al., 2000). Strong freshening strengthened the upper ocean stratification and slowed transformation of the Atlantic water. Consequently, the layer underlying the Atlantic water became colder and fresher due to an increased contribution of the Arctic Intermediate water from the Arctic sector of the Nordic Seas Atlas domain. The changes of the deep water masses characteristics that are feeding the overflow from the Nordic Seas have further affected the properties of the North Atlantic Deep Water (Dickson et al., 1996).
7. The cold and low-salinity regime unexpectedly terminated in the late 1990s. Initiation of warm and salty conditions can be attributed to changes in Atlantic water inflow into the Nordic Seas (see the discussion in Introduction). An exceptionally strong warming of the upper layer led to unprecedented density decrease despite of a simultaneous salinity increase. Normally, the presence of high salinity in the upper ocean layer under atmospheric cooling at the surface is a precondition for more intense vertical mixing. However, the present-day situation is characterized by ocean warming from both above and below, as clearly seen in the OWSM or the Lofoten Basin TDDs. Furthermore, those two processes have already coupled in the Greenland Basin generating an unusual surface-to-bottom positive temperature anomaly (Fig. 5.3, bottom panel).

Although the time-depths diagrams capture much of the vertical variability, to obtain a more complete and detailed understanding of the ocean climate variability in the Nordic Seas, one needs to analyze horizontal fields as presented in the following Section.

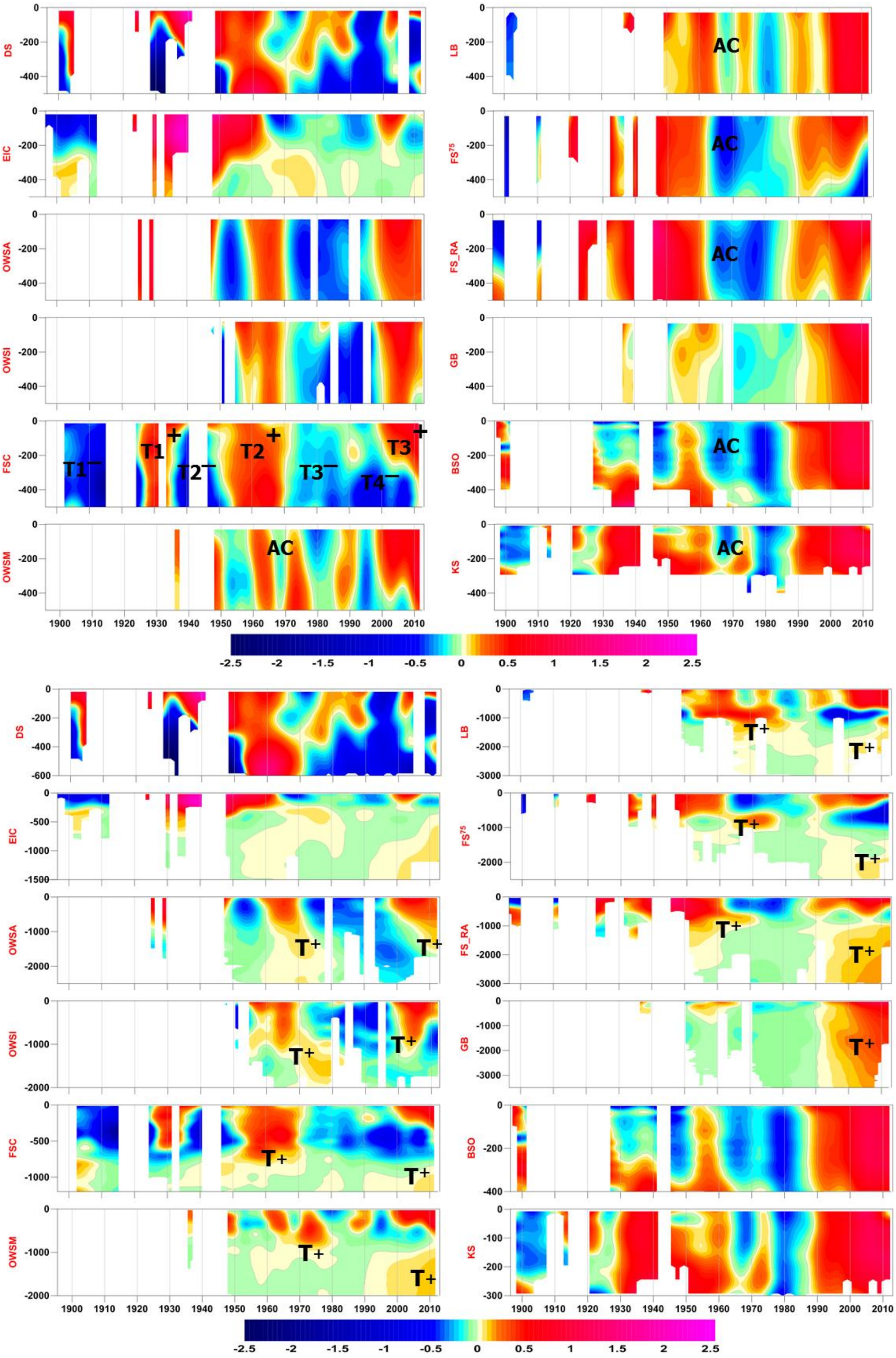

Figure 5.3 Time-depth diagrams of temperature anomalies (°C) in the 0–500 m layer (upper panel) and from the surface to the last interpolated depth level (bottom panel). Selected positive and negative temperature anomalies are marked by 'T', while 'AC' stands for abrupt cooling of the late 1960s.

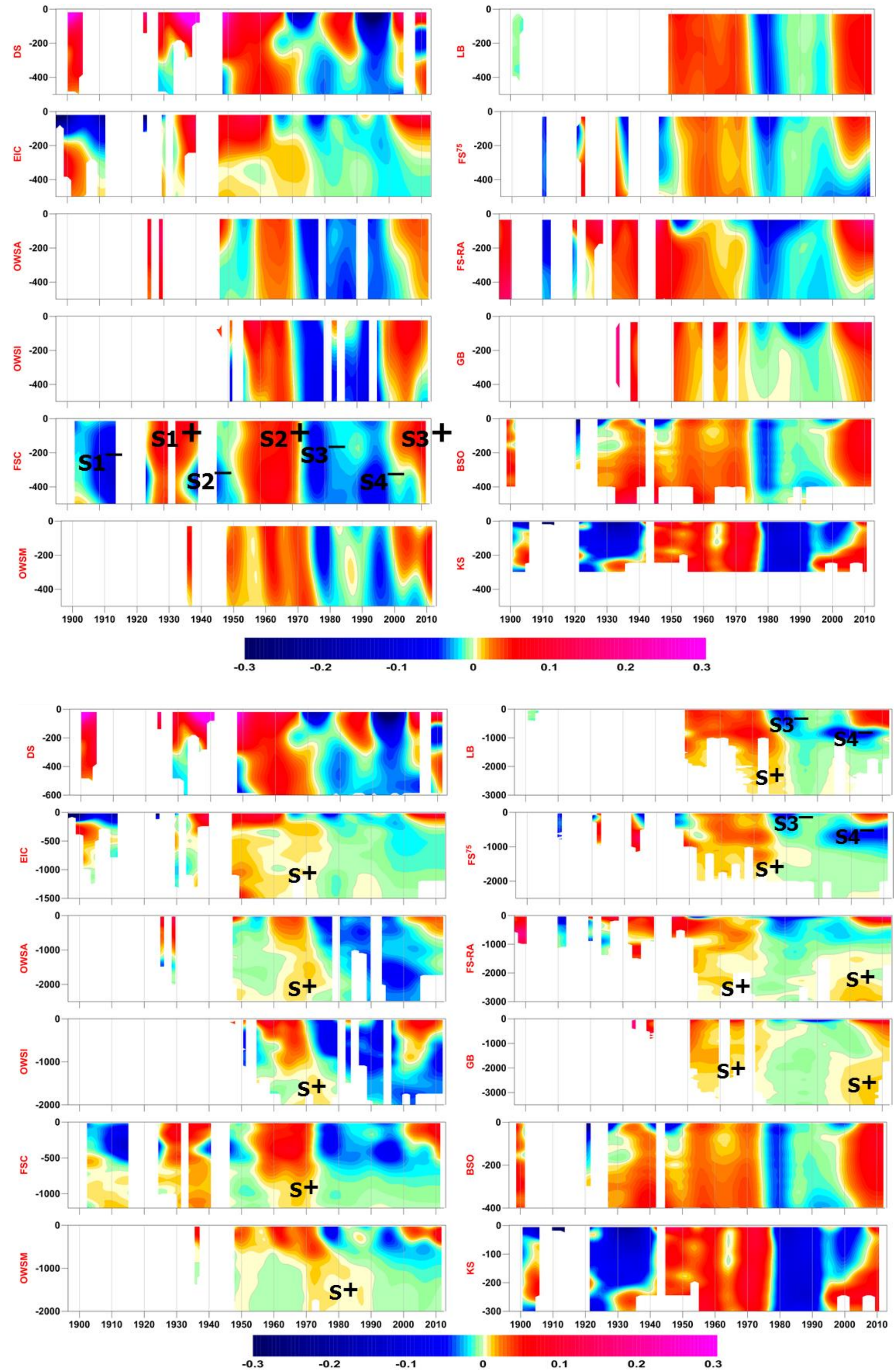

Figure 5.4 Time-depth diagrams of salinity anomalies in the 0–500 m layer (upper panel) and from the surface to the last interpolated depth level (bottom panel). Selected positive and negative salinity anomalies are marked by 'S'.

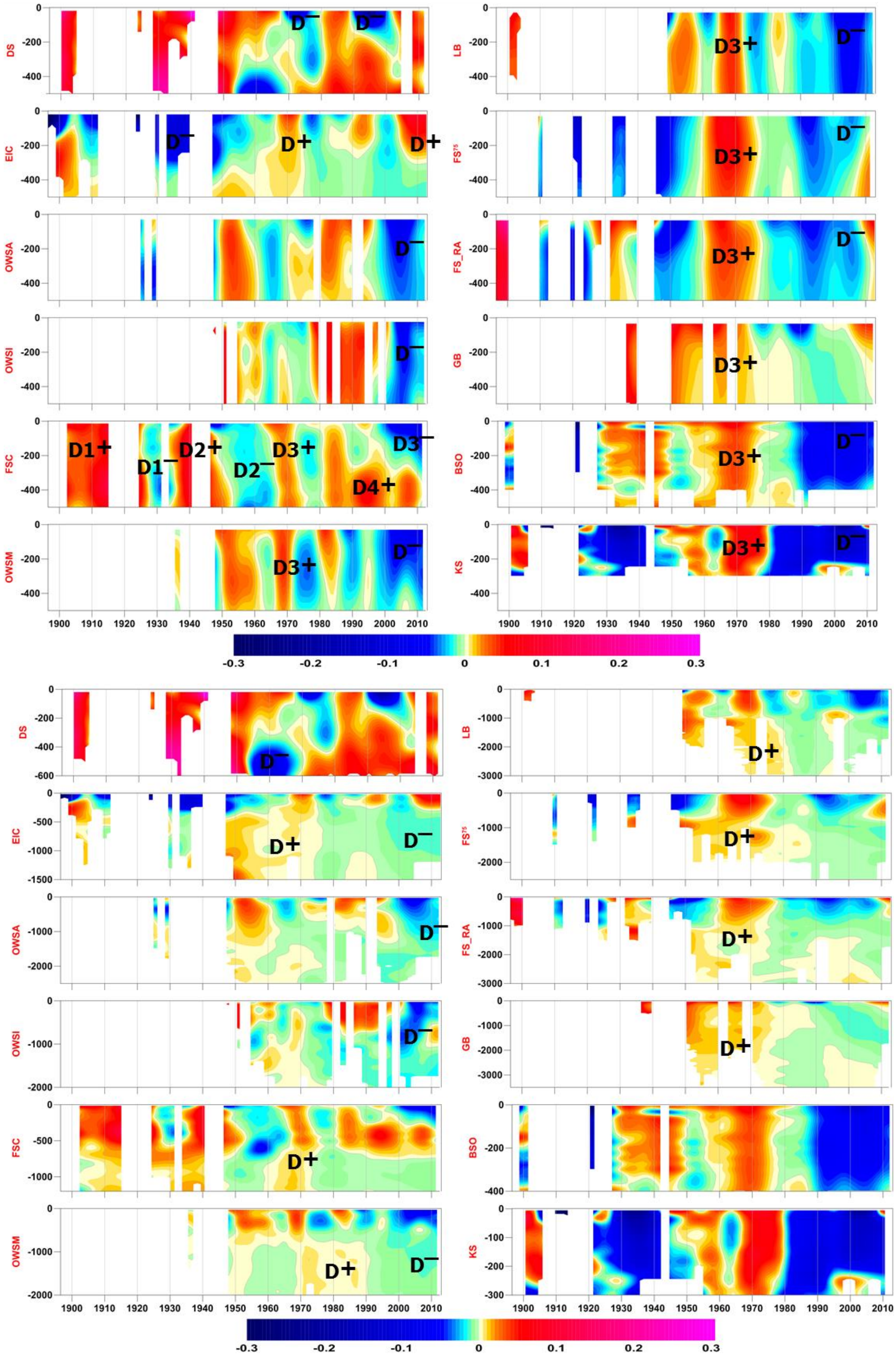

Figure 5.5 Time-depth diagrams of density (kg/m^3) anomalies in the 0–500 m layer (upper panel) and from the surface to the last interpolated depth level (bottom panel). Selected positive and negative density anomalies are marked by 'D'.

6. CLIMATOLOGICAL GRIDDED FIELDS

The Atlas provides seven types of gridded fields listed in Table 1 (see the content Section). The fields are in digital (as NetCDF files) and graphical representations (the monthly fields are only in digital format). The technology of computing gridded fields was described above (Sections 2, 3, and 4); here we provide some examples of fields and their application for studying water mass structure and variability.

6.1 Interpolation error and standard error of the mean

Each interpolated value estimated by DIVA is supplied with its interpolation error. This error is different from the error of climatological fields computed by averaging of the individually analyzed monthly fields (variant B), with provided standard error of the mean. Correct accounting for the errors is critical for the fields' evaluation. The major concern is that the errors should not exceed the magnitude of variability we are trying to estimate.

DIVA provides two different errors – relative (rated from 0 to 1) and absolute (expressed in physical units). Their magnitudes rely on the number and location of samples within a correlation radius of the interpolation node (Section 3). To define how the errors have to be treated and what threshold values have to be assigned, a series of experiments with gridded fields were conducted. We have studied the error dependence on variable, depth level and annual cycle (see also Section 3).

An example of temperature distribution with corresponding errors is shown in Fig. 6.1. It is evident that both error distributions match nicely together and the problem is how to determine the threshold value, which divides the field into reliable and non-reliable parts. However, the experiments have shown that the absolute error is not universal even for the same variable; it can vary with depth and annual cycle, and a constant threshold cannot be defined. This makes the utilization of the absolute error in routine calculations unpractical. Therefore, the relative error was chosen as the major criterion for the quality control of estimated values. A rather subjective assessment was applied to define the threshold value, based on joint consideration of the relative error and the observations location. Therefore, the threshold value of the relative error was set equal to 0.25. It allows keeping all estimations quite close to the data (Fig. 6.1 bottom panel) restricting extrapolation, which is always a dangerous procedure especially close to the data edges and in gradient zones. The value was further used in all kinds of the gridded fields processing (averaging, computing of anomalies etc.).

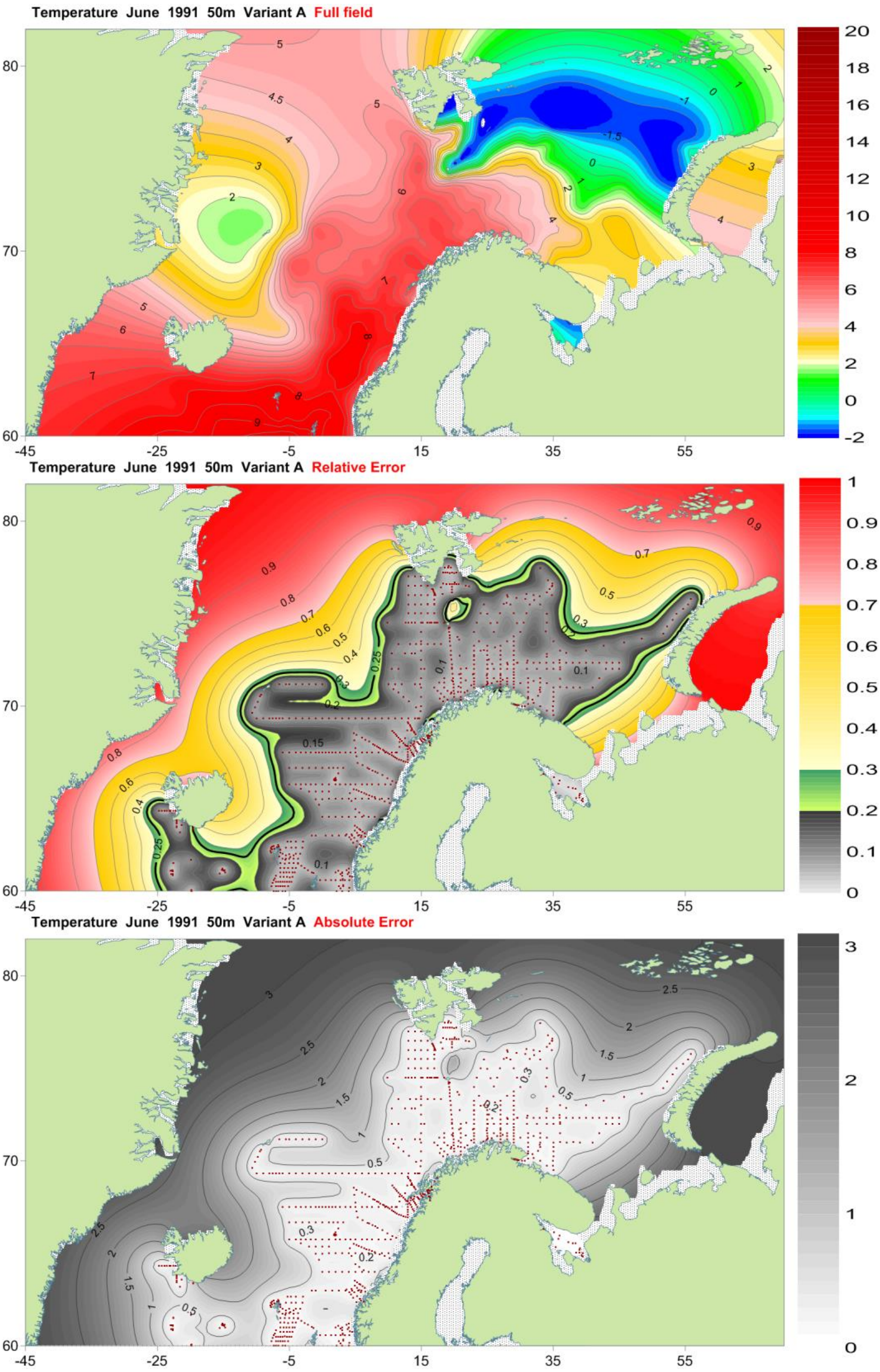

Figure 6.1 Temperature (top), relative error (middle) and absolute error (bottom) of interpolation at 50 m in June 1991. Areas shallower than 50 m are masked. Sample locations shown as red dots.

Figure 6.2 illustrates the field’s area reduction after applying the relative error thresholds from 0.5 to 0.2. Setting the relative error threshold equal to 0.5 cuts off all the grid nodes with the absolute error exciding ~1 °C. A threshold value equal to 0.2 designates an area, which is spatialy close to the measurements location and reduce the absolute error. The relative threshold equal to 0.3 remains to be close to the data but allows a slight extrapolation outside the area covered by the observations. Since our goal was to compute the climatological fields with potential for estimating of temporal variability, for further processing we have selected the relative error threshold value equal to 0.25 (highlighted in Fig. 6.1, middle panel) which keeps estimations sufficiently close to the data.

Despite the fact that the relative error was used to truncate the gridded fields, the absolute error is utilized for the fields’ quality representation (in turn truncated by the relative error equal to 0.25) and shown on all maps included into the Atlas in physical units.

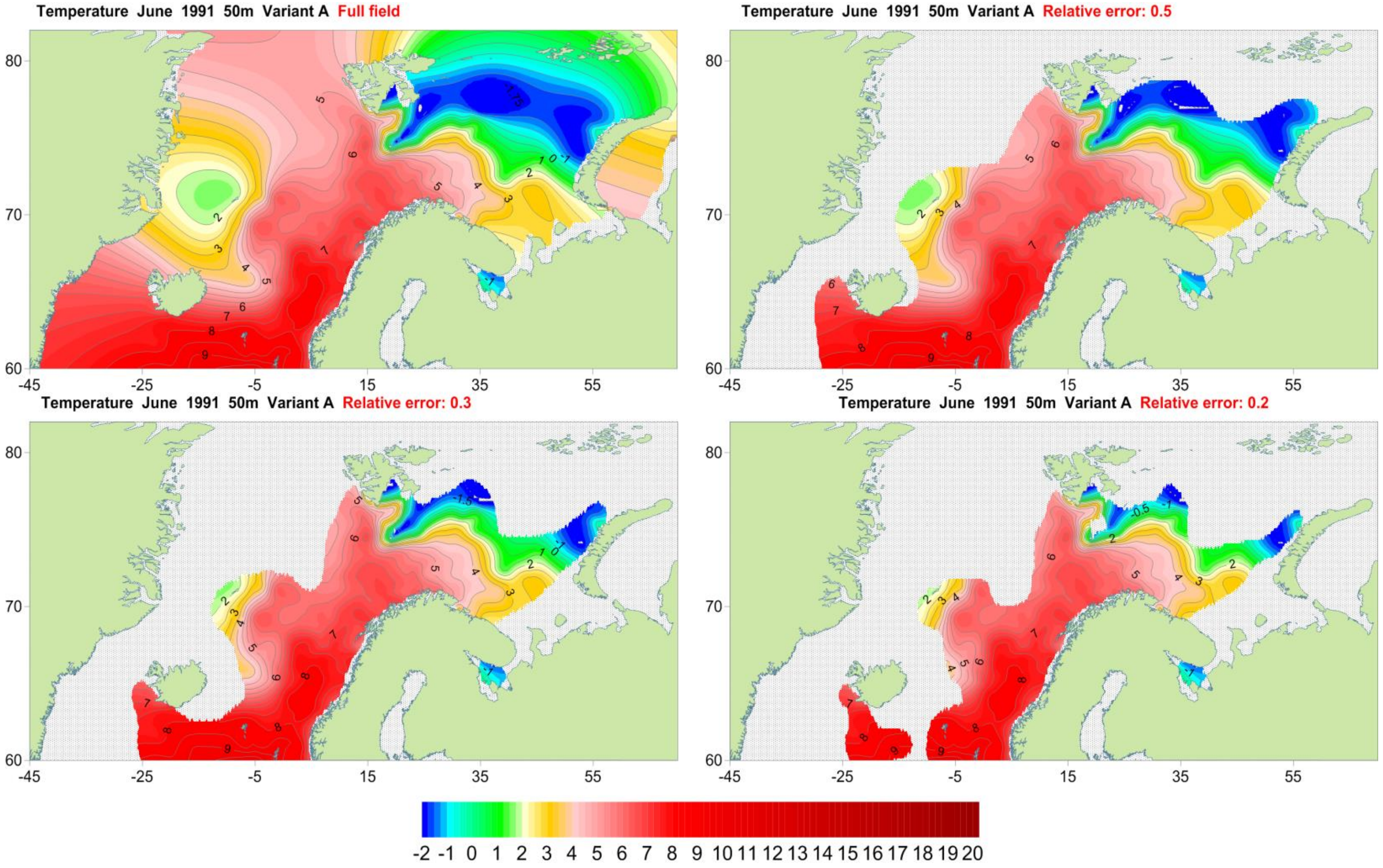

Figure 6.2 Temperature distributions at 50 m in June 1991 (top, left map) truncated by the relative error thresholds equal to 0.5 (top, right), 0.3 (bottom, left) and 0.2 (bottom, right). Areas shallow 50 m are masked.

6.2 Monthly fields

Variability in the ocean is caused by multiple interacting physical processes with various temporal and spatial scales, ranging from diurnal variations to multi-decadal fluctuations. To resolve a pattern of variability with a specific scale, appropriate observations have to be used. Helland-Hansen and Nansen (1909) were the first who noted the complexity of the ocean's variability and the necessity of detailed and reliable *in situ* measurements to describe and understand the driving mechanisms of observed variability. Measurements at sea, however, are limited due to the vast volume of the ocean, substantial economic costs, and instruments' imperfection. A major concern while getting a snapshot of the ocean state is that the observations at oceanographic stations are non-uniform both in space and time. The spatial interpolation technique, which has been described in Section 3 at least partially solves the problem of the spatial data irregularity, but the temporal interpolation remains a challenge. A compromise between the amount of available data and the time-scale of the physical processes is needed for resolving time-space irregularity of the oceanographic observations. Monthly averaged fields (monthly fields) is one of the approaches to such a compromise – assuming observations within one calendar month are uniform enough to represent ocean state, regardless of their temporal inconsistency. There are other ways to reduce the effect of the data insufficiency, for example, by increasing the selection period (a centered month for instance when data actually represent a longer period) or using zonal means. We opted for using the monthly data integration as the best resolution for our climatological fields.

Examples of monthly temperature, salinity and density fields at 0, 50, 300 and 800 m in June 1976 are presented in Figures 6.3–6.5. This is one of the best data coverage patterns that can be found in our database, with 1,590 oceanographic stations taken within one month (Fig. 6.6). Sixteen research vessels from five countries contributed to the extensive survey of the area in June 1976 – 'Aisberg', 'Akhill', 'Ayaks', 'Professor Vise', 'Tunets', 'Vsevolod Berezkin', 'Fridtjof Nansen', 'Mikhail Somov', 'Nerei' (USSR), 'G.O.Sars', 'Polarfront II', 'Rommenstad', 'Johan Hjort' (Norway), 'Bjarni Saemundsen' (Iceland), 'Mara' (United Kingdom), 'Planet', 'Viktor Hansen' (Germany). Undoubtedly, collocated but not synchronous measurements introduce noise related to both deterministic (e.g. summer warming at the surface) and random processes (e.g. eddy propagation). Accompanied by the instrumental errors, which varied from vessel to vessel (and therefore is difficult to evaluate), it constitutes an uncertainty in the observations transferred to the gridded monthly field.

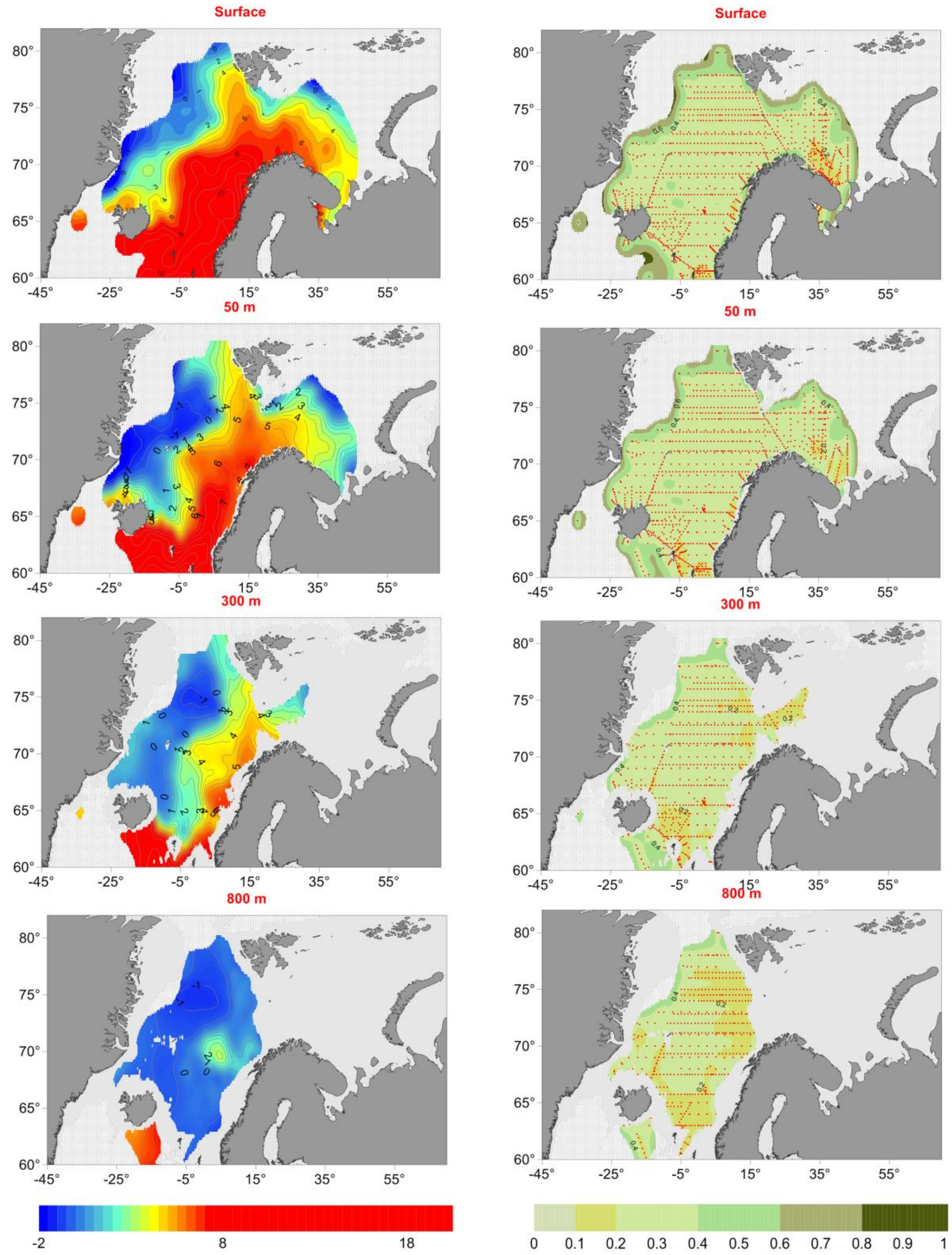

Figure 6.3 Monthly temperature (°C) fields at 0, 50, 300 and 800 m in June 1976 (left) and corresponding distributions of absolute error (right). Sample locations shown as red dots.

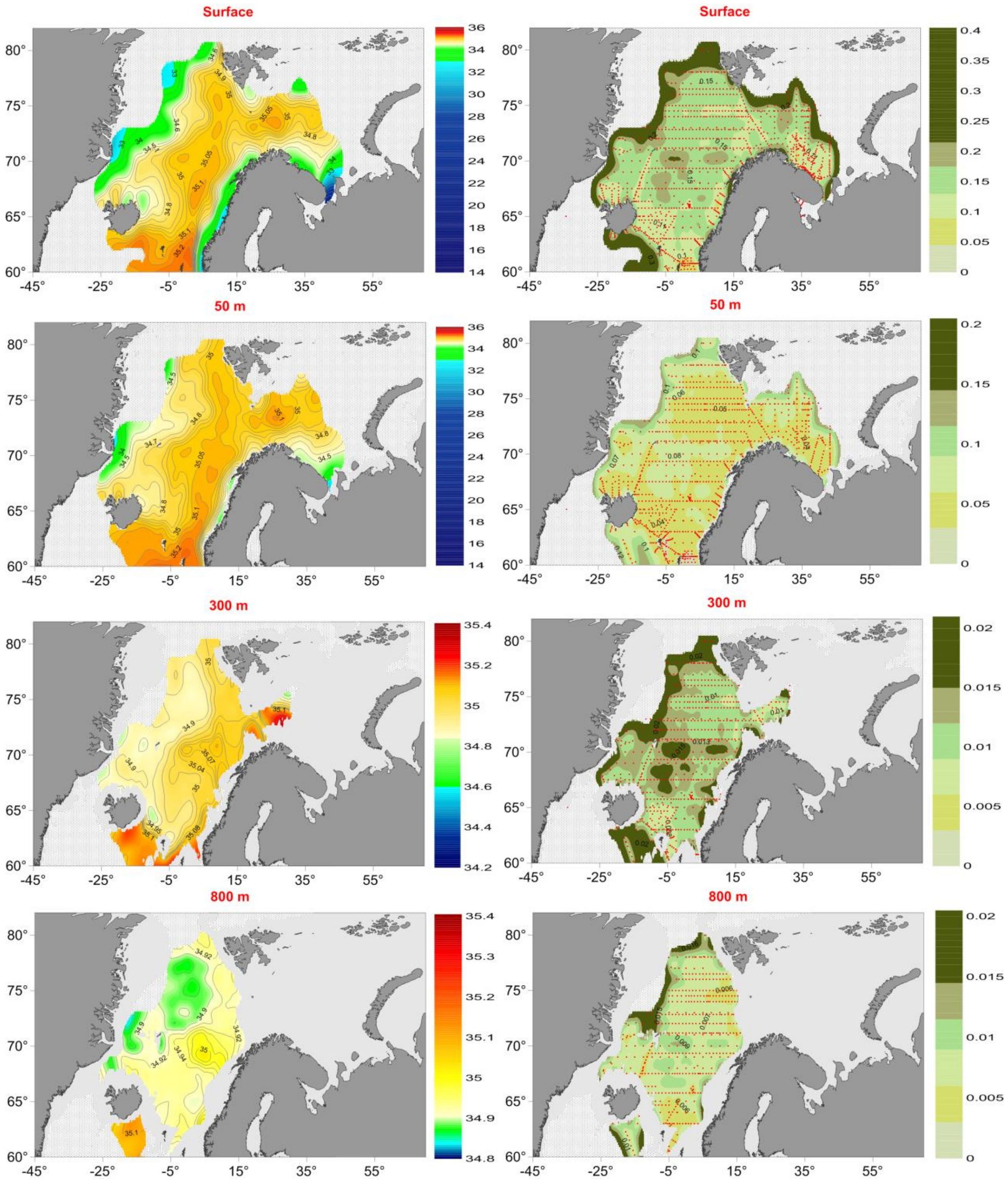

Figure 6.4 Monthly salinity fields at 0, 50, 300 and 800 m in June 1976 (left) and corresponding distributions of absolute error (right). Sample locations shown as red dots.

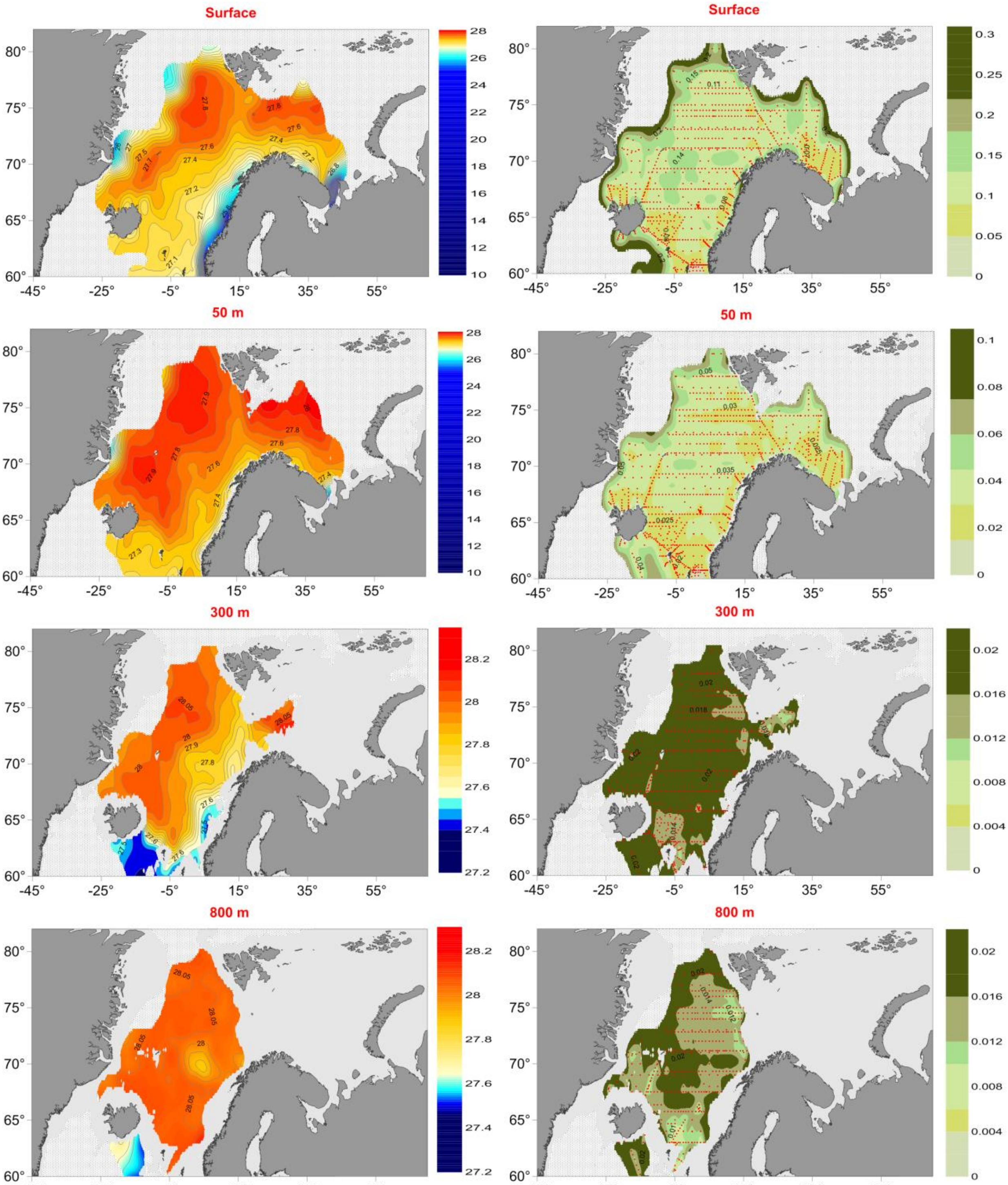

Figure 6.5 Monthly density (kg/m^3) fields at 0, 50, 300 and 800 m in June 1976 (left) and corresponding distributions of absolute error (right). Sample locations shown as red dots.

The comparison of sample locations and distribution of absolute errors (right panels in Fig. 6.3–6.5) reveals strong dependence of the errors on location. The magnitude of the error is minimal within densely sampled areas and reaches maxima at data boundaries. For temperature, the absolute error within the data-covered area is typically less than 0.5 °C, decreasing to less than 0.2 °C at the best-sampled locations. The magnitude of the absolute error decreases with depth due to the generally decreasing variability, regardless of the number of available samples.

The monthly fields preserve the major features of water masses at different depths quite well. As it will be shown further in the text, the mean reference monthly field has to be computed to quantify uniqueness of June 1976 relative to the mean conditions.

6.3 Yearly fields

The next step in generalization, beyond the monthly scale, is computing annual mean fields. Notably, a new uncertainty arises due to irregularity of data distribution within a year. There is a clear tendency of measurements being more abundant for the warm period and underrepresented for the cold period (Section 2). The maps of stations location for all months of the year 1976 (Fig. 6.6) illustrate such irregularity (maps for 1900–2012 period are available on the web). In 1976, there were almost no measurements in the northern North Atlantic. The best data coverage of the Nordic Seas is found in April, May and June, while the Barents Sea was better surveyed in August and September.

We employed two methods for computing the annual mean fields. The first method is based on the joint analysis of all 1976 data together (variant ‘A’). The second is a two-step procedure consisting of an analysis of data within each month of the year and then averaging of the generated monthly fields to obtain the annually mean fields (variant ‘B’). The derived fields of temperature, salinity and density for both variants and their differences are presented in Fig. 6.7–6.9. It is important to know which algorithm was used for averaging in variant ‘B’. Ideally, we have to average 12 monthly values in each node to obtain unbiased estimate of the annual mean. In reality, due to lack of data, the estimated area will shrink to a few locations where regular monitoring take place, which we have already explored using time-depth diagrams (Section 5). Therefore we relaxed the criterion in order to obtain better spatial coverage for the variant ‘B’. Different algorithms can be used – from at least one value at a node to their different combinations.

To reduce the bias of the annual mean value, we used a threshold that at least one value must exist in the warm and one in the cold periods before averaging. An alternative threshold was at least one value must exist in each season of the year. In the discussed one-year case (Fig. 6.6), we set the criterion that at least three monthly values exist in a node regardless of the season. In the Atlas, much longer periods are considered and stricter criterion of at least one estimated value in each three-month season was used.

In the 1976 example, it is evident that the variant ‘A’ provides a larger estimated area, while the variant ‘B’ yields less biased estimates. Nonetheless, in one-year cases, the averaging algorithm also produces estimates biased toward the months with better data coverage (April – June for the Nordic Seas, June – September for the Barents Sea). As can be seen in the ‘difference maps’ (Fig. 6.7–6.9, low panels), the offsets depend on sample locations. Within the areas with a relatively good data coverage, the offsets do not exceed ~0.3 °C for temperature, ~0.2 for salinity and ~0.05 kg/m^3 for density. However, at some locations closer to the boundaries and in the zones of sharp gradients, the differences can be significant – more than 1 °C for temperature, 0.3 for salinity and 0.1 for density. In all such cases (in the Denmark Strait, close to the Norwegian coast, the East Icelandic Current and some other areas) large differences are caused by uneven data distributions within gradient zones. This highlights the importance of the error field’s analysis prior making inference from the gridded fields.

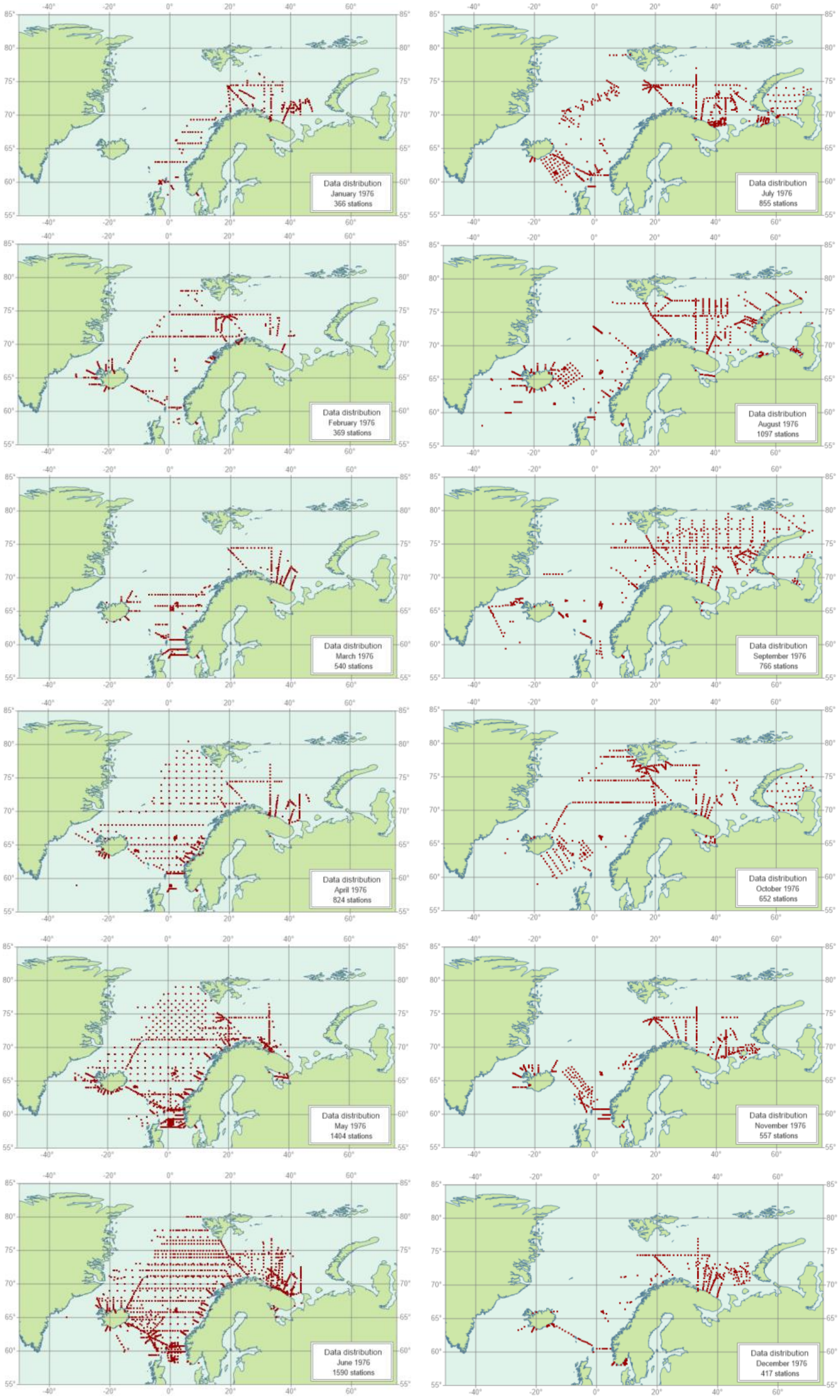

Figure 6.6 Oceanographic station positions (red dots) by month in 1976.

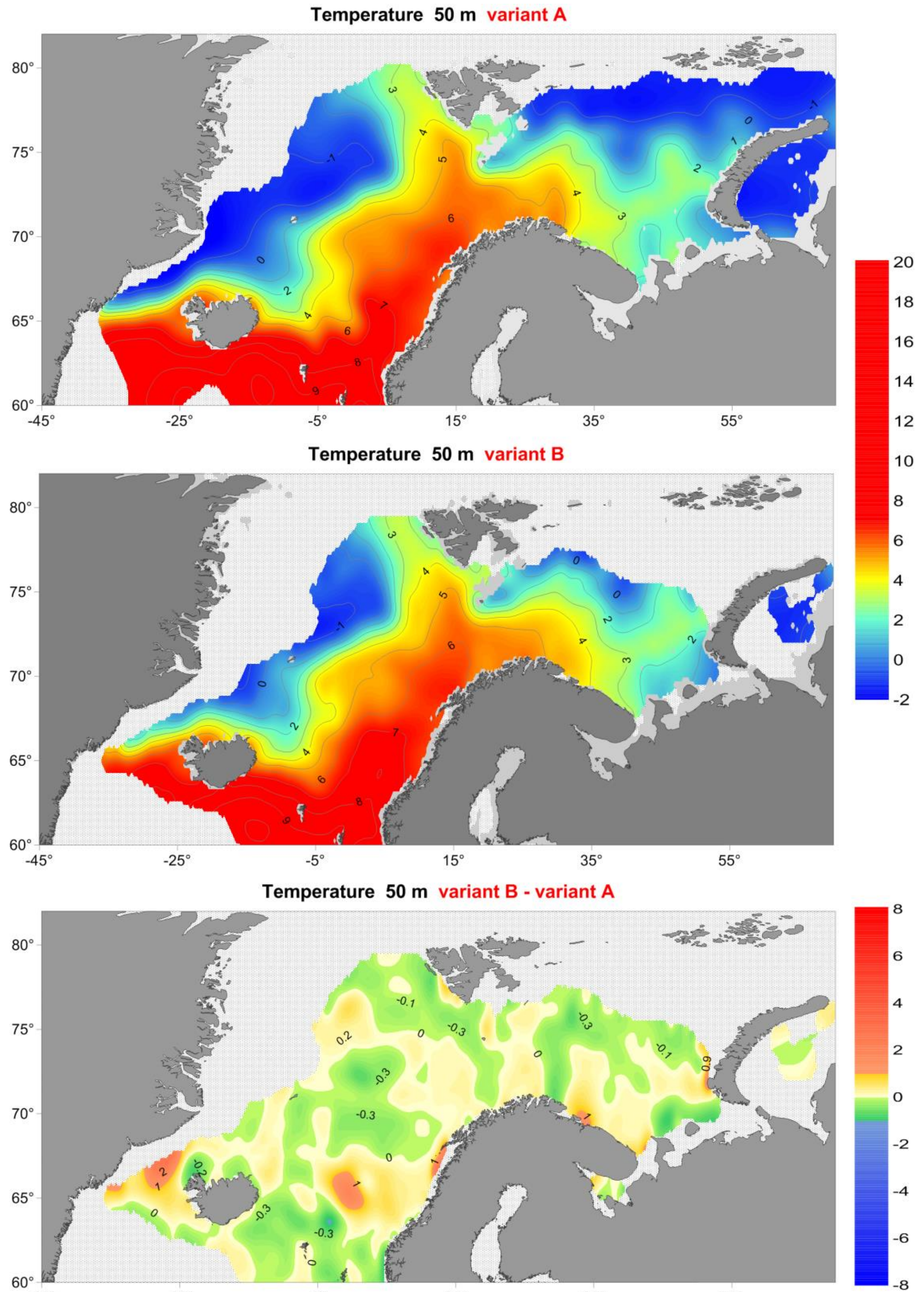

Figure 6.7 Annual mean temperature (°C) distributions in 1976 computed by the variant ‘A’ (upper panel) and the variant ‘B’ (middle). The bottom panel shows their difference.

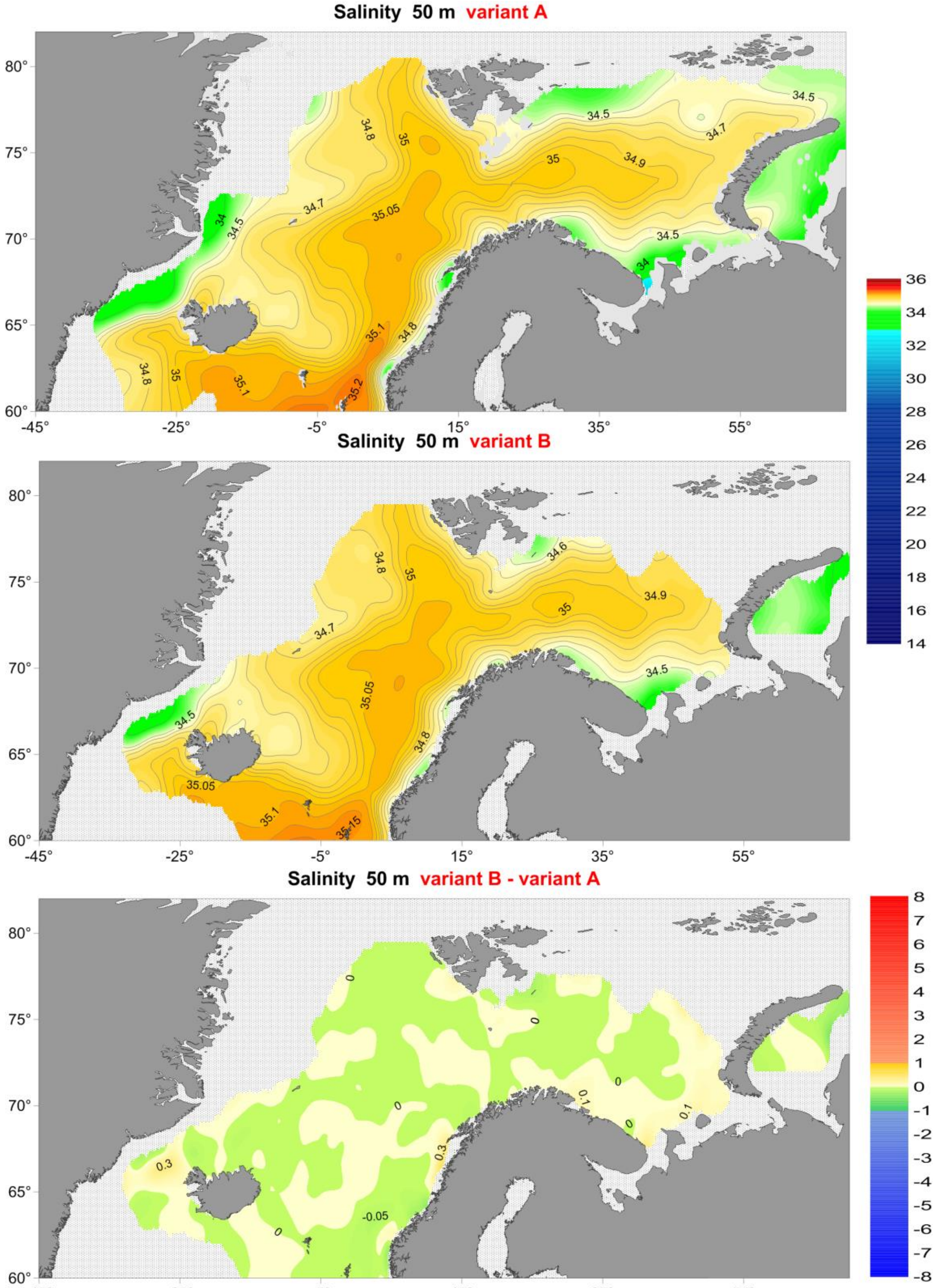
Salinity 50 m variant A

Salinity 50 m variant B

Salinity 50 m variant B - variant A

Figure 6.8 Annual mean salinity distributions in 1976 computed by the variant 'A' (upper panel) and the variant 'B' (middle). The bottom panel shows their difference.

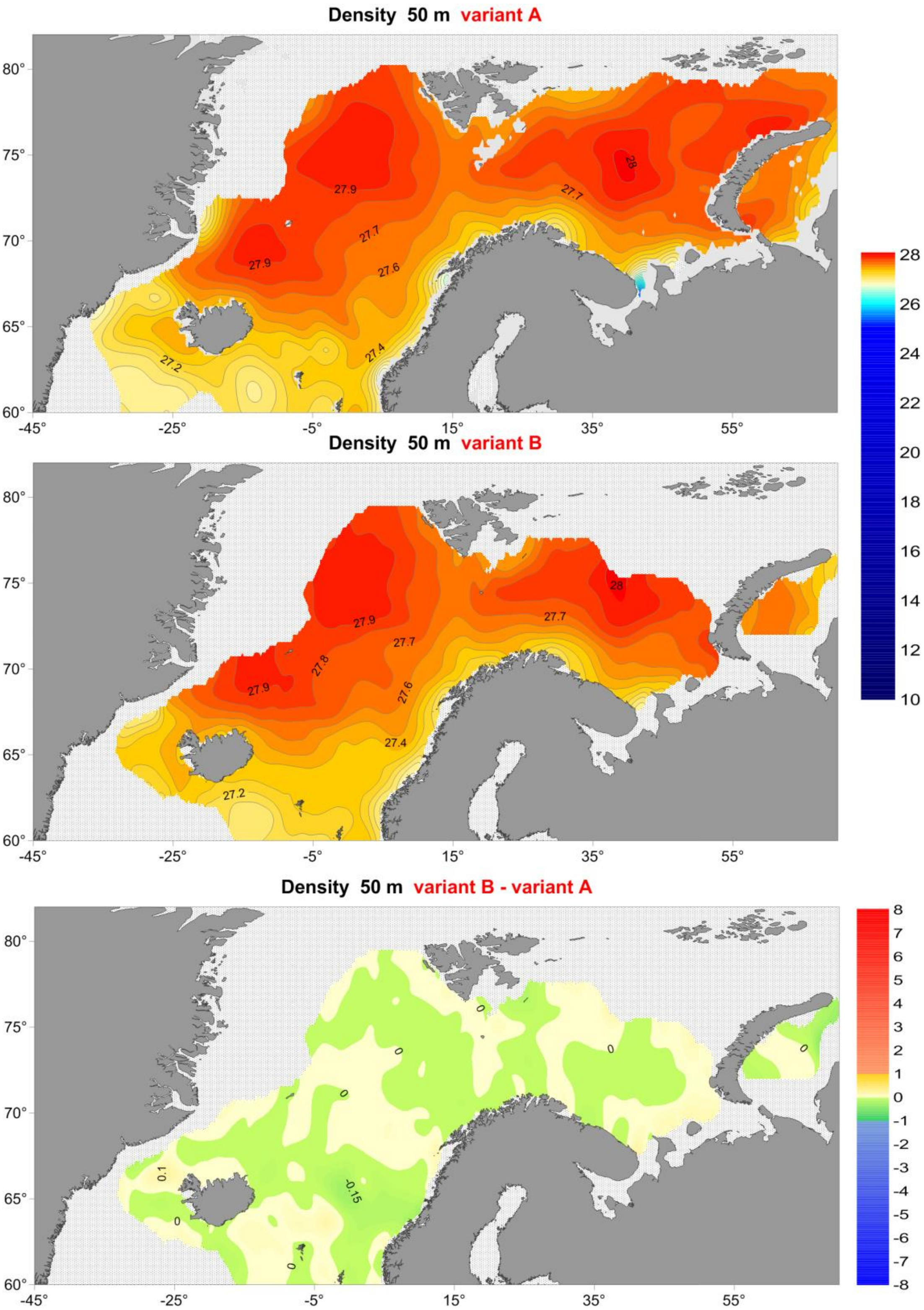

Figure 6.9 Annual mean density (kg/m^3) distributions in 1976 computed by the variant ‘A’ (upper panel) and the variant ‘B’ (middle). The bottom panel shows their difference.

6.4 Climatological fields

The Atlas contains climatological fields for six anomalous periods, eleven decades and two reference periods (see Atlas content). The long-term means for the reference periods of the years 1900–2012 and 1950–2000 were computed. The second period excludes data prior 1950, with generally lower data quality, as well as a warm period after 2000. Decadal fields were computed to compare them with decadal averages in similar products (decadal averaging is commonly used in oceanography and climatology). The anomalous periods were selected from the time-depth diagrams and were divided on “abnormal regimes” and “abnormal events.” As a rule, a regime is longer, and can include several unidirectional events (defined as a several-year variable deviation from average state).

Distributions of temperature, salinity, density at 0, 50, 300, 800 m for 1900–2012 and 1950–2000 reference periods are presented in Fig. 6.10–6.12 and 6.13–6.15, respectively. They illustrate the structure of water masses within different layers: the upper layer with horizontal advection, intermediate layer with strong horizontal gradients (or frontal zones between waters of Atlantic and Arctic origin), and deep-water strata over deep basins. At the upper layer, the two-branch advection of the Atlantic water to the Arctic through the Fram Strait and the Barents Sea is clearly seen, as well as the magnitude of the water properties transformation along these routes. At 300 m, the area of the Atlantic water in the eastern part of the Nordic Seas shrinks considerably (in comparison with the overlying layers) and is replaced by colder, fresher and denser water masses of Arctic origin. At 800 m, the Atlantic water with temperature of more than 2 °C concentrates in the Lofoten Basin, while the most dense and coldest waters, yet with somewhat reduced salinity, occupy the Greenland Basin.

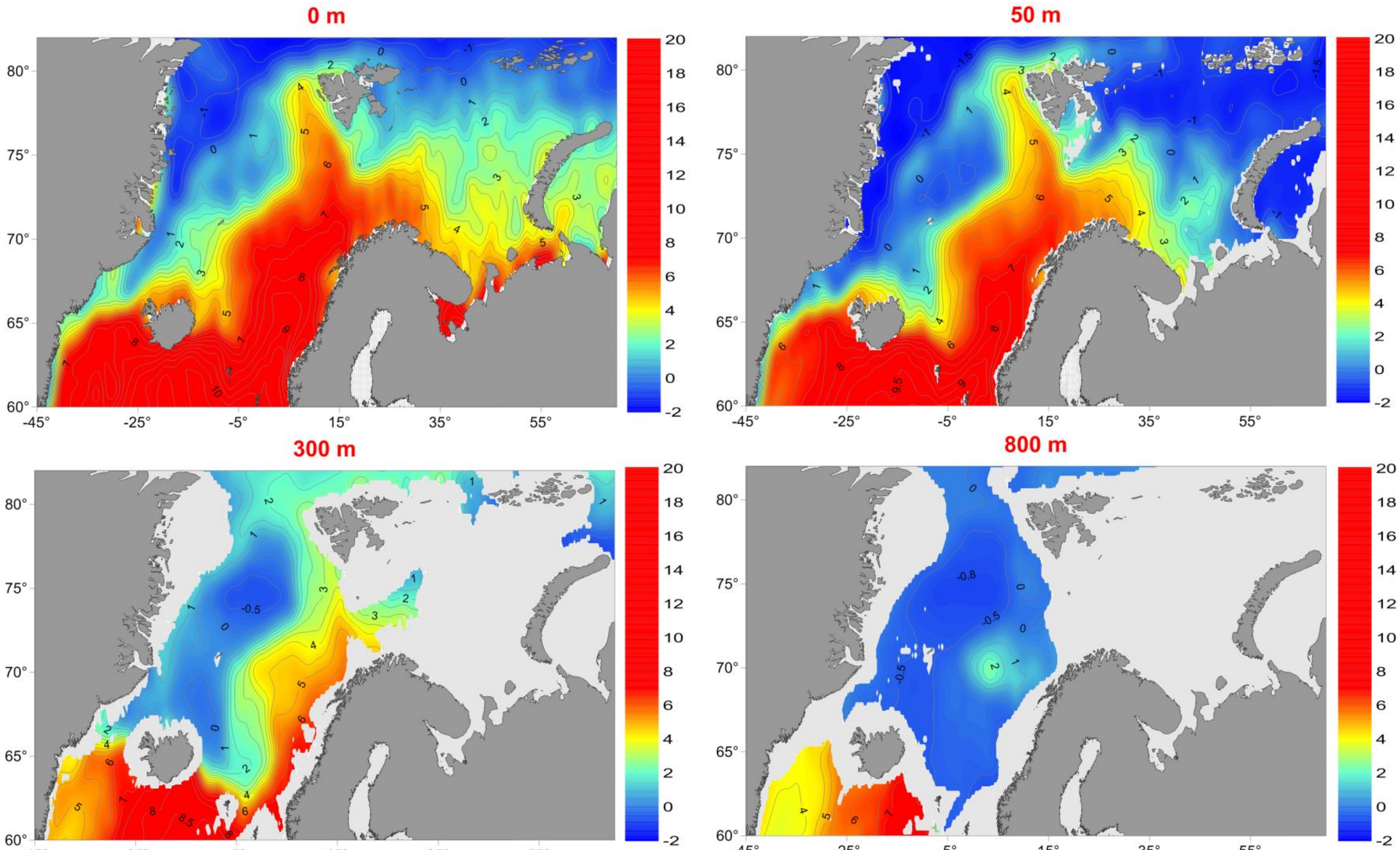

Figure 6.10 Mean temperature (°C) distributions at 0, 50, 300 and 800 m for the 1900–2012 period computed in the variant ‘A’.

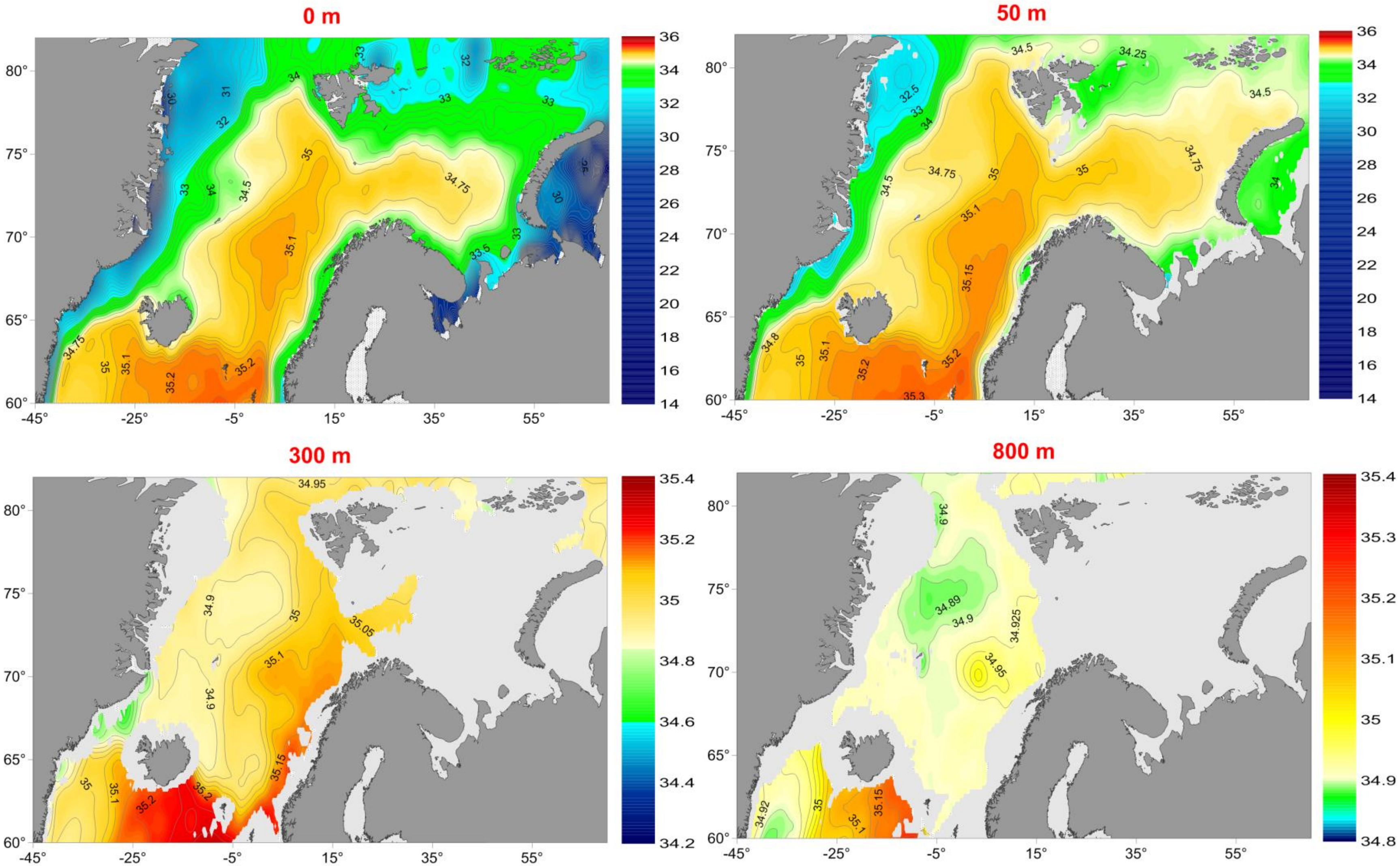

Figure 6.11 Mean salinity distributions at 0, 50, 300 and 800 m for the 1900–2012 period computed in the variant ‘A’.

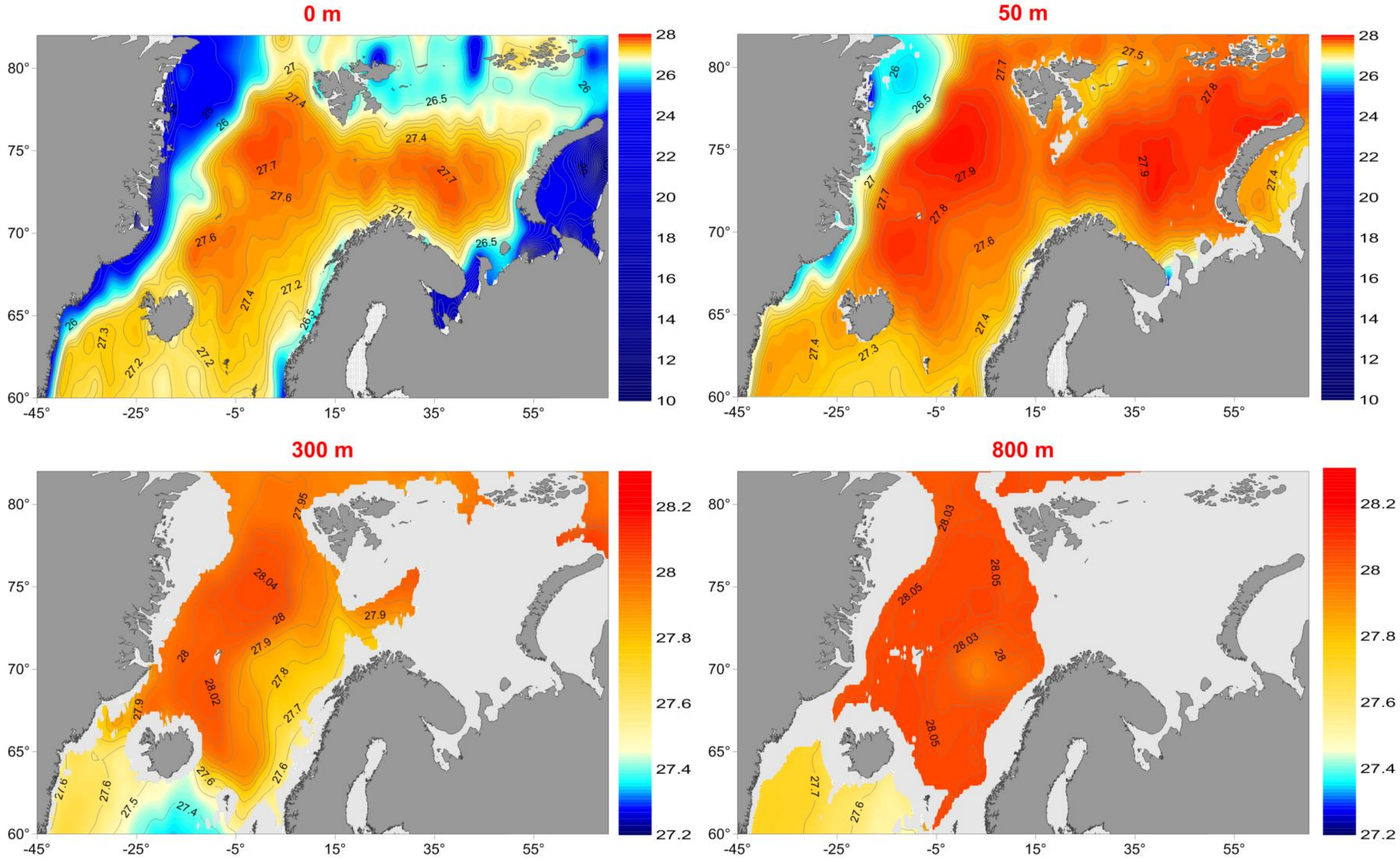

Figure 6.12 Mean density (kg/m^3) distributions at 0, 50, 300 and 800 m for the 1900–2012 period computed in the variant 'A'.

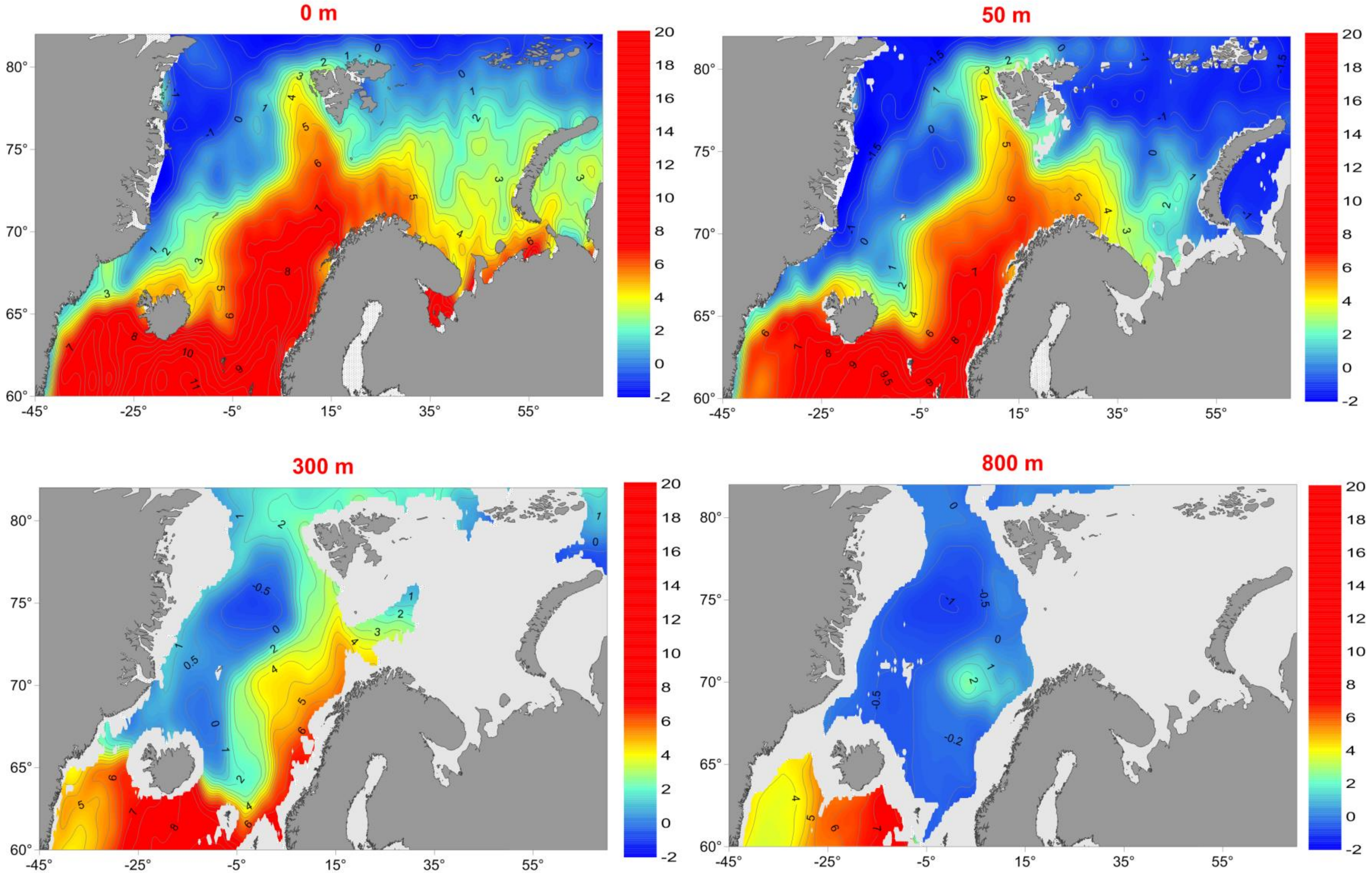

Figure 6.13 Mean temperature (°C) distributions at 0, 50, 300 and 800 m for the 1950–2000 period computed in the variant ‘A’.

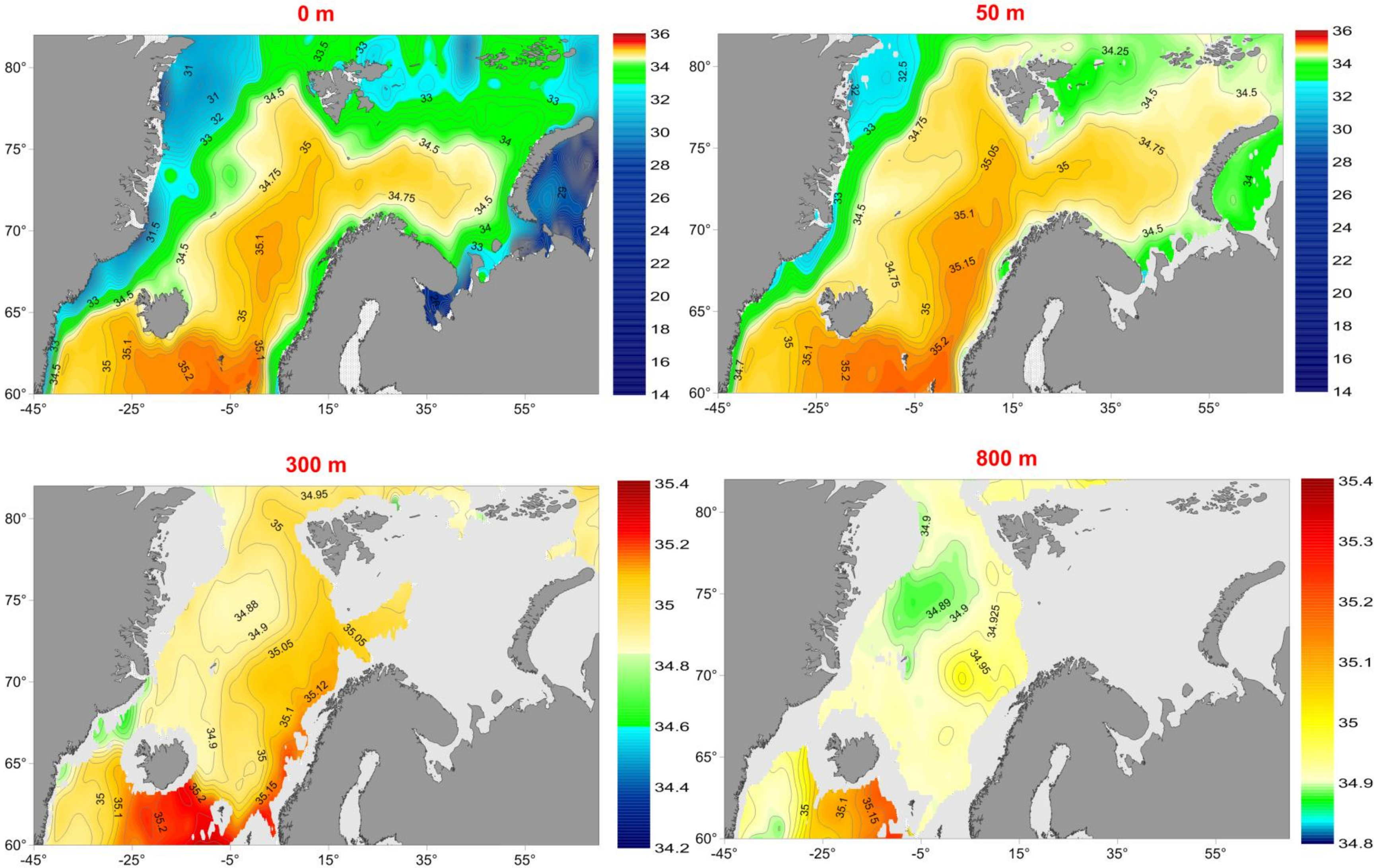

Figure 6.14 Mean salinity distributions at 0, 50, 300 and 800 m for the 1950–2000 period computed in the variant ‘A’.

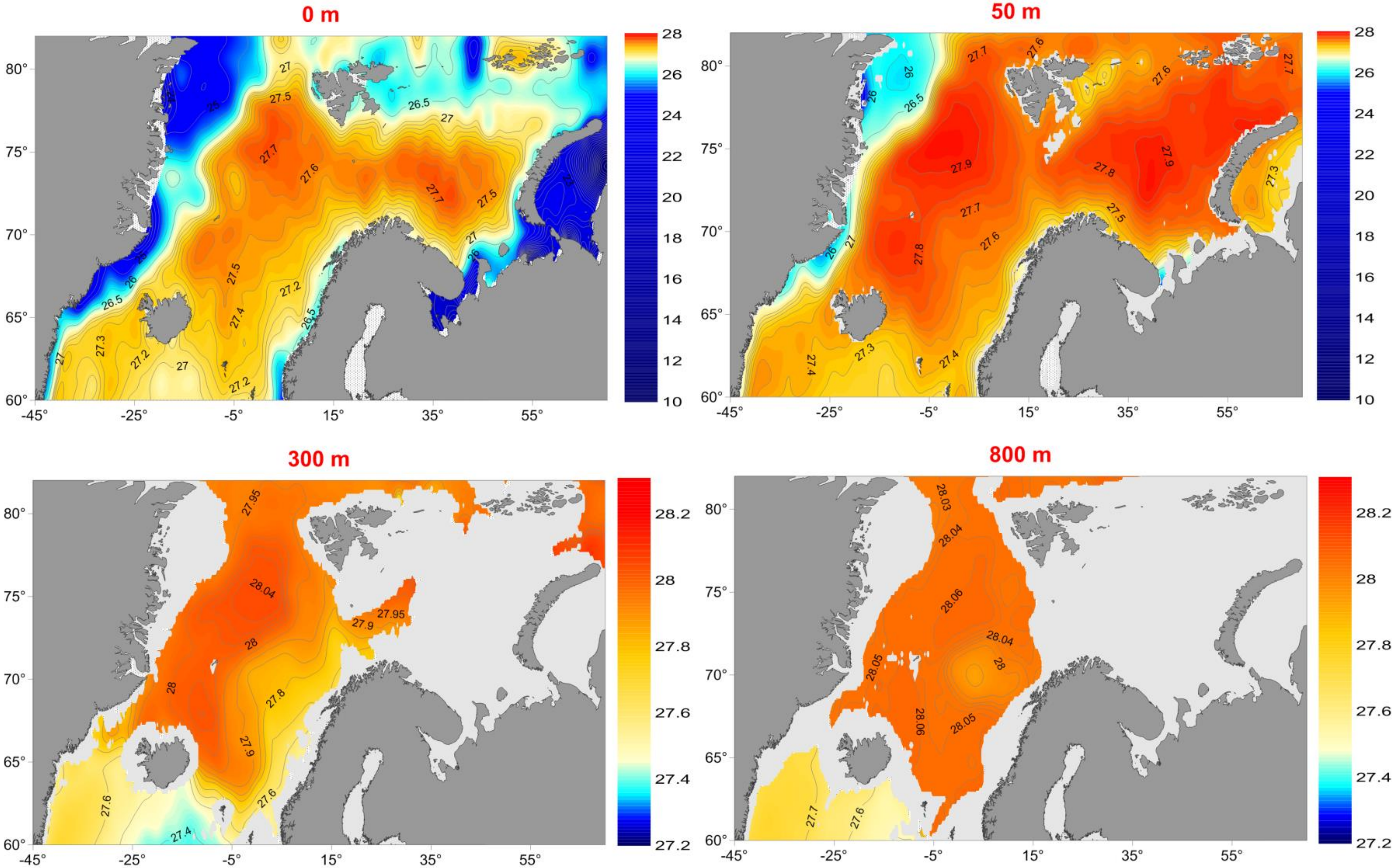

Figure 6.15 Mean density (kg/m^3) distributions at 0, 50, 300 and 800 m for the 1950–2000 period computed in the variant ‘A’.

6.5 Fields comparison

A collection of gridded fields for the various periods, included in the Atlas, allows estimating of irregularity of ocean state on different time scales. A special program module embedded in the 'OceanShell' allows computing and visualizing of anomalies (or deviations) between any two gridded fields (stored in the NetCDF format).

We will first evaluate the difference between fields for two long-term periods used as references for anomalies (1900–2012 and 1950–2000). For this purpose, anomalies of temperature, salinity and density at 0, 50, 300 and 800 m were computed by subtraction of 1950–2000 values from 1900–2012 values (Fig. 6.16–6.18). Positive anomalies at 0, 50 and 300 m reflect generally warmer and saltier conditions for the 1900–2012 period. It can be explained by the fact that the longer period includes two warmer and saltier periods of the 1930s and the 2000s. Contrary to temperature and salinity, density is characterized by negative values due to predominantly higher temperatures (Fig 6.18). At 800 m, a boundary between negative and positive temperature deviations runs strait across the middle of the Nordic Seas. The positive values in the western part can be explained by reduced ventilation in the Arctic domain, while negative values in the eastern part are likely due to reduced Atlantic water transformation caused by strengthening of the upper layer stratification. Deviations between the climatological fields for the most part of the domain do not exceed ~0.5 °C for temperature and ~0.1 for salinity, but at the boundaries they can reach considerably higher values mainly because of insufficient data coverage in the zones of sharp gradients.

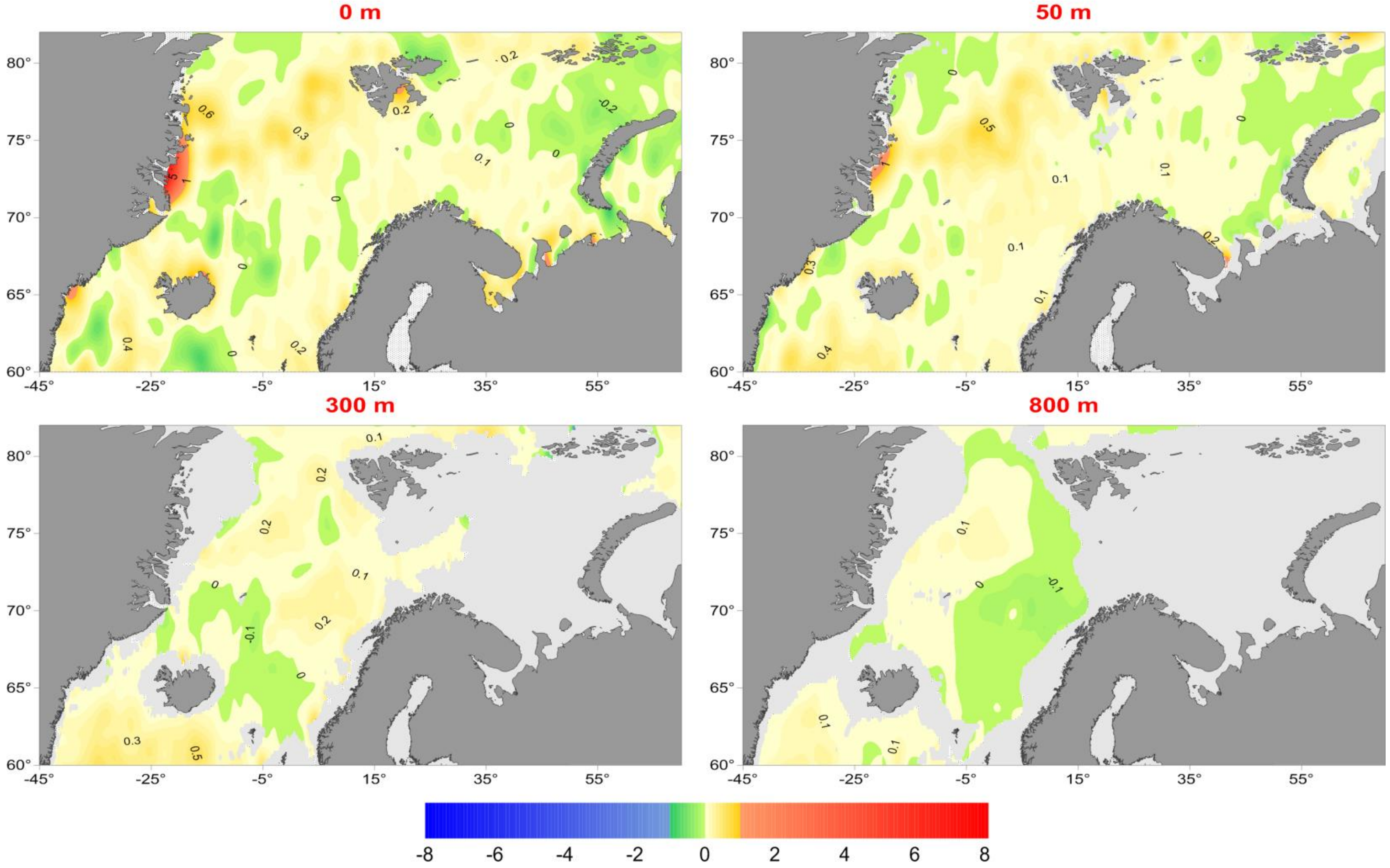

Figure 6.16 Temperature difference (°C) between 1900–2012 and 1950–2000 reference periods computed by the variant ‘A’.

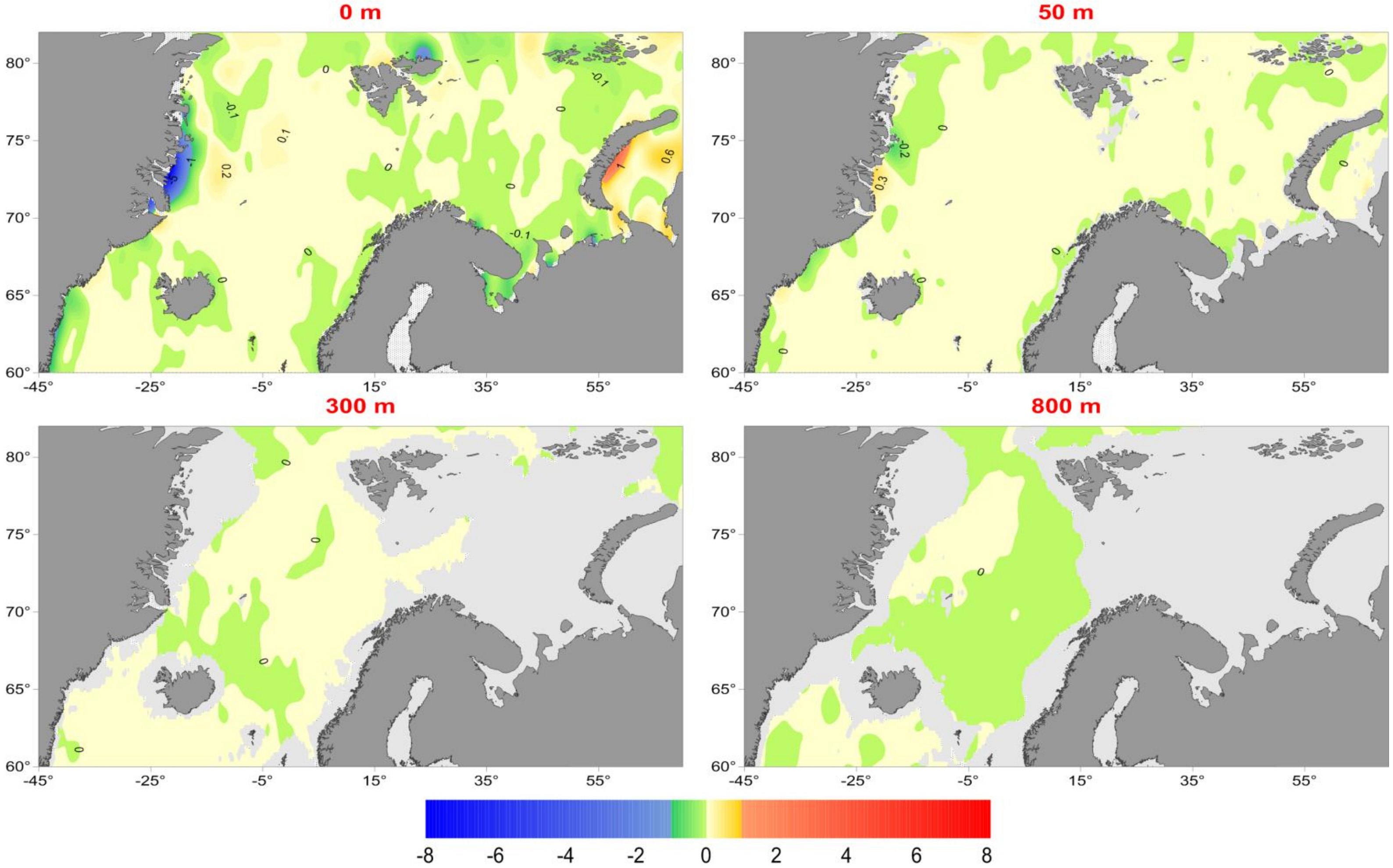

Figure 6.17 Salinity difference between 1900–2012 and 1950–2000 reference periods computed by the variant ‘A’.

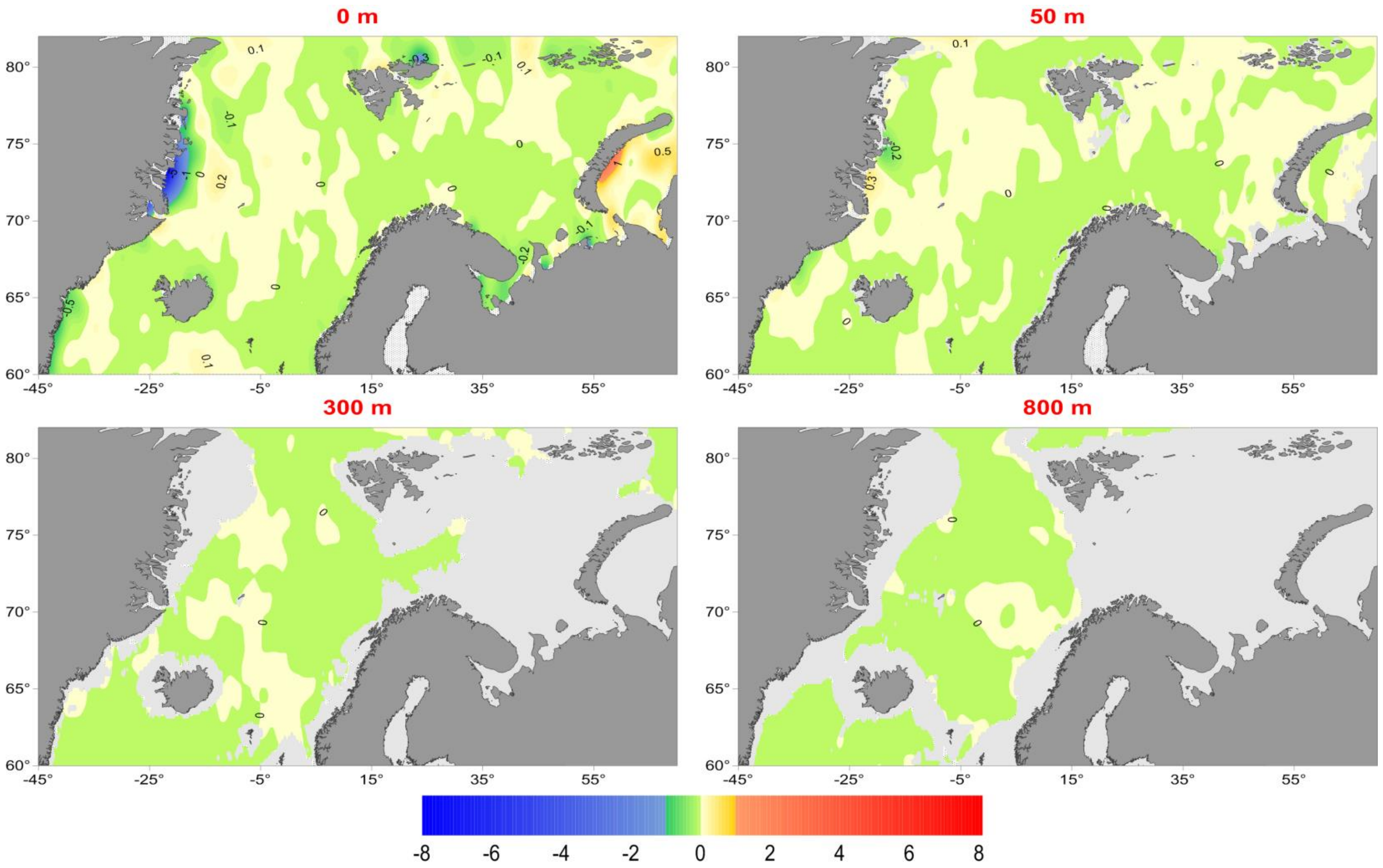

Figure 6.18 Density difference (kg/m^3) between 1900–2012 and 1950–2000 reference periods computed by the variant ‘A’.

Now we can estimate the singularity of oceanographic conditions in 1976. Salinity anomalies at 50 m computed as a difference between the annual mean values for 1976 and the two reference periods exposing the return of ‘The Great Salinity Anomaly’ to the Nordic Seas (Fig. 6.19). In both cases, the magnitude of the salinity anomaly crossing the Iceland-Faroe Ridge, exceeds 0.1. However, it is worth mentioning that the salinity background had already been reduced over large areas in the eastern part of the Nordic Seas. A more detailed analysis of the monthly fields in 1975 and 1976 (not shown) confirmed that the upper-layer salinity started declining before the GSA returned to the Norwegian Sea.

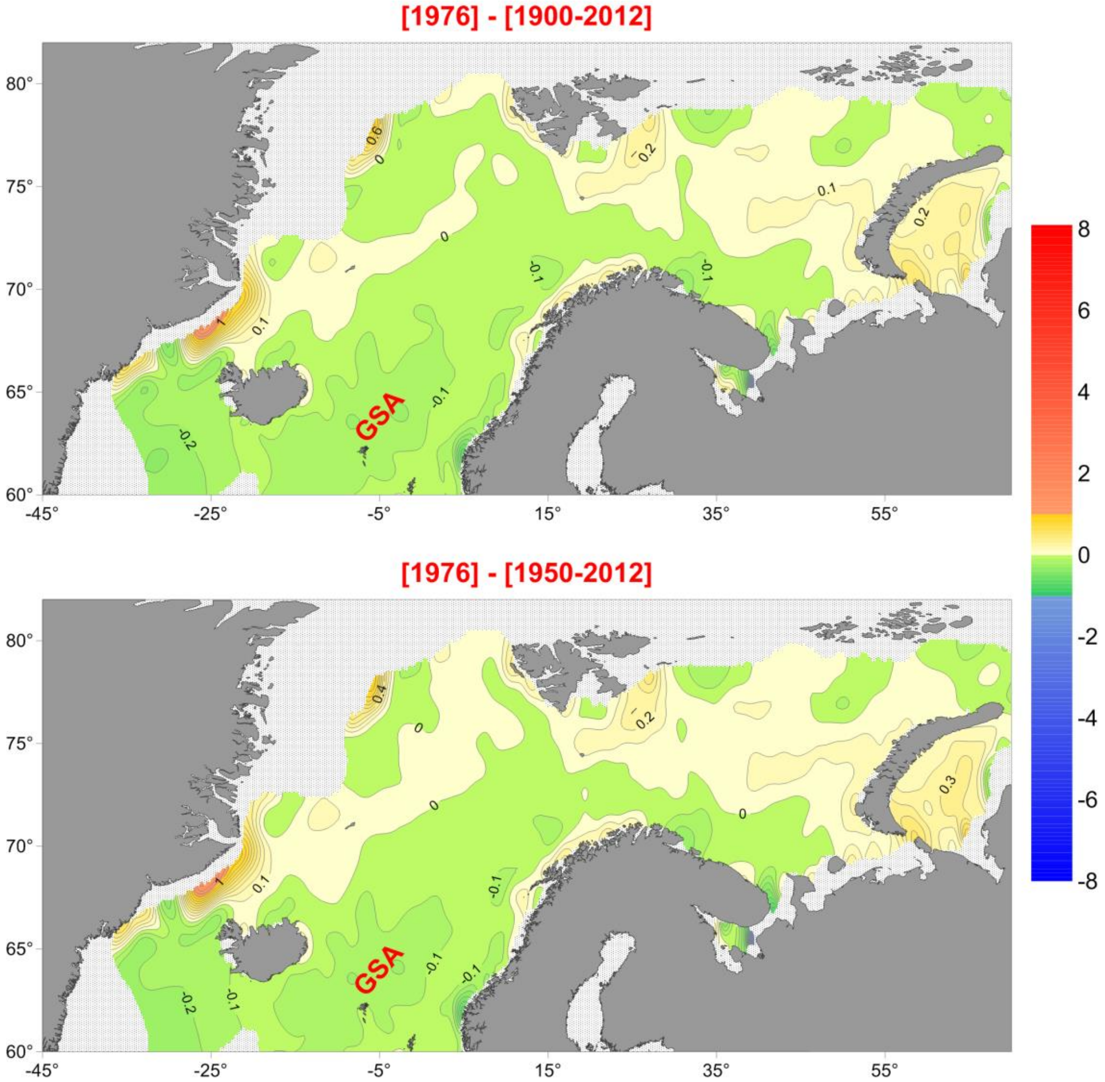

Figure 6.19 Salinity anomalies at 50 m computed as difference between the year mean salinity in 1976 and mean salinity for the two reference periods 1900–2012 (top) and 1950–2012 (bottom). The negative anomaly associated with the ‘Great Salinity Anomaly’ is labeled as GSA.

To evaluate the spatial pattern of seasonal transformations, the 1900–2012 yearly reference field was subtracted from the computed for the same period mean monthly fields. The example of temperature at 50 m is presented in Fig. 6.20. The anomalies indicate that the cold season continues from January to May, warm conditions dominate from July to November, while June and December are the transitional. The time when the largest area was occupied by water with temperature anomaly colder than –1 °C coincides with March and April. Summer warming begins in June around the Faroes, near the southwest Iceland coast and over the Norwegian shelf. By July, the warming spreads over the entire area of the Nordic Seas, except for the northern Barents Sea, where the transition to positive anomalies ends only in August–September. October is a very warm month in the northern Barents Sea at 50 m, contrary to the surface (not shown), where an intensive cooling begins earlier. The magnitude of seasonal variations of the mean temperature reaches 4–5 °C with maximum fluctuations to the west of Spitsbergen and in the Barents Sea.

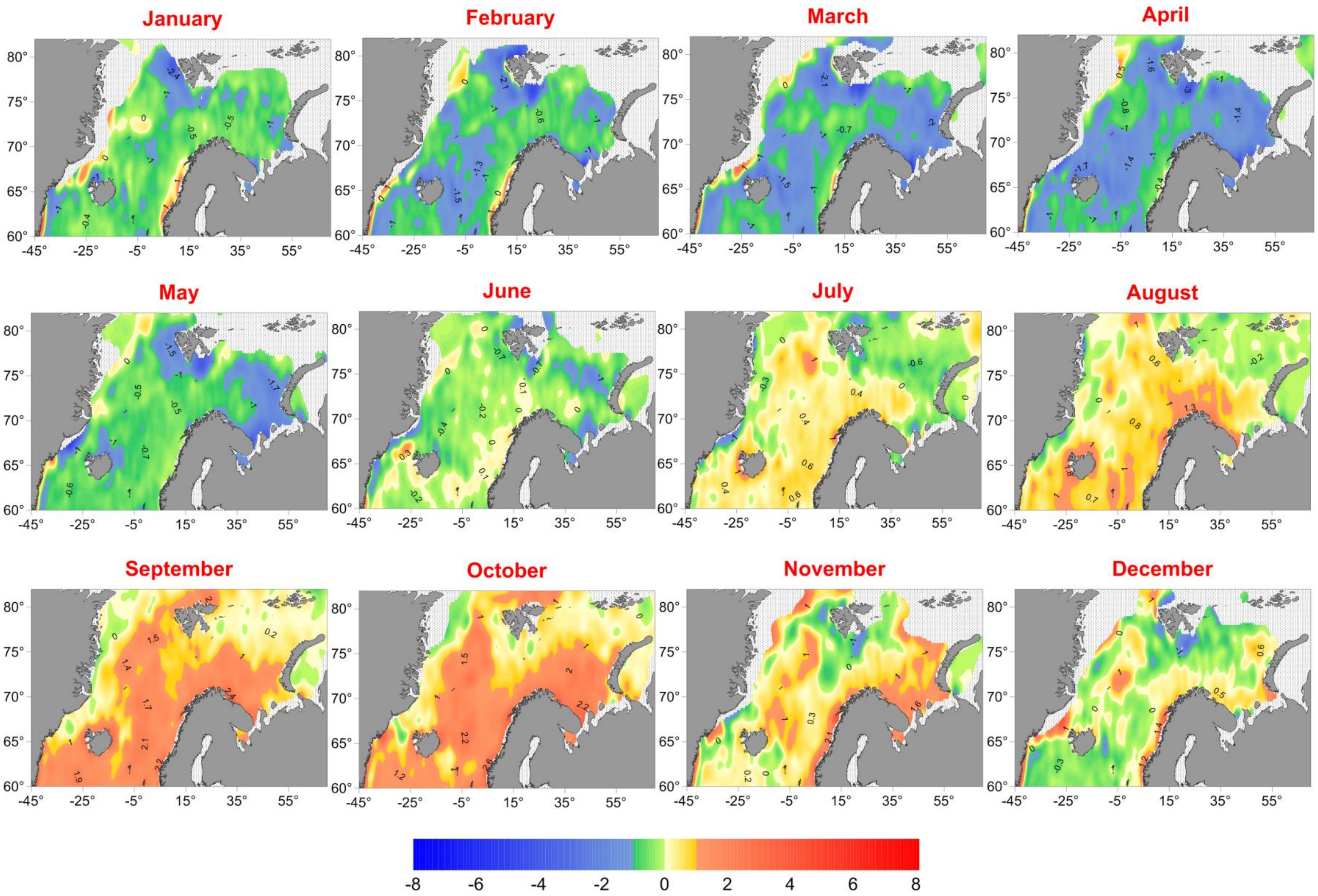

Figure 6.20 Monthly mean (1900–2012) anomalies of temperature (°C) at 50 m relative to the 1900–2012 reference period.

Based on our analysis of temporal variations of the thermohaline variables (Section 5), we identify several abnormal periods in the Atlas domain divided in regimes and events. To obtain the corresponding spatial patterns – the horizontal distributions of temperature, salinity and density were plotted at 50 m (Fig. 6.21–6.23) for the detected regimes (1950–1970, 1976–1999, and 2000–2012) and events (1960–1970, 1976–1982, and 1992–1998). The left panels in the figures represent relatively stable hydrographic regimes (labeled R1, R2 and R3), while the right panels illustrate the events associated with strong salinity fluctuations (labeled S2+, S3–, S4–, S3+, see also Fig. 5.2, 5.4). The warm and saline regime 'R3' is still ongoing and is so far an 'S3+' event. The magnitude of the anomalies averaged over long periods is certainly low (for better reference see the time-depth diagrams, e.g. Fig. 5.3–5.5), but the distributions clearly show the trends.

The 'R1' regime – the one with elevated salinity – is not actually characterized by warmer water, in contrast to the 'R3' regime with warming of exceptional intensity. Another warm period, in the 1930s, also contributed to warming of the background of the 1900–2012-reference field. The cold and low-salinity regime 'R2' was maintained by the two strong low salinity anomalies (S3–, S4–). The 'S3–' event represents the GSA propagation across the region (discussed in Introduction), while the 'S4–' event is linked to the low-salinity anomaly of the mid-1990s. As the time-depth diagrams reveal, the difference between the two events is that the GSA caused the strongest salinity decline at the surface, while the second anomaly was a subsurface event. Moreover, the area affected by the 'S4–' was smaller and confined within the southern part of the Nordic Seas. The R3 regime is characterized by the strongest and broadest density decrease in the upper layer..

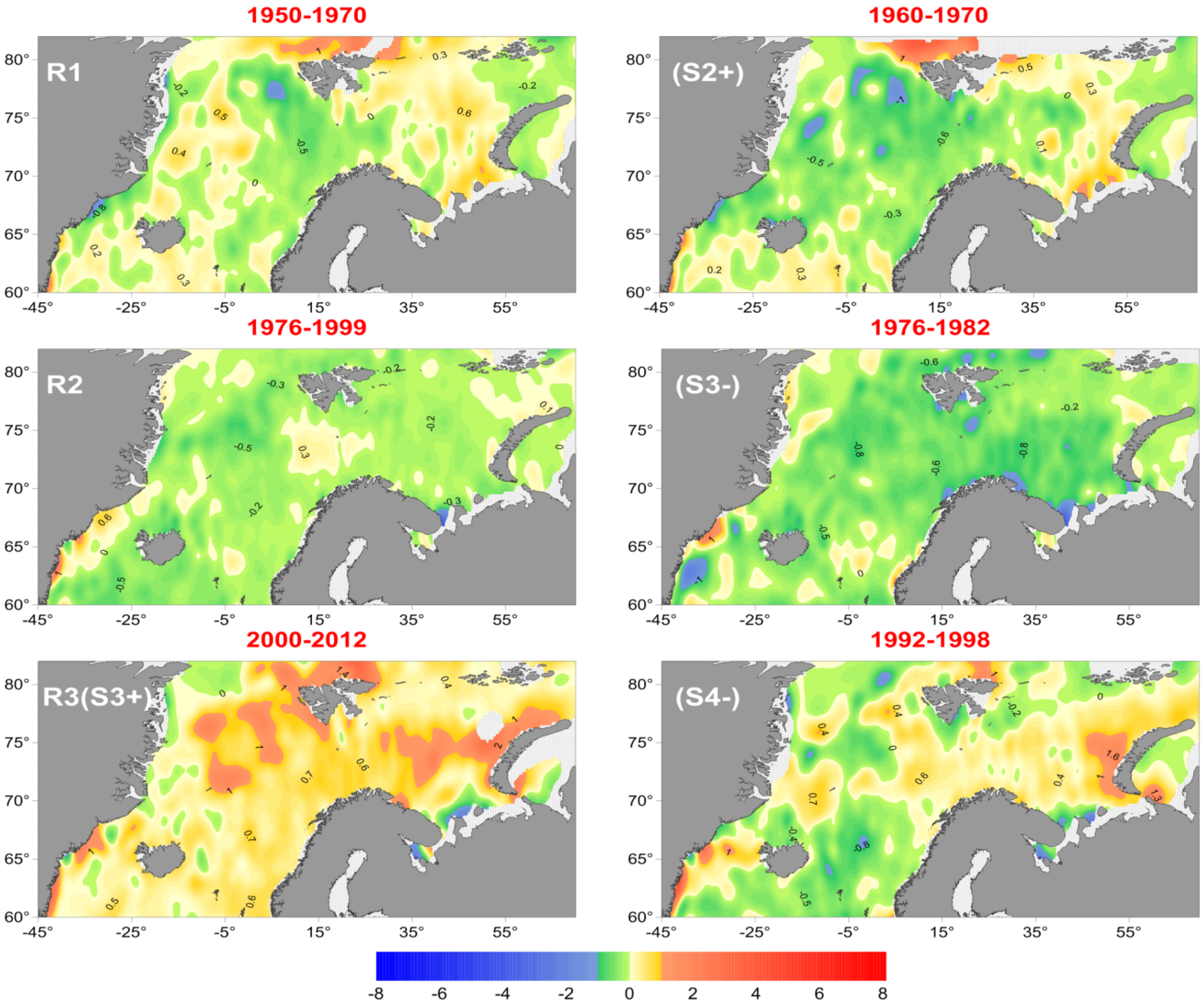

Figure 6.21 Annual mean temperature anomalies (°C) at 50 m relative to the 1900–2012 reference period for the stable regimes (labeled as R) and events (labeled as S).

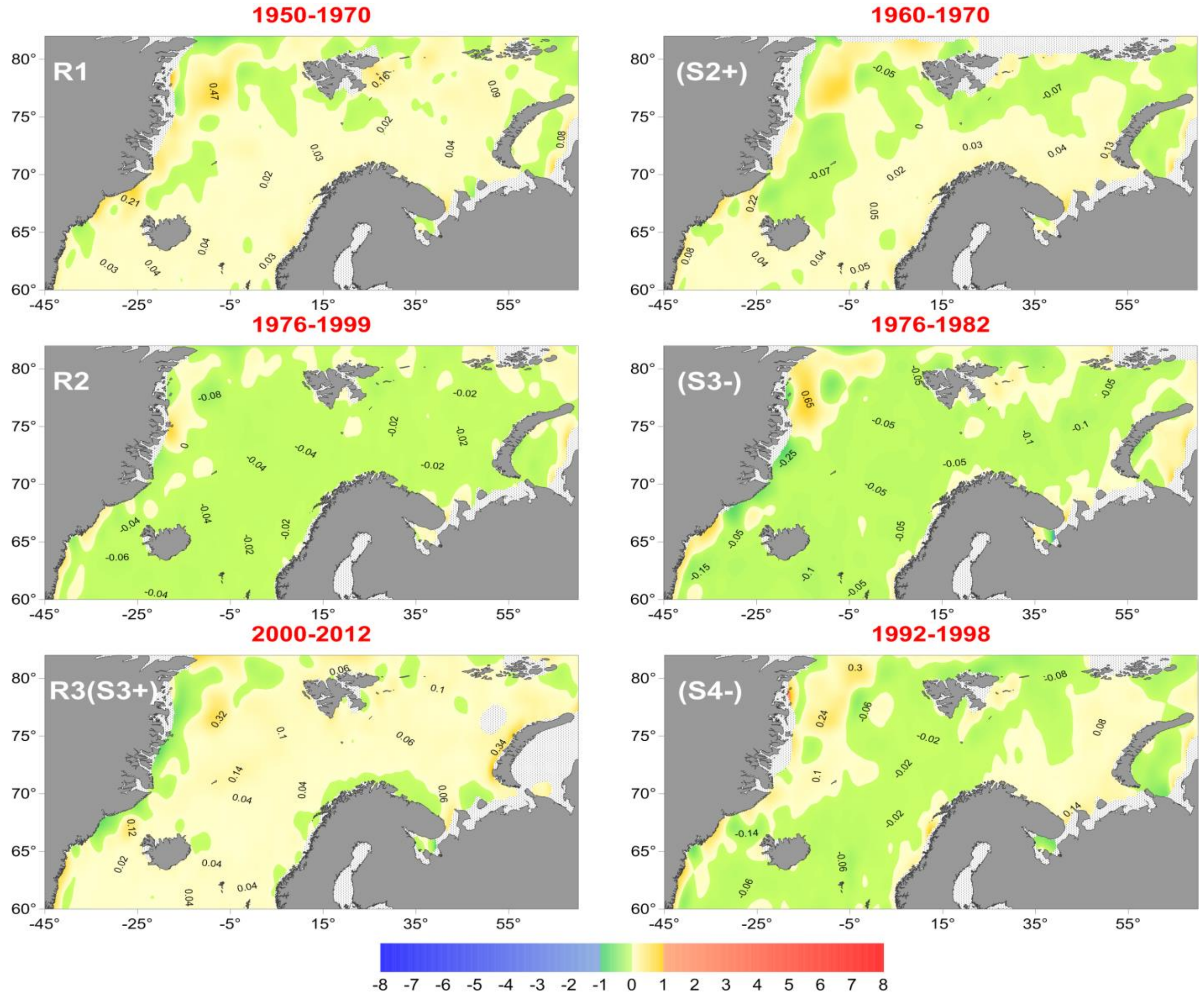

Figure 6.22 Annual mean salinity anomalies at 50 m relative to the 1900–2012 reference period for the stable regimes (labeled as R) and events (labeled as S).

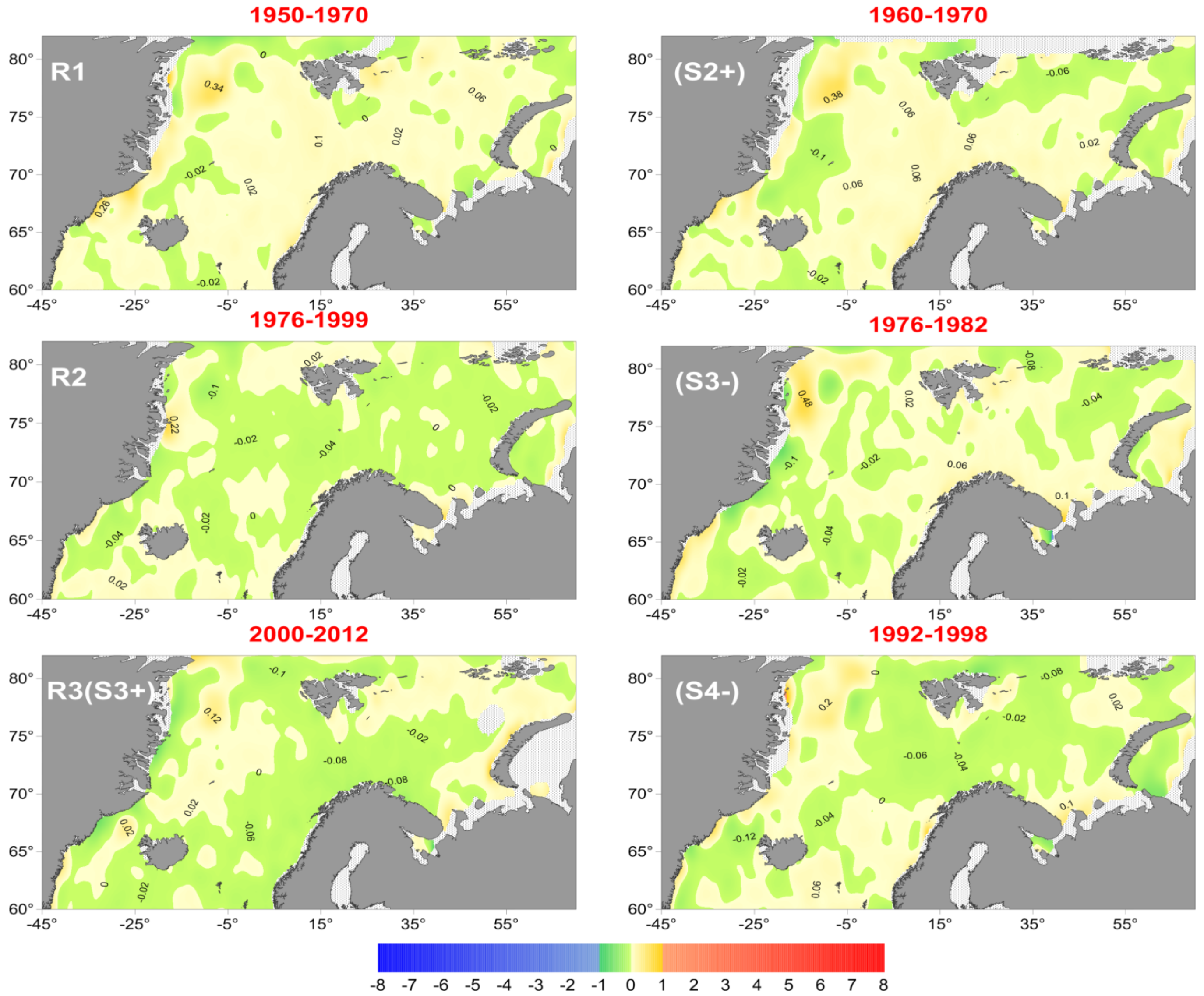

Figure 6.23 Annual mean density anomalies (kg/m^3) at 50 m relative to the 1900–2012 reference period for the stable regimes (labeled as R) and events (labeled as S).

6.6 Temporal variability

Consistency of the horizontal gridded fields was additionally checked by analyzing time-series in the grid's nodes. Numbers of the months and years for which the values can be extracted from the monthly and yearly fields for the 1900–2012 period are shown in figures 6.24, 6.25. The distributions look like a smoothed version of the *in situ* data location (see station position for the whole period on www.nodc.noaa.gov/OC5/nordic-seas/atlas/inventory.html), but add a temporal component to the data description. The eastern part of the Atlas domain is better covered by observations and therefore is the area where the longest time series are located. Not only the amount of measurements, but also their positions relative to interpolation nodes are important (Section 3). If the entire area and each month of the year from 1900 to 2012 were uniformly covered by data, every node would contain 113 yearly or 1,356 monthly estimated values, respectively. In reality, the length of the time series is not uniformly distributed even in well-sampled parts of the Atlas domain. Obviously, the nodes with the longest records are concentrated around long-term monitored sites: ocean weather ships and standard sections.

The grid nodes with the maximum number of months (> 800) are found in the North Sea. The next large node cluster, with 785 months or 58% of the maximum amount, is close to the OWSM location, where the monthly observations were conducted regularly since 1948 (Fig. 6.24). Surprisingly, the cluster location does not coincide with the OWSM fixed location (66° N, 2° E) due to vessels drifting. The other nodes with long time series are located at the Faroe-Shetland Chanel, Barents Sea Opening and Kola Section. Distribution of the time series' length expressed in years (Fig. 6.25) is obviously similar to the monthly map. The longest records are found in the North Sea (99–100 years) and in the Faroe-Shetland Channel (99 years). In the Barents Sea, the number of years with estimations counts up to 95 and 84 for the Kola Section and the Barents Sea Opening, respectively.

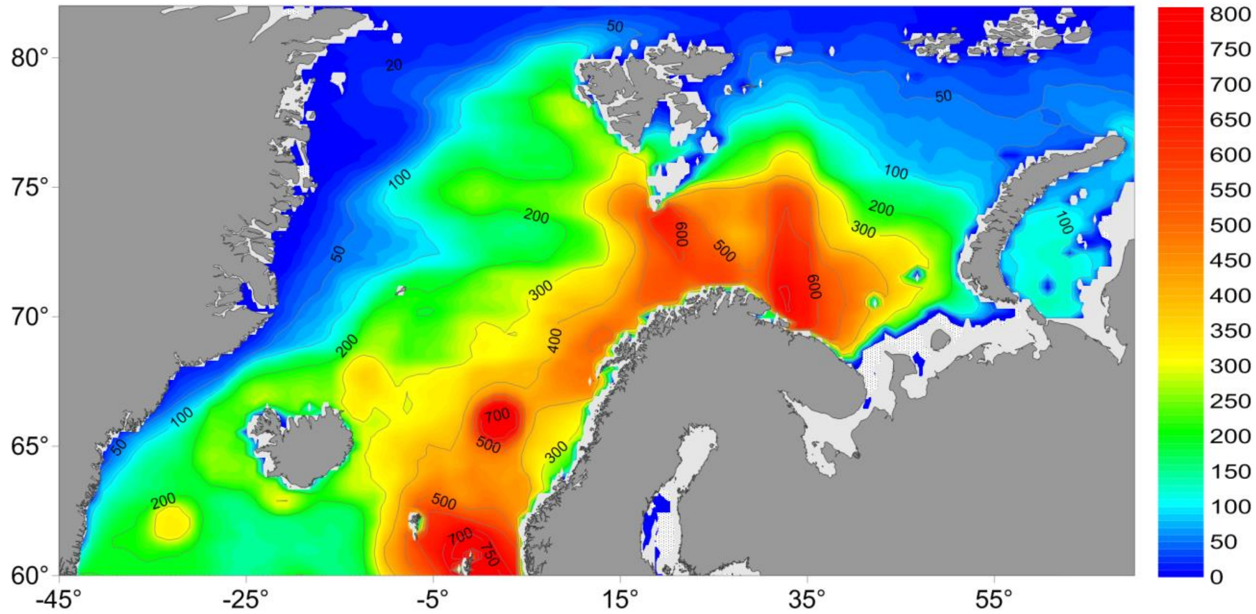

Number of months with estimated temperature (relative error < 0.25)

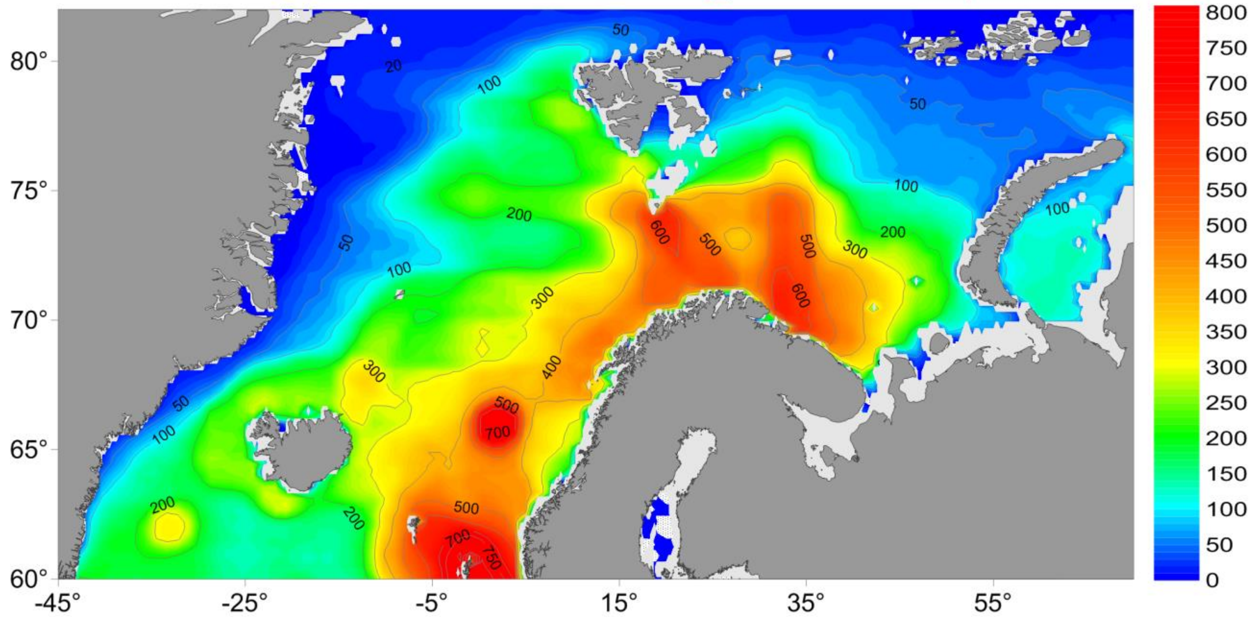

Number of months with estimated salinity (relative error < 0.25)

Figure. 6.24 Number of months with estimated temperature (top) and salinity (bottom) in mesh nodes of the monthly gridded fields for 1900–2012, where the relative error of interpolation is less than 0.25.

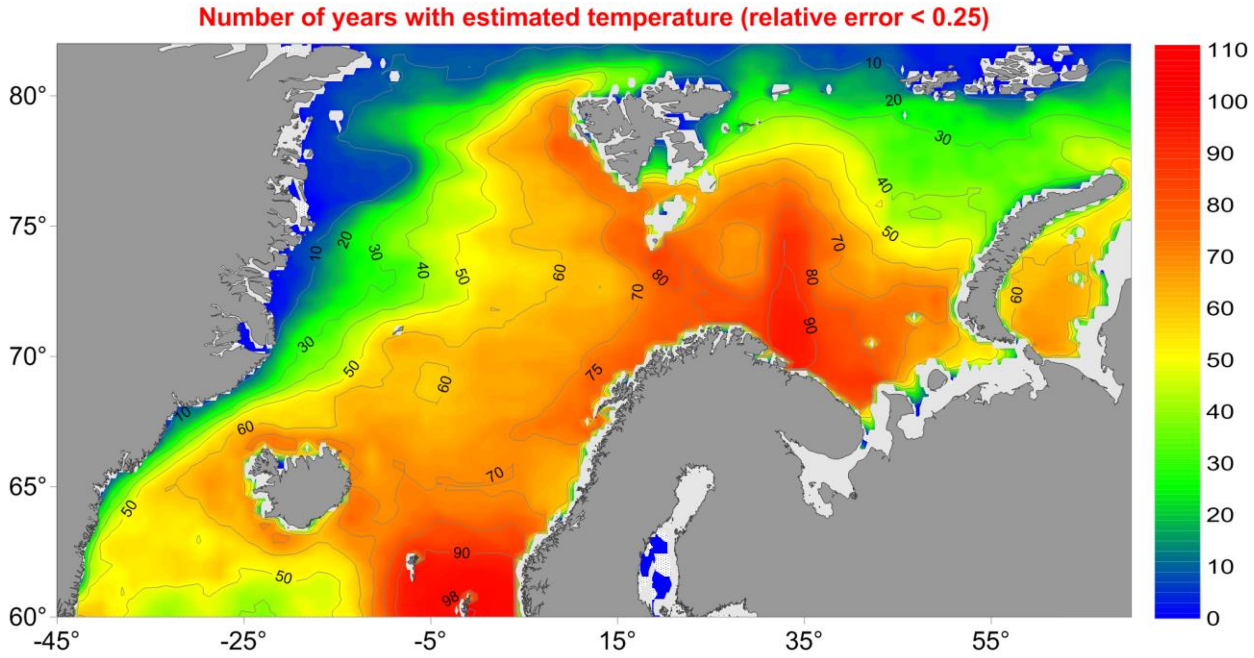

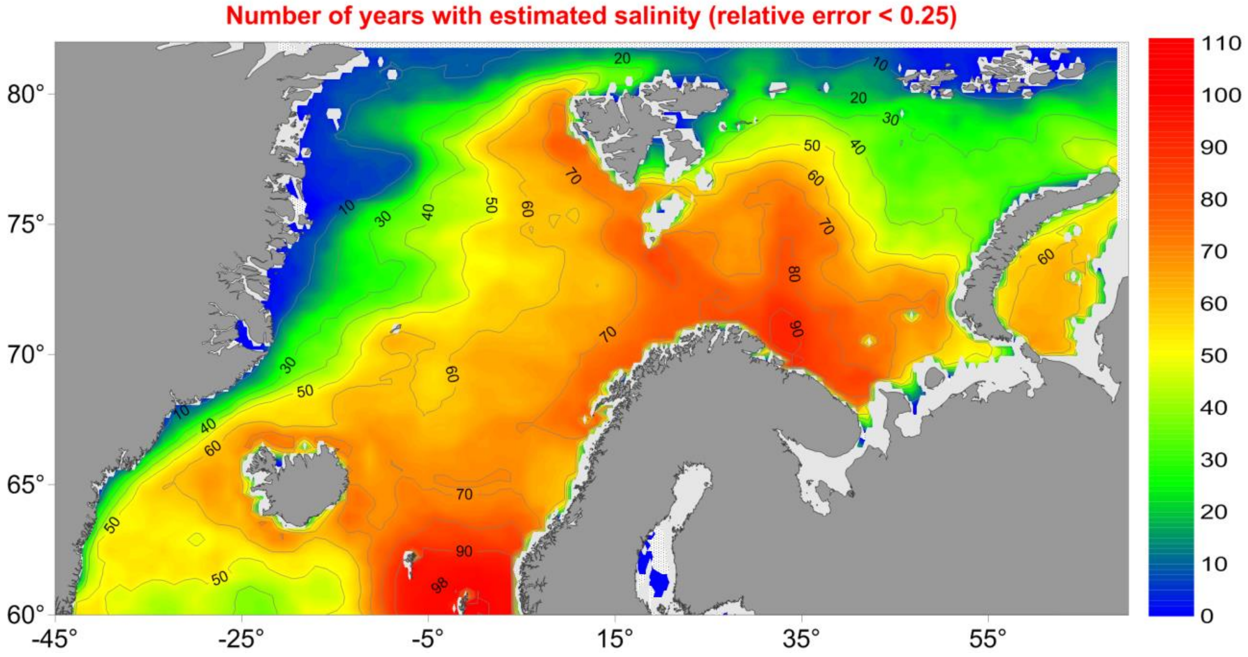

Figure. 6.25 Number of years with estimated temperature (top) and salinity (bottom) in mesh nodes of the yearly gridded fields for 1900–2012, where the relative error of interpolation is less than 0.25.

The most critical questions are: accuracy of the estimations; and reliability of the natural signals in the time series extracted from the grid nodes. In previous sections we discussed the interpolation errors and how well the temporal variability can be assessed based on the interpolated data. As an example, the time series of estimated temperature at the OWSM location is shown in Fig. 6.26. The estimated monthly values were compared with the *in-situ* data selected in 50 km radius around the OWSM central point.

There is a close agreement between monthly-averaged and *in situ* values (not shown). The smoothed curve clearly shows all major regimes and anomalous periods. Furthermore, we extracted temperature and salinity time series at 50 m depth from the above mentioned nodes with the maximum number of the estimated months (Fig. 6.27). They are located in the Atlantic water carried northward by the Norwegian Atlantic Current and the North Cape Current, and thus represent the Atlantic water transformation. The records give the magnitude of cooling and freshening along the trajectory as well as the timing of the major anomalies propagation. Notably, the time series from a single node do not provide the smoothed variability of the time-depth diagrams.

Some fluctuations are linked to natural regional factors (a frontal zone movement, for instance), whereas an artificial component is linked to the ability of the available observations to resolve these fluctuations. Furthermore, the uncertainties inherited by monthly fields from the data should always be taken into account. Nevertheless, the warming of the 1930s, 1960s and 2000s, the GSA’s propagation, and freshening of the mid-1990s are evident in in Fig. 6.27 showing how the Atlantic water steadily loses its identity by cooling by more than 5 °C between the FSC and KS and freshening by 0.8 between FSC and the grid nodes located in BSO.

A comparison with *in situ* data was made for the upper 50 m temperature time series in 12 areas where the time-depth diagrams was computed (Table 2; not shown). It was concluded that the gridded data represent variability relatively well. However, the lack of data in certain months does not permit the horizontal interpolation and, thus, introduces gaps in the records derived from the gridded fields. The time series, therefore, are not equally substantiated and thus are not fully comparable. Moreover, one has to keep in mind that spatial heterogeneity introduces another type of uncertainty into time series, when *in situ* data is utilized without interpolation.

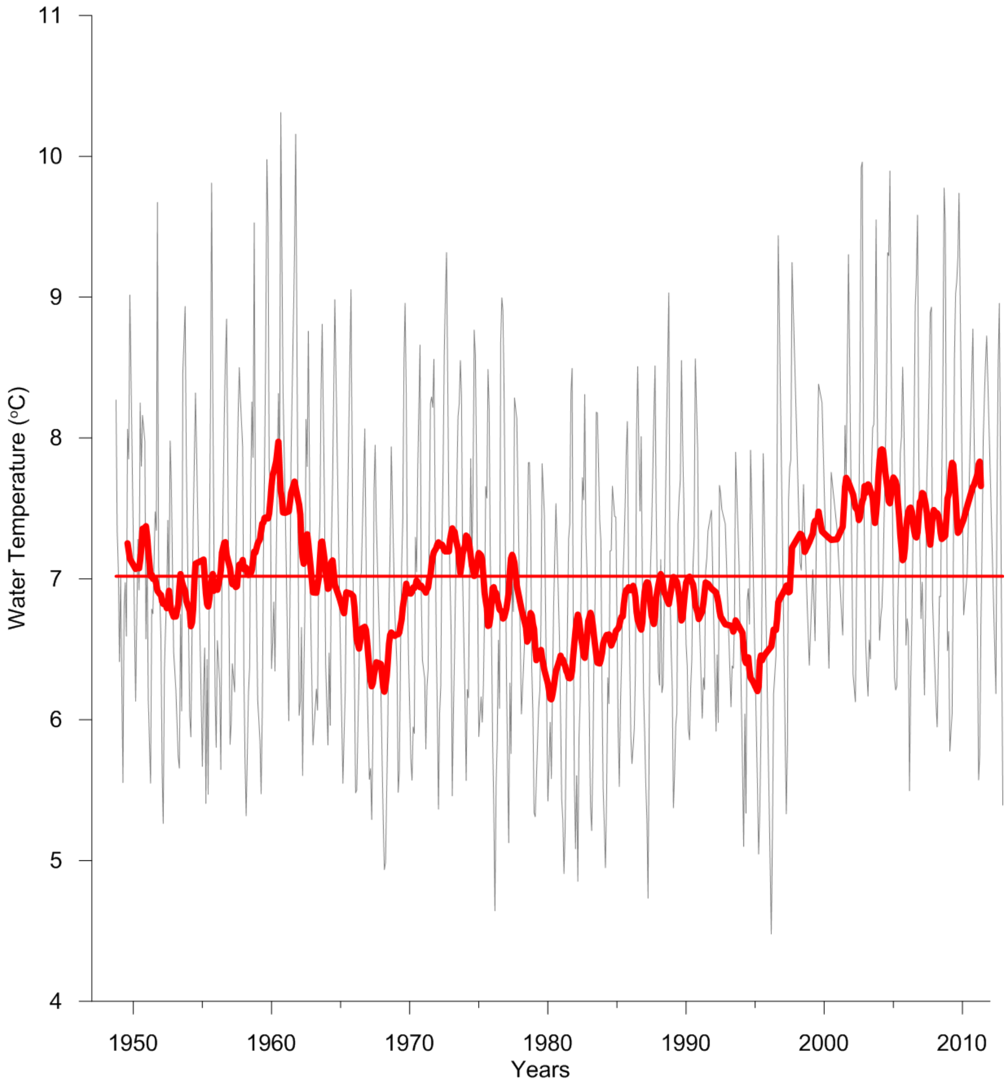

Figure. 6.26 Time-series of estimated temperature (gray curve – monthly values, red curve – running average, red line – the mean) for 1948–2012, in the grid node with the longest record (66.75° N, 1° E) found at 50 m depth close to the OWSM location (declared point 66° N, 2° E). The estimated values were extracted from the monthly gridded fields, where the relative error of interpolation was less than 0.25.

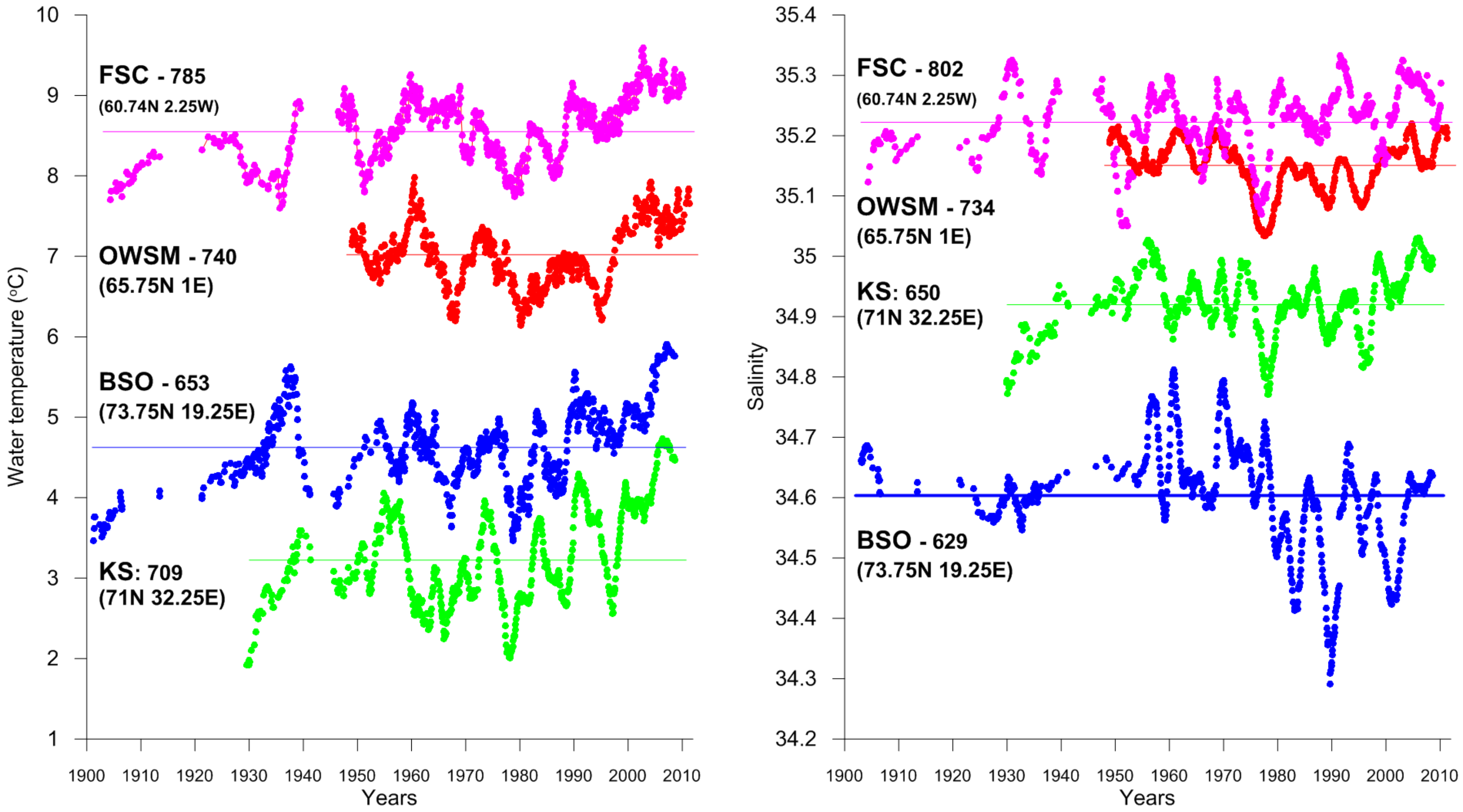

Figure. 6.27 Time series (running average) of temperature (left) and salinity (right) extracted from the monthly fields' mesh nodes with maximal number of estimated values at four locations in the Nordic Seas: Faroe-Shetland Channel (FSC), Ocean Weather Ship 'Mike' (OWSM), Barents Sea Opening (BSO) and Kola Section (KS). Number of estimated values and coordinates of the selected nodes are provided for each location.

7. SUMMARY AND PROSPECTS

We have described the technology of the regional oceanographic climatological dataset compilation based on extended and updated *in situ* observations and a state-of-the-art interpolation method. The oceanographic observations included in this Atlas are part of the World Ocean Database 2013, which is publicly available on the NODC website (www.nodc.noaa.gov/OC5/WOD13). All data and relevant supplement information, including this report, are freely available for downloading from the NOAA/NODC web page (www.nodc.noaa.gov/OC5/nordic-seas).

The authors and editors believe that the Atlas will be a useful tool for a large variety of applications and will provide a basis for future improvements. There are several directions for upgrading, developing and extending the Atlas. We want to emphasize that every measurement ever made in the area is important and should be publically available. Still, significant efforts are required for assembling a complete historical dataset for the Nordic Seas. The technology itself provides needed procedures albeit some modifications are still required. For instance, the vertical interpolation of profiles introduces significant errors, reduces reliability and the extent of the gridded fields. The procedure is especially unsafe for the low-resolution historical profiles. A workaround is to skip this step by using three-dimensional analysis instead of two-dimensional one. Within such an approach, all profiles at all levels for a certain period would be analyzed together. Another way to improve the consistency would be to apply some dynamical constraints during the analysis (based on bottom topography or observed/modeled current); in fact, DIVA already provides such an opportunity.

In our project, we focused on computing and displaying horizontal gridded fields, which can be used for ocean climate studies, especially those addressing the ocean change since the beginning of reliable instrumental observations. Including gridded datasets for vertical sections could have extended the content of the Atlas, but was left for future developments. There are a number of standard sections across the Atlantic water flow from the Faroe-Shetland Channel to the Fram Strait and the Barents Sea. They provide more detailed description of pattern and magnitude of the climatic signals which propagating across the region. In a gridded form, such subsets can be useful for studies of long-term ocean variability, as well as for model verification.

Collaboration on compiling and maintaining large datasets is highly desirable and is the key for further success of ocean climatology. Authors and editors will be grateful for any feedback from the scientific community concerning both the *in situ* dataset and the employed analytical technique. Any advices on improving the historical dataset quality will be very much welcome and appreciated.

8. APPENDIX

Table 3. Technological procedures of the database compilation

A. Compilation of the source databases

1. Defining the metadata composition and database structure
2. Compilation of supporting databases for the gridded bathymetry (GEBCO) and international codes for country/ vessels names (merged NODC, ICES, Climatic Atlas of the Arctic Seas)
3. Developing software for converting the original data to the internal Interbase 7.0 format
4. Downloading data from initial data sources into individual databases
5. Updating metadata by adding bottom depths from gridded bathymetry and last measured level at station
6. Deleting the stations outside the Nordic Seas geographic region
7. Executing quality control and setting the quality control flags on observed level data:
   - range check
   - maximum allowable number of observed level
   - depth inversions
   - depth duplicates
   - minimum allowable number of observed level
   - stability and vertical gradients
   - stations exact duplicates

B. Compilation of the integrated observed level database, duplicate control, assigning quality control flags

1. Merging of the individual databases into integrated database with instrument control
2. Executing automated duplicate control with metadata and profiles merging:
   - exact duplicates
   - TSO2 duplicates
   - CTD with different resolution
   - different variants of interpolated profiles
3. Executing expert duplicate control with metadata and profiles merging:
   - all station with the same date within +/- 1’
   - computing of the variables standard deviations (SD) for every month of the year in the layers around the standard levels, quality control flags assigning on values outside 3,4,5 SD

Table 4. Metadata composition: STATION

#	Field name	Description
1	ABSNUM	Unique ID
2	STFLAG	Quality flag (See Appendix, Table 7)
3	STLAT	Longitude (in degrees and decimal degrees)
4	STLON	Latitude (in degrees and decimal degrees)
5	STDATE	Station date
6	STTIME	Station time
7	STSOURCE	Source where station has been obtained from
8	STVERSION	Version of station
9	STCOUNTRYNAME	Country name
10	STVESSELNAME	Vessel name
11	STDEPTHSOURCE	Depth from initial source
12	STLASTLEVEL	Depth of the last measured level
13	STDEPTHGRID	Bottom depths from GEBCO (BODC, 2003) bathymetry at station
14	STDEPTHGRIDMIN	Bottom minimum depths from GEBCO (BODC, 2003) bathymetry in five kilometers radius around station
15	STDEPTHGRIDMAX	Bottom maximum depths from GEBCO (BODC, 2003) bathymetry in five kilometers radius around station

Table 5. Metadata composition: STATION_INFO

#	Field name	Description
1	ABSNUM	Unique ID (linked to the STATION table)
2	COUNTRYCODE	International country code
3	VESSELCODE	International vessel codes
4	STNUMINCRUISE	Station number in cruise
5	PROJECTCODE	Code of project
6	INSTITUTECODE	Code of institute
7	INSTRUMENT	Instrument type
8	SOURCEUNIQUEID	Unique number from the source
9	SOURCEDATAORIGIN	Name of the secondary source
10	VESSELCRUISEID	Cruise number

Table 6. Structure of a data table

#	Field name	Description
1	ABSNUM	Unique ID (linked to the STATION table)
2	LEVEL_	Depth
3	VALUE_	Variable value
4	FLAG_	Quality flag (See Appendix, Table 8)

Table 7. Meaning of the quality control StFlag of the table 'Station'

#	Flag	Description
1	1	Last observed level at station exceed maximum depth inside 5 km radius around station from GEBCO bathymetry
2	2	Station on shore
3	4	Time lag between the stations inside a cruise is not realistic (possible error in metadata)
4	8	Not in use
5	16	Time is absent
6	32	Station date was changed (days in a month)
7	64	Station date was changed (time format)
8	128	Accuracy of the temperature probe <0.01° C
9	256	Accuracy of the salinity probe <0.02 psu
10	512	NODC ship code not unique or absent in support database
11	1024	Not in use
12	2048	Profiles combined from different stations
13	4096	Metadata combined from different stations
14	8192	Chemistry has not passed quality control
15	16384	Observations at the station are suspicions
16	32768	Observations at the station are erroneous

Table 8. Meaning of the quality control Flag_ of parameter tables

#	Flag	Description
1	0	Flag is not set
2	1	Accuracy lost (from source)
3	2	Suspicious value (from source)
4	4	Erroneous value (from source)
5	8	Interpolated value
6	16	Chemistry units recalculated
7	32	Depth from pressure
8	64	Range error
9	128	Stability error
10	256	=Reserved=
11	512	Duplicate analysis
12	1024	Outside 3 SD (Standard Deviation)
13	2048	Outside 4 SD
14	4096	Outside 5 SD
15	8192	= Reserved=
16	16384	Suspicious value
17	32768	Erroneous value

9. REFERENCES

1. Aagaard, K., Swift, J.H. and Carmack, E.C., (1985), Thermohaline circulation in the Arctic Mediterranean Seas. Journal of Geophysical Research, 90, C3, pp. 4833-4846.
2. Anderson, L. G., Falck, E., Jones, E. P., Jutterstrom, S., and Swift, J. H., (2004), Enhanced uptake of atmospheric CO2 during freezing of seawater: A field study in Storfjorden, Svalbard, J. Geophys. Res., 109, C06004, doi:10.1029/2003JC002120.
3. Årthun, M., Ingvaldsen, R.B., Smedsrud, L.H., Schrum, C., (2011), Dense water formation and circulation in the Barents Sea. Deep-Sea Res. I, 58, pp. 801–817.
4. Årthun, M., Eldevik, T., Smedsrud, L.H., Skagseth, Ø., and Ingvaldsen, R., (2012), Quantifying the influence of Atlantic heat on Barents Sea ice variability and retreat. J. Climate, 25, pp. 4736–4743.
5. Bacon, S, Reverdin G, Rigor I.G., Snaith H.M., (2002), A freshwater jet on the East Greenland Shelf. J. Geophys. Res. 107, doi:10.1029/2001JC000935.
6. Bacon, S., Myers, P.G., Rudels, B., and Sutherland, D.A., (2008), Accessing the Inaccessible: Buoyancy-Driven Coastal Currents on the Shelves of Greenland and Eastern Canada. In Arctic–Subarctic Ocean Fluxes: Defining the Role of the Northern Seas in Climate, edited by R. R. Dickson, J.Meincke, and P. Rhines, Springer, New York, pp. 703–723.
7. Belkin, I.M., Levitus, S., Antonov, J.I., and Malmberg, S.-A., (1998), “Great Salinity Anomalies” in the North Atlantic, Prog. Oceanogr., 41, pp. 1–68.
8. Belkin, I.M., (2004) Propagation of the “Great Salinity Anomaly” of the 1990s around the northern North Atlantic. Geophys. Res. Lett., 31, L08306.
9. Beszczynska-Moller, A., Fahrbach, E., Schauer, U., Hansen, E., (2012), Variability in Atlantic water temperature and transport at the entrance to the Arctic Ocean, 1997–2010., ICES J. Mari. Sci. 69, pp. 852-863.
10. Blindheim, J., (1990), Arctic intermediate water in the Norwegian Sea. Deep-Sea Research, 37, pp. 1475-1489.
11. Blindheim, J., Osterhus, S., (2005), The Nordic Seas, main oceanographic features. In: Drange, H., Dokken, T., Furevik, T., Gerdes, R., Berger, W. (Eds.), The Nordic Seas–integrated perspective: oceanography, climatology, biogeochemistry, and modelling (Geophysical Monograph 158), American Geophysical Union, pp. 11–38.
12. Blindheim, J., Borovkov, V., Hansen, B., Malmberg, S.A., Turrell, W.R., and Osterhus, S., (2000), Upper layer cooling and freshening in the Norwegian Sea in relation to atmospheric forcing, Deep Sea Research, Part I, 47, pp. 655–680.

13. Bonisch, G., Blindheim, J., Bullister, J., Schlosser, P., and Wallace, D., (1997), Long-term trends of temperature, salinity, density, and transient tracers in the central Greenland Sea, J. Geophys. Res., 102, pp. 18553–18571.
14. Bourke, R.H., Paquette, R.G., Blythe, R.F., (1992), The Jan Mayen Current of the Greenland Sea. J. Geophys. Res. 97, pp. 7241–7250.
15. Boyer, T., Antonov, J.I., Garcia, H., Johnson, D.R., Locarnini, R.A., Mishonov, A.V., Pitcher, M.T., Baranova, O.K., and Smolyar, I., (2006). World Ocean Database 2005, Chapter 1: Introduction, NOAA Atlas NESDIS 60, Ed. S. Levitus, U.S. Government Printing Office, Washington, D.C., 182 pp.
16. Budeus, G., Cisewski, B., Ronski, S., Dietrich, D., and Weitere, M. (2004), Structure and effects of a long lived vortice in the Greenland Sea, Geophys. Res. Lett., 31, L05304, doi:10.1029/2003GL017983.
17. Carmack, E., and Aagaard, K., (1973), On the deep water of the Greenland Sea. Deep-Sea Research, 20, pp. 687-715.
18. Curry, R., Dickson, B., Yashayaev, I., (2003), A change in the freshwater balance of the Atlantic Ocean over the past four decades. Nature 426, pp. 826–829.
19. Curry, R., Mauritzen, C., (2005), Dilution of the Northern North Atlantic Ocean in recent decades. Science, 308 (5729), pp. 1772-1774.
20. Dickson, R.R., Meincke, J., Malmberg, S.A., Lee, A.J., (1988), The «Great Salinity Anomaly» in the northern North Atlantic, 1966–1982, Progress in Oceanography, 20, 2, pp. 103–151.
21. Dickson, R.R., Meincke, J., Rhines, P., (2008), Arctic–Subarctic Ocean Fluxes. Dordrecht: Springer Science, 736 pp.
22. Dickson, R.R, Lazier, J., Meincke, J., Rhines, P., Swift J., (1996), Long-term Coordinated Changes in the Convective Activity of the North Atlantic. Prog. Oceanogr., 38, pp. 241–295.
23. Dickson, R.R., Meincke, J., Malmberg, S.-A., Lee, A.J., (1988), The Great Salinity Anomaly in the northern North Atlantic 1968–1982. Prog. Oceanogr., 20, pp. 103–151.
24. Dickson, R.R., Rudels, B., Dye, S., Karcher, M., Meincke, J., Yashayaev, I., (2007), Current estimates of freshwater flux through Arctic and subarctic seas. Prog. Oceanogr., 73, pp. 210–230.
25. Drange, H., Dokken, T., Furevik, T., Gerdes, R., and Berger, W. (Eds.), (2005), The Nordic Seas: An Integrated Perspective Oceanography, Climatology, Biogeochemistry, and Modeling, Geophys. Monogr. Ser., AGU, Washington, D. C., 158, 366 pp.

26. Eldevik, T., and Nilsen, J.E.Ø., (2013), The Arctic–Atlantic thermohaline circulation. J. Climate, 26, pp. 8690–8705.

27. Eldevik, T., Nilsen, J. E. Ø., Iovino, D., Olsson, K.A., Sandø, A.B., and Drange H., (2009), Observed sources and variability of Nordic Seas overflow. Nat. Geosci., 2, pp. 406–410.

28. Eldevik, T., Straneo, F., Sandø, A.B. & Furevik, T., (2005), Pathways and Export of Greenland Sea Water. In The Nordic Seas: An Integrated Perspective (Eds. Drange, H., Dokken, T. M., Furevik, T., Gerdes, R. & Berger, W.), Geophysical Monograph Series 158, American Geophysical Union, pp. 89-103.

29. Fogelqvist, E., Blindheimb, J., Tanhuac T., Osterhus S., Buche E., Reyb F., (2003), Greenland–Scotland overflow studied by hydro-chemical multivariate analysis, Deep Sea Res., Part I, 50 (2003), pp. 73–102.

30. Furevik, T., (2001), Annual and interannual variability of Atlantic Water temperatures in the Norwegian and Barents Seas: 1980-1996, Deep Sea Res., Part I, 48 (2), pp. 383-404.

31. Gammelsrod, T., Leikvin, O., Lien, V., Budgell, W.P., Loeng, H., Maslowski, W., (2009), Mass and heat transports in the NE Barents Sea: observations and models. J. Mar. Syst. 75, pp. 56–69.

32. Gascard, J.-C., Watson, A.J., Messias, M-J., Olsson, A., Johannessen, T. And Simonsen K., (2002), Long-lived vortices as a mode of deep ventilation in the Greenland Sea, Nature, 416, pp. 525–527.

33. Great Soviet Encyclopedia, online version, dic.academic.ru/dic.nsf/enc3p/266810.

34. Hansen, B., and Osterhus, S., (2000), North Atlantic-Nordic Seas exchanges, Prog. Oceanogr., 45 (2), pp. 109–208.

35. Hansen, B., Osterhus, S., (2007), Faroe Bank Channel overflow 1995–2001. Prog. Oceanogr., 75, pp. 817–856.

36. Hansen, B., Osterhus, S., Turrell, W.R., Jonsson, S., Valdimarsson, H., Hatun, H., and Olsen, S.M., (2008), The inflow of Atlantic water, heat, and salt to the Nordic Seas across the Greenland-Scotland Ridge, in Arctic–Subarctic Ocean Fluxes: Defining the Role of the Northern Seas in Climate (eds. R.R. Dickson, J. Meincke, and P. Rhines), Springer, New York., pp. 15–43.

37. Hatun H., Sando A.B., Drange H., Hansen B., Valdimarsson H., (2005), Influence of the Atlantic Subpolar Gyre on the Thermohaline Circulation, Science, 309, pp. 1841–1844.

38. Helland-Hansen, B., Nansen, F., (1909), The Norwegian Sea. Its physical oceanography based upon the Norwegian researches 1900–1904. In Report on Norwegian Fishery and marine investigations, vol. II (I), Mallingske, Christiania, pp. 360.

39. Holfort, J., Hansen, E., Østerhus, S., Dye, S., Jonsson, S., Meincke, J., Mortensen, J., and Meredith, M., (2008), Freshwater Fluxes East of Greenland.In Arctic–Subarctic Ocean Fluxes: Defining the Role of the Northern Seas in Climate, (eds. R.R. Dickson, J. Meincke, and P. Rhines), Springer, New York, pp. 263–289.
40. Hopkins, T.S., (1991), The Gin Sea – A synthesis of its physical oceanography and literature review 1972-1985., Earth-Science Reviews, 30, pp. 175-318.
41. Hurdle, B.G., (1986), The Nordic Seas, Springer, New York, 777 pp.
42. Ingvaldsen, R.B., (2005), Width of the North Cape Current and location of the Polar Front in the western Barents Sea, Geophys. Res. Lett., 32, L16603, doi:10.1029/2005GL023440.
43. Ingvaldsen, R.B., Asplin, L., and Loeng, H., (2004a), Velocity field of the western entrance to the Barents Sea, J. Geophys. Res., 109, C03021, doi:10.1029/2003JC001811.
44. Ingvaldsen, R., Asplin, L., Loeng, H., (2004b), The seasonal cycle in the Atlantic transport to the Barents Sea during the years 1997–2001., Cont. Shelf Res. 24, pp. 1015–1032.
45. IOC, IHO and BODC, (2003), Centenary Edition of the GEBCO Digital Atlas, published on CD-ROM on behalf of the Intergovernmental Oceanographic Commission and the International Hydrographic Organization as part of the General Bathymetric Chart of the Oceans, British Oceanographic Data Centre, Liverpool, U.K.
46. Isachsen, P., Mauritzen, C., Svendsen, H., (2007), Dense water formation in the Nordic Seas diagnosed from sea surface buoyancy fluxes., Deep-Sea Res. I 54 (1), pp. 22–41.
47. Ivanov, V.V., and Korablev, A.A., (1995a), Formation and regeneration of the pycnocline lens in the Norwegian Sea, Russ. Meteor. Hydrol., 9, pp. 62–69.
48. Ivanov, V.V., and Korablev, A.A. (1995b), Dynamics of an intrapycnocline lens in the Norwegian Sea. Russ. Meteor. Hydrol., 10, pp. 32–37.
49. Ivanov, V., Korablev, A. & Myakoshin, O., (1996), PC-adapted oceanographic database for studying climate shaping ocean processes. Oceanology International 96. The Global Ocean–Towards Operational Oceanography. Conference proceedings, New Malden, UK: Spear-head Exhibitions Ltd., Vol. 1, pp. 89-99.
50. Ivanov, V.V., Shapiro, G.I., (2005), Formation of a dense water cascade in the marginal ice zone in the Barents Sea. Deep Sea Res., Part 1, 52 (9), pp. 1699–1717.
51. Jakobsen, P.K., Ribergaard, M.H., Quadfasel D., Schmith, T., and Hughes, C.W., (2003), Near-surface circulation in the northern North Atlantic as inferred from Lagrangian drifters: Variability from the mesoscale to interannual, J. Geophys. Res., 108 (C8), 3251, doi:10.1029/2002JC001554.

52. Jeansson, E., Jutterstrom, S., Rudels, B., Anderson, L.G., Olsson, K.A., Jones, E.P., Smethie Jr., W.M., Swift, J.H., (2008), Sources to the East Greenland Current and its contribution to the Denmark Strait Overflow., Prog. Oceanogr., 78, pp. 12–28.
53. Jochumsen, K., Quadfasel, D., Valdimarsson, H., Jonsson, S., (2012), Variability of thevDenmark Strait overflow: Moored time series from 1996–2011., J. Geophys. Res., 117, C12003, dx.doi.org/10.1029/2012JC008244.
54. Johnson, D.R., Boyer, T.P., Garcia, H.E., Locarnini, R.A., Baranova, O.K., and Zweng, M.M., (2009), World Ocean Database 2009 Documentation. Edited by Sydney Levitus. NODC Internal Report 20, NOAA Printing Office, Silver Spring, MD, 175 pp.
55. Jonsson, S., Valdimarsson, H., (2012a), Hydrography and circulation over the southern part of the Kolbeinsey Ridge., ICES J. Mar. Sci., 69 (7), pp. 1255–1262.
56. Jonsson, S., Valdimarsson, H., (2012b), Water mass transport variability to the north Icelandic shelf, 1994-2010. ICES J. Mar. Sci., dx.doi.org/10.1093/icesjms/fss024.
57. Jonsson, S., (2007), Volume flux and fresh water transport associated with the East Icelandic Current, Progress in Oceanography, doi: 10.1016/j.pocean.2006.11.003.
58. Kasajima, Y., Olsson, K.A., Johannessen, T., Messias, M-J., Jeansson, E., Bellerby, R.G. J., and Skjelvan, I., (2006), A submesoscale coherent eddy in the Greenland Sea in 2003. J. of Geophys. Res., Vol. 111, C07013, doi:10.1029/2005JC003130.
59. Knudsen, M., (1899), Hydrography. The Danish INGOLF expedition.
60. Köhl, A., (2007), Generation and stability of a quasi-permanent vortex in the Lofoten basin, J. Phys. Oceanog., 37, pp. 2637-2651.
61. Korablev A., Pnyushkov, A., Smirnov, A., (2007), Compiling of the oceanographic database for climate monitoring in the Nordic Seas. In Russian, Trudy AARI, Vol. 447, pp. 85-108.
62. Koszalka, I., LaCasce, J.H., Andersson, M., Orvik, K.A., Mauritzen, C., (2011), Surface circulation in the Nordic Seas from clustered drifters., Deep-Sea Res. I 58 (4), pp. 468–485.
63. Koszalka, I., LaCasce, J.H.,Mauritzen, C., (2013), In pursuit of anomalies–Analyzing the poleward transport of Atlantic Water with surface drifters. Deep-Sea Res. II 85, pp. 96–108.
64. Levitus, S., (2012), The UNESCO/IOC/IODE Global Oceanographic Data Archaeology and Rescue (GODAR) project CODATA Data Sci. J. , 11, pp. 46-71.
65. Levitus, S., Matishov, G., Seidov, D., Smolyar, I., (2009), Barents Sea multidecadal variability., Geophys. Res. Lett., 36, L19604, doi:19610.11029/12009GL039847.

66. Lind, S., Ingvaldsen, R.B., (2012), Variability and impacts of Atlantic Water entering the Barents Sea from the north. Deep-Sea Res. I, 62, pp. 70–88.

67. Loeng, H., Ozhigin, V., and Adlandsvik, B., (1997), Water fluxes through the Barents Sea, J. Mar. Sci., 54, pp. 310–317.

68. Malmberg, S.-A., and Jonsson, S. (1997), Timing of deep convection in the Greenland and Iceland Seas, ICES Journal of Marine Science, 54, pp. 300–309.

69. Mauritzen, C, Price, J., Sanford, T., Torres, D., (2005), Circulation and Mixing in the Faroese Channels. Deep-Sea Research, 52 (6), pp. 883-913.

70. Mauritzen, C., (1996), Production of dense overflow waters feeding the North Atlantic across the Greenland–Scotland Ridge. Part 1: evidence for a revised circulation scheme. Deep-Sea Res., I 43, pp. 769–806.

71. Metcalf, W.G., (1955), On the formation of bottom water in the Norwegian Basin, Trans. AGU., 364, pp. 595-600.

72. Midttun, L., (1985), Formation of dense bottom water in the Barents Sea, Deep-Sea Res. Part A, 32 (10), pp. 1233–1241.

73. Mohn, H., (1887), The North Ocean, its Depths, Temperature and Circulation. The Norwegian North-Atlantic Expedition 1876-1878, Christiania.

74. Nansen, F., (1906), Northern waters: Captain Roald Amundsen's oceanographic observations in the Arctic seas in 1901, Videnskabs-Selskabets Skrifter, I, Mathematisk-Naturv. Klasse, No. 3, 145 pp.

75. Olsson, K.A., Jeansson, E., Anderson, L.G., Hansen, B., Eldevik, T., Kristiansen, R., Messias, M. J., Johannessen, T., Watson, A.J., (2005), Intermediate water from the Greenland Sea in the Faroe Bank Channel: Spreading of released sulphur hexafluoride, Deep-Sea Res. I 52, pp. 279-294.

76. Orvik, K.A., and Niiler, P., (2002), Major pathways of Atlantic water in the northern North Atlantic and Nordic Seas toward Arctic, Geophys. Res. Lett., 29 (19), 1896, doi:10.1029/2002GL015002.

77. Osterhus, S., Turrrell, W.R., Jonsson, S., and Hansen, B., (2005), Measured volume, heat, and salt fluxes from the Atlantic to the Arctic Mediterranean, Geophys. Res. Lett., 32, L07603, doi:10.1029/2004GL022188.

78. Poulain, P.-M., Warn-Varnas, A., Niiler, P.P., (1996), Near-surface circulation of the Nordic Seas as measured by Lagrangian drifters. J. Geophys. Res. 101, pp. 18237–18258.

79. Raj, R.P., Chafik, L., Nilsen, J.E.Ø., and Eldevik, T. (2013), The Lofoten Vortex of the Nordic Seas. In review Deep Sea Res.

80. Reiniger R.F., Ross C.K. (1968), A method of interpolation with application to oceanographic data, Deep Sea Res., vol. 15. pp. 185–193.
81. Rew, R.K., Davis, G.P., Emmerson, S., and Davies, H., (1997), NetCDF User's Guide for C, An Interface for Data Access, Version 3, 189 pp.
82. Ronski, S., and Budeus, G., (2005), Time series of winter convection in the Greenland Sea, J. Geophys. Res., 110, C04015, doi:10.1029/2004JC002318.
83. Rudels, B., Bjork, G., Nilsson, J., Winsor, P., Lake, I., Nohr, C., (2005), The interaction between waters from the Arctic Ocean and the Nordic Seas north of Fram Strait and along the East Greenland Current: results from the Arctic Ocean-02 Oden expedition, J. Mar. Syst. 55, pp. 1–30.
84. Schauer, U., Rudels, B., Jones, E.P., Anderson, L.G., Muench,R.D., Bjork, G., Swift, J.H., Ivanov, V., Larsson, A.-M., (2002b), Confluence and redistribution of Atlantic water in the Nansen, Amundsen and Marakov basins, Annales Geophysicae, 20, pp. 257–273.
85. Skagseth, O., (2004), Monthly to annual variability of the Norwegian Atlantic slope current: Connection between the northern North Atlantic and the Norwegian Sea, Deep Sea Res., Part I, 51 (3), pp. 349–366.
86. Skagseth, O., (2008). Recirculation of Atlantic Water in the eastern Barents Sea.Geophys. Res. Lett., 35, L11606.
87. Skogseth, R., Fer, I., Haugan P.M., (2005), Dense-Water Production and Overflow from an Arctic Coastal Polynya in Storfjorden (Eds. Drange, H., Dokken, T., Furevik, T., Gerdes, R., Berger, W., The Nordic Seas–integrated perspective: oceanography, climatology, biogeochemistry, and modelling), American Geophysical Union, Geophysical Monograph 158, pp. 11–38.
88. Slubowska-Woldengen, M., Rasmussen, T.L., Koc, N., Klitgaard-Kristensen, D., Nilsen, F., Solheim, A., (2008), Time-slice reconstructions of ocean circulation changes on the continental shelf in the Nordic and Barents Seas during the last 16,000 cal yr B.P., Quaternary Science Reviews, 27, pp. 1476–1492.
89. Smirnov A., Korablev, A., Alekseev, G. and Esau, I., (2010), Temporal and spatial changes in mixed layer properties and atmospheric net heat flux in the Nordic Seas, IOP Conf. Ser.: Earth Environ. Sci., 13 012006, doi: 10.1088/1755-1315/13/1/012006.
90. Søiland, H., and Rossby, T., (2013), On the structure of the Lofoten Basin Eddy, J. Geophys. Res. Oceans, 118, pp. 4201–4212.
91. Stephens, C., Antonov, J.I., Boyer, T.P., Conkright, M.E., Locarnini, R.A., O'Brien, T.D., Garcia, H.E., (2002), World Ocean Atlas 2001, Volume 1: Temperature. S. Levitus, Ed.,

NOAA Atlas NESDIS 49, U.S. Government Printing Office, Wash., D.C., 167 pp., CD-ROMs.

92. Straneo, F., Curry, R.G., Sutherland D.A., Hamilton G.S., Cenedese C., Vage K., and Stearns L.A., (2010), Rapid circulation of warm subtropical waters in a major, East Greenland glacial fjord. Nature Geosci,. 3, pp. 182-186.
93. Sutherland, D. and Pickart, R.S., (2008), The East Greenland Coastal Current: Structure, variability, and forcing, Progress in Oceanography, 78, pp. 58-77.
94. Swift, J.H. and Aagaard, K., (1981), Seasonal transitions and water mass formation in the Iceland and Greenland, Deep-Sea Research Part a-Oceanographic Research Papers. 28:1107-1129.
95. Tansjura, A., (1959), Currents in the Barents Sea. Proceedings of PINRO, Vol. 7, pp. 35-53.
96. Trangeled, S., (1974), Oceanography of the Norwegian and Greenland Seas and Adjacent Areas, Vol.2: Survey of 1870-1970 Literature. SACLANTCEN SM-47, SACLANT ASW Research Centre, La Spezia.
97. Troupin, C, Barth, A, Sirjacobs, D, Ouberdous, M, Brankart, J.-M, Brasseur, P, Rixen, M, Alvera Azcarate, A, Belounis, M, Capet, A, Lenartz, F, Toussaint, M.-E, & Beckers, J.-M. (2012). Generation of analysis and consistent error fields using the Data Interpolating Variational Analysis (Diva). Ocean Modelling, 52-53, pp. 90-101.
98. Troupin, C., Machín, F., Ouberdous, M., Sirjacobs, D., Barth, A. & Beckers, J.-M., (2010), High-resolution Climatology of the North-East Atlantic using Data-Interpolating Variational Analysis (Diva). Journal of Geophysical Research, 115, C08005. doi: 10.1029/2009JC005512.
99. Troupin, C., Ouberdous, M., Sirjacobs, D., Alvera-Azcárate, A., Barth, A., Toussaint, M.-E. & Beckers, J.-M., (2013), Diva User Guide, modb.oce.ulg.ac.be/mediawiki/upload/DIVA/notes/DivaUserGuide_March2013.pdf
100. Våge, K., Pickart R.S., Spall M.A., Moore G.W.K., Valdimarsson H., Torres D.J., Erofeeva S.Y., Jan Even O. Nilsen J. E. O., (2013), Revised circulation scheme north of the Denmark Strait, Deep-Sea Res., I 79 (2013), pp. 20–39.
101. Volkov, D.L., Belonenko, T.V., and Foux, V.R., (2013), Puzzling over the dynamics of the Lofoten Basin - a sub-Arctic hot spot of ocean variability, Geophys. Res. Lett., 40, pp. 738–743.
102. Wadhams, P., Budeus, G., Wilkinson, J.P., Loyning, T., and Pavlov, V., (2004), The multiyear development of long-lived convective chimneys in the Greenland Sea, Geophys. Res. Lett., 31, L06306, doi:10.1029/2003GL019017.

103. Wadhams, P., Holfort, J., Hansen, E., and Wilkinson, J.P., (2002), A deep convective chimney in the winter Greenland Sea, Geophys. Res. Lett., 29 (10), 1434, doi:10.1029/2001GL014306.
104. Walczowski, W., (2013), Frontal structures in the West Spitsbergen Current margins. Ocean Sci. Discuss., 10, pp. 985–1030.